2007

IMPLEMENTATION AND VALIDATION OF THE HYBRID TURBULENCE MODELS IN AN UNSTRUCTURED GRID CODE

Sri S. Panguluri
University of Kentucky, zphangply@gmail.com

ABSTRACT OF THESIS

IMPLEMENTATION AND VALIDATION OF THE HYBRID TURBULENCE MODELS IN AN UNSTRUCTURED GRID CODE

Since its introduction in 1997, the use of Detached Eddy Simulation (DES) and similar hybrid turbulence techniques has become increasingly popular in the field of CFD. However, with increased use some of the limitations of the DES model have become apparent. One of these is the dependence of DES on grid construction, particularly regarding the point of transition between the Reynolds-Averaged Navier-Stokes and Large Eddy Simulation models. An additional issue that arises with unstructured grids is the definition of the grid spacing in the implementation of a DES length scale. To lay the ground work to study these effects the Spalart-Allmaras one-equation turbulence model, SA based DES hybrid turbulence model, and the Scale Adaptive Simulation hybrid turbulence model are implemented in an unstructured grid CFD code, UNCLE. The implemented SA based DES model is validated for flow over a three-dimensional circular cylinder for three different turbulent Reynolds numbers. Validation included studying the pressure, skin friction coefficient, centerline velocity distributions averaged in time and space. Tools to output the mean velocity profiles and Reynolds stresses were developed. A grid generation code was written to generate a two/three dimensional circular cylinder grid to simulate flow over the cylinder in UNCLE. The models implemented and validated, and the additional tools mentioned will be used in the future.

KEYWORDS: Hybrid turbulence model, Detached Eddy Simulation, Reynolds-Averaged Navier-Stokes, Large Eddy Simulation, grid construction

Sri .S. Panguluri

03/12/2007

IMPLEMENTATION AND VALIDATION OF THE HYBRID TURBULENCE MODELS IN AN UNSTRUCTURED GRID CODE

By

Sri .S. Panguluri

Dr. Raymond .P. LeBeau

Director of Thesis

Dr. L. S. Stephens

Director of Graduate Studies

03/12/2007

RULES FOR THE USE OF THESIS

Unpublished thesis submitted for the Master's degree and deposited in the University of Kentucky Library are as a rule open for inspection, but are to be used only with due regard to the rights of the authors. Bibliographical references may be noted, but quotations or summaries of parts may be published only with the permission of the author, and with the usual scholarly acknowledgements.

Extensive copying or publication of the thesis in whole or in part also requires the consent of the Dean of the Graduate School of the University of Kentucky.

A library that borrows this thesis for use by its patrons is expected to secure the signature of each user.

Name Date

THESIS

Sri S Panguluri

The Graduate School

University of Kentucky

2007

IMPLEMENTATION AND VALIDATION OF THE HYBRID TURBULENCE MODELS IN AN UNSTRUCTURED GRID CODE

THESIS

A thesis submitted in partial fulfillment of the
requirements for the degree of Master of Science in Mechanical Engineering
in the College of Engineering at the University of Kentucky

By

Sri .S. Panguluri
Lexington, Kentucky

Director: Dr. Raymond .P. LeBeau
Assistant Professor of Mechanical Engineering
University of Kentucky Lexington, Kentucky
2007

To My Parents

ACKNOWLEDGEMENTS

I would like to take this opportunity to express my gratitude to my advisor Dr Raymond P. LeBeau. It has been a privilege for me to work under him for my Master's thesis. I would like to thank him for constantly supporting and motivating me through out this project with his valuable suggestions.

I would also like to thank Dr George P Huang for letting me use his code UNCLE for doing this research project. I would also like to thank Dr Vincent Capece and Dr Jian Sheng for their time and for serving as members for my defense committee. Finally, I would like to thank all my teachers.

I will be indebted to my parents forever who have always supported and motivated me to reach greater heights in life and achieve my goals.

TABLE OF CONTENTS

LIST OF FIGURES

LIST OF TABLES

LIST OF FILES

1. Thesis_Panguluri.pdf - 1.15 MB (File Size)

Chapter 1 : INTRODUCTION

Most of the flows occurring in nature and that are of interest for engineering applications are said to be turbulent in nature. Turbulence in nature has random velocity fluctuations and contains a wide range of eddies with varying length scales. Despite efforts by researchers for more than a century, complete understanding of turbulence to date is still an unsolved problem. The first attempt in understanding turbulence was made by Osborne Reynolds (1883, 1895), later on Prandtl (1925) with his mixing length model and Kolmogorov (1942) with a first complete turbulence model went a step further in turbulence research. By the late 1970's three main approaches for solving a turbulence problem computationally had been developed. These were the Reynolds Averaged Navier Stokes equations, Direct Numerical Simulation, and Large Eddy Simulation.

Many industrial applications in the field of computational fluid dynamics are based on the Reynolds Averaged Navier Stokes equations (RANS). The RANS approach is the most widely applied simulation technique for engineering applications involving wall bounded flows. Direct Numerical Simulation (DNS) forms another powerful tool in handling a turbulent flow problem as it resolves all the scales in a turbulent flow but with an added disadvantage of a large increase in computational cost with an increase in Reynolds number and with the complexity of the geometry to be handled. The Large Eddy Simulation (LES) technique, which falls in a category in between the RANS models and DNS, involves resolving the large scales in a flow and modeling small scales in the flow. The LES technique is generally superior to RANS models when compared for predictions of the separation regions at high Reynolds numbers. The non-affordable computational cost of LES in the attached boundary layer flows and the limitations of the RANS models in the predictions of separation regions at high Reynolds numbers inspired the introduction of hybrid turbulence models combining the advantages of both the RANS and LES models. The leading hybrid model is Detached Eddy Simulation (DES). This has been followed by Scale Adaptive Simulation (SAS) and then the next version of DES which is Delayed Detached Eddy Simulation (DDES). Increasing popularity of these models for essentially three dimensional turbulent flows at turbulent Reynolds numbers is of interest in this thesis. Flow over

a circular cylinder is a standard, challenging test case for the validation of a hybrid turbulence model like DES and is considered as a test case in this study.

1.1 Introduction to Turbulence

Most flows occurring in nature are said to be turbulent. Turbulence is a highly complex phenomenon and is three-dimensional, non-linear, and time dependent in nature. However, it has always been a difficult task to give a watertight definition for turbulence [2]. Turbulence is often described as eddying motion. One of the best known informal definitions for turbulence is given by Richardson [3] as follows:

"Big whorls have little whorls,
which feed on their velocity;
And little whorls have lesser whorls,
And so on to viscosity."

This means that the mechanical energy injected into a fluid undergoes an energy cascade on fairly large scales and it is transferred to smaller scales which in turn dissipate on molecular scales to heat.

It is easier to give specific examples for turbulent flows rather than a definition. For example turbulent flows can be observed in the flow over a golf ball, the mixing of warm and cold air in the atmosphere by wind and external flow over vehicles such as cars, airplanes, ships and submarines. Coming to a everyday example one can find a turbulent flow on a breakfast table where turbulence greatly enhances the rate at which sugar and cream mix in a cup of coffee.

Reynolds number is a dimensionless parameter that characterizes the flow behavior in different regimes. It is given as

$$\mathrm{Re} = \frac{\rho U L}{\mu}. \tag{1.1}$$

Here ρ is the density and μ is the dynamic viscosity, both of which are properties of the fluid. U is the velocity and L is the characteristic length scale of the flow, for example the radius of the pipe through which the fluid flows.

For flows with low Reynolds numbers, low velocities, and small scales, the equations of motion for a viscous fluid have well behaved steady solutions. These flows are termed as laminar flows; they are controlled by the viscous diffusion of vorticity and momentum. The Reynolds number can also be defined as the ratio of inertia forces to the viscous forces and the inertia force of the fluid overcomes the viscous stresses when the Reynolds numbers are reasonably large leading to the instability of the flow. Such flows can be described as turbulent flows.

Irregularity or randomness is one characteristic of turbulent flows. Alternately, one can describe a turbulent flow as chaotic but all chaotic flows are not turbulent e.g. Lagrangian/kinematic chaos or 'Lagrangian turbulence' [4]. Even though such a nature of turbulence emphasizes a deterministic approach rather than statistical one, the very nature of it makes turbulence an almost next to impossible task for a deterministic approach [5]. Turbulence is a continuum phenomenon governed by the equations of fluid mechanics as noted by Tennekes and Lumley [5] (1983).

"Even the smallest scales occurring in a turbulent flow are ordinarily far larger than any molecular length scale" – Tennekes and Lumley

In a viscous (real) flow the instabilities arise from the interaction between the non-linear inertial terms and the viscous terms of the Navier-Stokes equations and the interaction has a high level of complexity as by its nature it is rotational, three-dimensional, and time-dependent. This non-linearity leads to the interactions between fluctuations of differing wavelengths and directions.

Since turbulent flow is rotational and three-dimensional, it hence contains vorticity. Vorticity is defined as the curl of the velocity, $\Omega = \nabla \times \mathbf{U}$. The random vorticity fluctuations that characterize turbulence cannot maintain themselves if the velocity fluctuations are only two-dimensional as there is no vortex stretching in a two-dimensional flow. Hence, turbulent flows always exhibit high levels of fluctuating vorticity [5].

Turbulent flows exhibit strongly enhanced transport processes of momentum, energy, heat, and mass due to its diffuse nature. This property of the fluid flow helps in preventing boundary-layer separation on airfoils at larger angles of attack, increases heat transfer rates, and also increases the momentum transfer between winds and ocean currents. All flows that appear to be random in nature cannot be considered as turbulent unless the flow is diffusive by nature and exhibits a spread of the velocity fluctuations by the surrounding fluid [5].

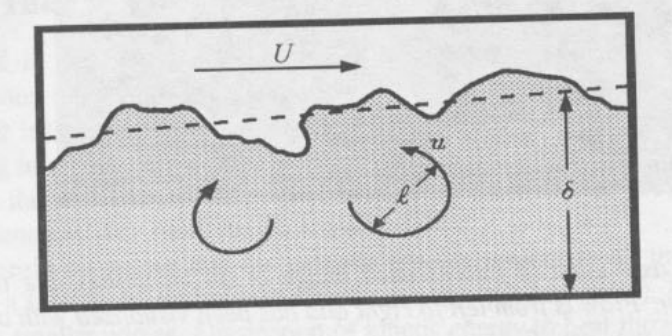

Figure 1-1 Schematic of Large eddies in a Turbulent Flow [6]

A wide range of a continuous spectrum of scales coexist in turbulent flows ranging from largest to the smallest and are superimposed in the flow, with the smaller ones inside the larger ones. A schematic for large eddies in a turbulent flow is presented in Figure 1-1. Often these scales in the turbulent flow are visualized as eddies, and a turbulent eddy can be thought of as a local swirling motion which has the dimension of a local turbulence length scale. These eddies are responsible for the vigorous mixing and turbulent stresses in the flow. Turbulence gains energy if the vortex elements are oriented in such a way that the mean flow gradients can stretch them. The larger scale turbulent motion carries most of its energy and is responsible for diffusivity and turbulent stresses. Turbulent flows are essentially dissipative. Both the larger eddies and smaller eddies overlap in space where the larger eddies carry the smaller ones and the former ones loose their energy in the form of kinetic energy to the latter ones which in turn dissipate into heat through the action of molecular viscosity.

It is appropriate to discuss the Kolmogorov length scale at this point. As turbulence follows the continuum phenomenon and the smallest length scales in turbulence are much larger

than molecular length scale of the flow, the magnitude of the smallest turbulent scales can be estimated by dimensional analysis if the physics of the turbulent flows at small scales are known. Equilibrium theory by Kolmogorov says that the smaller eddies should be in such a state that the rate of receiving energy from the larger eddies should be on the same order of its rate of dissipating energy to heat. In that case he argues that the smallest scales should only depend on the kinematic viscosity of the fluid, ν and the rate of energy supply by the large eddies, $\varepsilon = -dk/dt$. The resulting Kolmogorov length, time, and velocity scales are given as

$$\eta \equiv \left(\nu^3/\varepsilon\right)^{1/4}, \quad \tau \equiv \left(\nu/\varepsilon\right)^{1/2}, \quad \upsilon \equiv \left(\nu\varepsilon\right)^{1/4}. \tag{1.2}$$

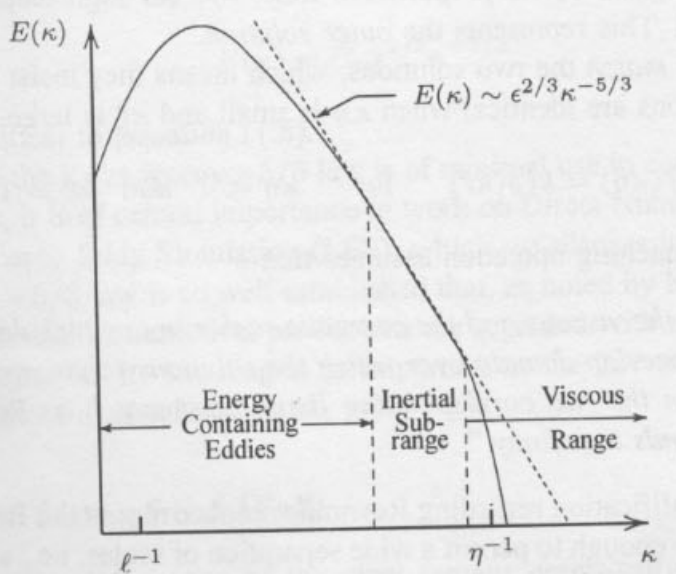

Figure 1-2 Energy Spectrum of a turbulent flow [6]

As turbulent flows contain a continuous spectrum of scales the spectral distribution of energy in the flow was analyzed. Kolmogorov came up with the -5/3 law for the representation of energy spectrum for a turbulent flow. He assumed that a wide separation of scales exist in turbulent flows and his hypothesis says that a range of eddy sizes, which fall in between the largest and the smallest eddies, exists for a very large Reynolds numbers and for these eddies the cascade process is independent of the direct effects of molecular viscosity and the statistics of energy containing eddies. Hence, the -5/3 law is given as,

$$E(k) = C_K \varepsilon^{2/3} \kappa^{-5/3}, \quad \frac{1}{l} \ll \kappa \ll \frac{1}{\eta}, \tag{1.3}$$

where $E(k)$ is the energy spectrum function, κ is the wave number, l is the characteristic length of the largest scale of the turbulent flow, η is the Kolmogorov length scale which represents the length of the smallest eddies in turbulent flow, ε is the dissipation rate from the larger eddies, and C_K is the Kolmogorov constant.

The energy spectrum is presented in Figure 1-2. The range of wavenumbers that fall between the reciprocal of characteristic length of largest eddies and the reciprocal of the Kolmogorov length scale for smallest eddies was identified as the inertial subrange by Kolmogorov.

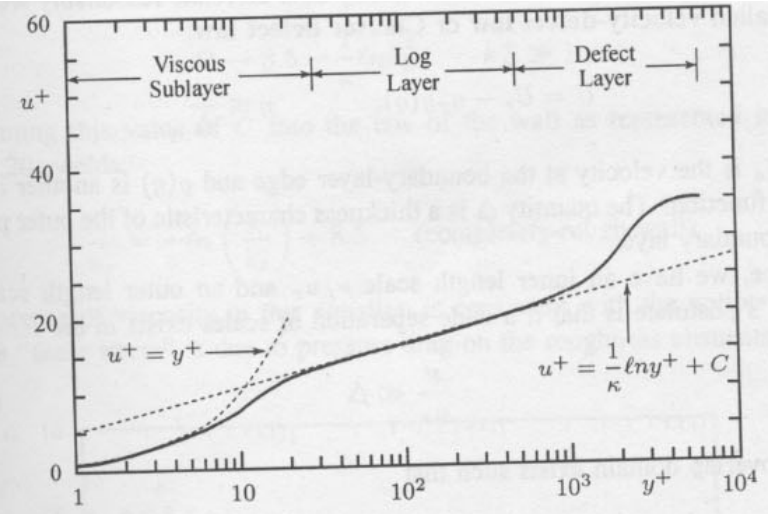

Figure 1-3 Velocity Profile of a turbulent boundary layer [6]

It is important to understand the physics in the boundary layers with increase in Reynolds numbers to deal with the grid construction where the initial spacing near the wall is considered to be critical to capture the smallest scales accurately. The velocity profile of a turbulent boundary layer is presented in Figure 1-3. Experiments for both internal and external flows show that in the flow near the wall, streamwise velocity varies logarithmically with the distance from the surface. Such a behavior is termed as the logarithmic law of the wall. At high Reynolds numbers,

the inertial forces and the pressure gradients are small near the surface and the flow near the wall is driven only by the rate of momentum transfer per unit area per unit time to the surface, local shear stress τ , and the molecular diffusion of momentum. The law of the wall is given as

$$u^+ = \frac{1}{\kappa} ln\left(y^+\right) + C\,, \tag{1.4}$$

$$\text{where, } u^+ \equiv \frac{U}{u_\tau} \text{ and } y^+ \equiv \frac{u_\tau y}{\nu}\,. \tag{1.5}$$

$$u_\tau \equiv \sqrt{\frac{\tau_w}{\rho}}\,, \tag{1.6}$$

where u_τ is a velocity scale close to the wall called the friction velocity, τ_w is the surface shear stress, ν is the kinematic viscosity, and y is the distance from the wall. From Figure 1-3 it can be observed that a turbulent boundary layer contains a viscous sublayer, a log layer, and a defect layer or the outer layer. The log layer is the overlap region between the inner and outer parts of the boundary layers. In the viscous sublayer (or inner layer), viscous shear forces dominate whereas in the outer layer the turbulent or eddy shear forces dominate and the velocity profile in the overlap region smoothly connects the inner and outer boundary layers and this region is dominated by both the viscous and turbulent shear forces.

While historically many simulations have used a “law-of-the-wall” boundary, improved accuracy is achieved by placing the initial grid points within the sublayers.

In summary of qualitative universal properties of turbulence are

- intrinsic spatial-temporal randomness, irregularity, chaotic
- unpredictability, stable statistical properties, sensitivity to initial conditions
- wide range of scales in both time and space
- highly dissipative, statistically irreversible, enhanced diffusion
- non-linear, non-integrable, non-local
- three dimensionality, rotational, time dependent

Hybrid turbulence models like DES attempt to capture these without requiring increasingly small grids near the wall.

1.2 Brief History of Turbulence Modeling

In this section the main highlights in the evolution of turbulence will be discussed briefly along with the history of turbulence modeling, particularly the statistical approach. Table 1-1 presents a brief overview about the progress made by researchers in the area of turbulence during the previous centuries.

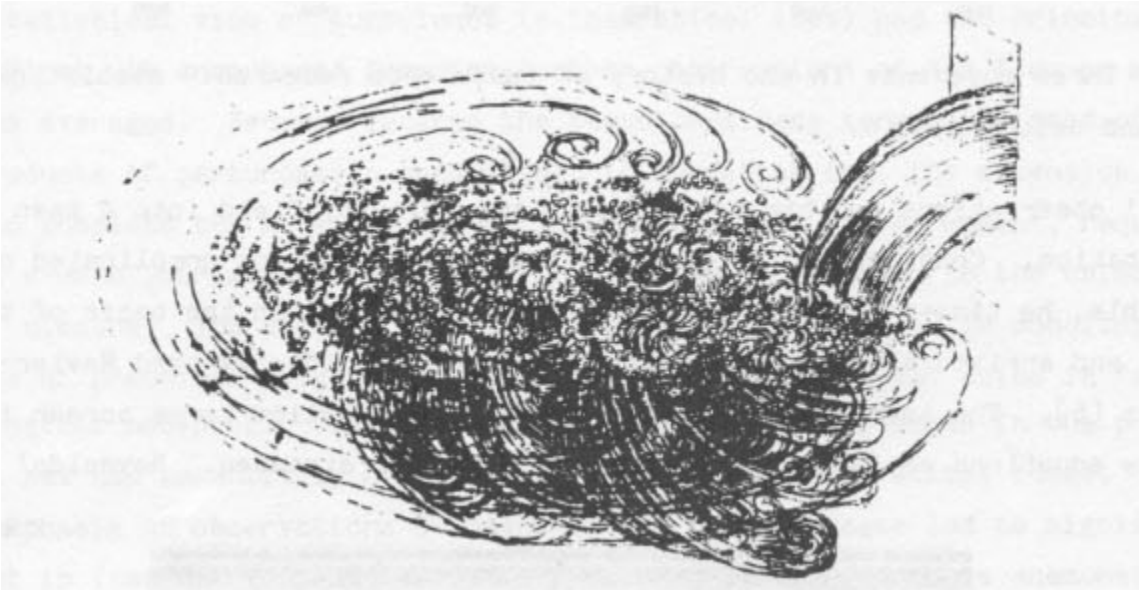

Figure 1-4 Turbulence sketch by Leonardo da Vinci [33]

Early examples [2, 6, 33, 34, 35, and 36] of turbulent studies can be found in the sketches of Leonardo da Vinci in the early 15th Century as presented in Figure 1-4. However, there was no quantitative understanding of this physical phenomenon until the late 19th Century. Boussinesq [32] in 1877 introduced the concept of eddy viscosity for a simple time-averaged turbulence closure. He replaced the molecular viscosity coefficient in the Navier-Stokes equations by turbulent or eddy viscosity coefficient and his hypothesis says that the "*turbulent stresses are linearly proportional to mean strain rate.*"

Table 1-1 Table presenting Evolution of Turbulence [4]

Year	Progress achieved in turbulence
1500	Recognition of two states of fluid motion by Leonardo da Vinci and use of the term *la turbolenza*
1839	'Rediscovery' of two states of fluid motion by G. Hagen
1883	Osborne Reynolds' experiments on pipe flow. Concept of critical Reynolds number – transition from laminar to turbulent flow regime.
1887	Introduction of the term 'turbulence' by Lord Kelvin
1895	Reynolds decomposition.
1909	D. Riabuchinsky invents the constant-current hot-wire anemometer.
1912	J. T. Morris invents the constant-temperature hot-wire anemometer.
1922	L. F. Richardson's hierarchy of eddies.
1924	L. V. Keller and A. A. Friedman formulate the hierarchy of moments.
1938	G. I. Taylor discovers the prevalence of vortex stretching.
1941	A. N. Kolmogorov local isotropy, 2/3 and 4/5 laws.
1943	S. Corrsin establishes the existence of the sharp laminar/turbulent interface in shear flows
1949	Discovery of intrinsic intermittence by G. Batchelor and A. Townsend
1951	Turbulent spot of H. W. Emmons.
1952	E. Hopf functional equation.
1967	Bursting phenomenon by S. J. Kline *et al.*
1976	Recapitulation of large scale coherent structures by A. Roshko.

Towards the end of nineteenth century Osborne Reynolds [7] (1883) presented his path-breaking work on the turbulence and his experiment of flow through a circular pipe with smooth transparent walls in which a dye streak was injected into the flow led to the observation of the transition of laminar flow to turbulent flow. Through this investigation he came up with a single dimensionless parameter called the Reynolds number, denoted by Re. His [8] observations (1895) led him to decompose the velocity field into the mean flow and a perturbation. Considering the perturbation flow either complicated or incomprehensible, he time averaged the Navier-Stokes equations based on the decomposition which led to the formulation of the well-known Reynolds-averaged Navier-Stokes equations. However, Reynolds's view of the unpredictability of the perturbations was not merely the result of observations, but was a viewpoint bolstered by the success of the statistical mechanics approach to the kinetic theory of gases.

It was only after 1920 that a successful calculation of a practical turbulent flow was achieved on the basis of the Reynolds-averaged Navier-Stokes equations with an eddy viscosity model. This was mainly due to the pioneering work of Prandtl [9] (1925) who introduced the mixing length, an analog of the mean free path of a gas, and a direct method for computing the turbulent or eddy viscosity in terms of the mixing length.

Von Karman [10] (1930) made a significant contribution by relating the mixing length hypothesis to the eddy viscosity concept. This kind of model was categorized as an algebraic or zero equation model of turbulence.

Later, with the aim of developing more realistic and general models, Prandtl [11] (1945) postulated a model in which the eddy viscosity depends on the kinetic energy of the turbulent fluctuations. This was the precursor to the so-called one-equation turbulence models. However, there was the necessity to specify the turbulence length scale, which varies with each flow, and without which a model is termed as incomplete.

Kolmogorov [12] (1942) introduced a second parameter, in addition to the modeled equation *k,* which he termed as "*the rate of dissipation of energy in unit volume and time.*" This led to the formulation of the first so-called complete turbulence model and the model was termed a two-equation turbulence model.

The foundation was laid for the formulation of a full Reynolds-stress turbulence model by Chou [13] (1945) and Rotta [14] (1951). The new model by Rotta, unlike the eddy-viscosity models, accounted for both the non-local and history effects on the evolution of Reynolds-stress tensor. Rotta has been successful in closing the Reynolds-Stress transport equation based on some of the statistical ideas of Kolmogorov. This model was termed or described as a stress-transport model or as a second-order closure or second–moment closure. Thus, by the early 1950's four kinds of turbulence models have evolved: the Algebraic or Zero equation models, the One-Equation models, the Two-Equation models, and the Stress-Transport models.

A key advance in zero-equation models occurred when Van Driest [15] (1956) applied a viscous damping correction for the mixing length model. Later, Cebeci and Smith [16] (1974) refined the model to work better for the attached boundary layer problems. A popular alternative algebraic model was suggested by Baldwin and Lomax [17] (1978). However, with continuously increasing computer power, algebraic models are used less frequently.

Coming to the developments in the one-equation models, the notable early model of this type was formulated by Bradshaw, Ferriss, and Atwell [18] (1967). After that the one-equation model was revisited by Baldwin and Barth [19] (1990), Goldberg [21] (1991), and the well-known Spalart-Allmaras (1992) model which lately appears to be the most popular and widely used one-equation model for turbulent flows.

Kolmogorov in the 1940's was the first one to introduce the two-equation model, but the first widely used formulation was the k-ε model of Launder and Spalding [21] (1972). However, the k-ε model by Launder and Sharma in 1974 is now considered to be the standard version of the k-ε models. Saffman [22] (1970) formulated a k-ω model, without prior knowledge of Kolmogorov's work, which had the advantage over the k-ε model for the prediction of flow in adverse pressure gradients. Apart from this, further work in the development of the k-ω model was taken by Wilcox and Alber [23] (1972), Saffman and Wilcox [24] (1974), Wilcox and Traci [25] (1976), and Wilcox and Rubesin [26] (1980). Later on the k-ω model was revisited by Wilcox but because of the disadvantage of the model which is sensitive to the free stream values and he further corrected the closure coefficients for the dissipation term in 1998 [6]. Meanwhile Menter in 1994 came up with the currently popular Shear Stress Transport model which retains the formulation of the k-ω model in the boundary layers and switches to a transformed k-ε model in the regions away from the wall, taking the transport effects into consideration.

The wide availability of the computer power by the 1970's gave a thrust for the development of the second-order closure models and the work began with Donaldson [27] (1972), and Daly and Harlow [28] (1970). A notable improvement of Rotta's work came from Launder, Reece and Rodi [29] (1975), as they developed a turbulence model in which the Reynolds stresses along with the turbulence dissipation rate are obtained from the solution of transport equations. Pressure-strain correlations were also derived. Subsequently, some examples of the researchers working on the second-order closure models include Lumley [30] (1978), who made significant contributions to the modeling of pressure-strain correlation and buoyancy effects, Speziale (1985, 1987) who worked on the invariance arguments, and Harworth and Pope [31] (1986), who developed a model from the pdf-based Langevin equation.

1.3 Governing Equations of Motion

One can consider two methods for deriving the equations of motion of a fluid. The first method treats the fluid as molecules whose motions are governed by the law of dynamics [37]. Equations of mass, momentum, and energy can be obtained by this approach for a fluid which is in a state not far removed from equilibrium. But this theory remains incomplete for polyatomic gas molecules and for liquids. The second method considers that the fluid consists of continuous matter or a continuum, with each point in this fluid having a unique value for velocity, pressure, density, and the other field variables. This continuum approach requires that "*the mean free path of the molecules be very small compared with the smallest physical-length scale of the fluid [37].*"

A material derivative represents the time derivative from a Lagrangian view (traveling with the fluid), and is related to the derivatives in the Eulerian view (from a fixed observer in absolute space). Here q can be any property of the fluid such as its mass, momentum, or energy in some direction $q = q(x, y, z, t)$. Then

$$\frac{Dq}{Dt} = \frac{\partial q}{\partial t} + u_k \frac{\partial q}{\partial x_k}, \tag{1.7}$$

and the Reynolds Transport Theorem relates the Eulerian and Lagrangian time derivatives for an arbitrary control volume (a material volume):

$$\frac{D}{Dt}\int_V q dV = \int_V \left[\frac{\partial q}{\partial t} + \frac{\partial}{\partial x_k}(q u_k) \right] dV . \tag{1.8}$$

Consider the equation for the conservation of mass,

$$\frac{D}{Dt}\int_V \rho dV = 0 . \tag{1.9}$$

Applying Reynolds Transport theorem to the equation above gives us the continuity equation,

$$\frac{\partial \rho}{\partial t} + \frac{\partial}{\partial x_k}(\rho u_k) = 0 , \tag{1.10}$$

and the continuity equation for an incompressible (constant density) fluid becomes

$$\frac{\partial u_k}{\partial x_k} = 0 . \tag{1.11}$$

Applying Newton's second law of motion, *the rate at which the momentum of the fluid mass is changing is equal to the net external force acting on the mass [37]*, to an element of the fluid obtains the equation for conservation of momentum,

$$\frac{D}{Dt}\int_V \rho u_j dV = \int_S \sigma_{ij} n_i dS + \int_V \rho f_j dV . \tag{1.12}$$

Applying the Reynolds Transport Theorem to the above equation gives the following form of the momentum equation:

$$\rho\frac{\partial u_j}{\partial t} + \rho u_k \frac{\partial u_j}{\partial x_k} = \frac{\partial \sigma_{ij}}{\partial x_i} + \rho f_j . \tag{1.13}$$

Stokes postulated that there are four conditions which the stress tensor is supposed to satisfy: (a) when the fluid is at rest, stress is hydrostatic, mechanical pressure is the thermodynamic pressure, (b) the stress tensor is linear with the deformation rate tensor (Newtonian fluid), (c) there is no shear stress during solid body rotation (conservation of angular momentum) and (d) the fluid is isotropic. From these conditions, the stress tensor attains a form which is

$$\sigma_{ij} = -p\delta_{ij} + \lambda\delta_{ij}\frac{\partial u_k}{\partial x_k} + \mu\left(\frac{\partial u_i}{\partial x_j} + \frac{\partial u_j}{\partial x_i}\right). \tag{1.14}$$

Here, the quantity p is the thermodynamic pressure and δ_{ij} is the Kronecker delta. The two parameters λ and μ must be determined experimentally or empirically. From Newton's law of viscosity, the proportionality factor between shear stress and the velocity gradient in a simple shear flow is the dynamic viscosity which is μ. The quantity λ is called the second viscosity coefficient.

As the difference between the mechanical pressure and the thermodynamic pressure is proportional to the divergence of the velocity vector, the proportionality factor K, called bulk viscosity, is $K = \lambda + (2/3)\mu$. However, if the fluid is a monatomic gas the mechanical pressure

and the thermodynamic pressure are the same and in this situation K = 0, hence $\lambda = -(2/3)\mu$. This is called Stokes' relation.

Substituting the obtained stress tensor equation in the momentum equation and considering the density to be constant (incompressible form) gives us the incompressible Navier-Stokes equations,

$$\rho\frac{\partial u_j}{\partial t} + \rho u_k \frac{\partial u_j}{\partial x_k} = -\frac{\partial p}{\partial x_j} + \mu\frac{\partial^2 u_j}{\partial x_i \partial x_i} + \rho f_j \,. \tag{1.15}$$

Applying the first law of thermodynamics to a fluid element to obtain the equation for conservation of energy yields

$$\frac{D}{Dt}\int_V \left(\rho e + \frac{1}{2}\rho \mathbf{u}\cdot\mathbf{u}\right) dV = \int_S \mathbf{u}\cdot\mathbf{P}\,dS + \int_V \mathbf{u}\cdot\rho\mathbf{f}\,dV - \int_S \mathbf{q}\cdot\mathbf{n}\,dS \,. \tag{1.16}$$

The Reynolds transport theorem is applied to equation (1.16) to convert it into an equation that contains Eulerian derivatives only, obtaining the energy equation in the following form,

$$\int_V \left\{\frac{\partial}{\partial t}\left(\rho e + \frac{1}{2}\rho u_j u_j\right) + \frac{\partial}{\partial x_k}\left[\left(\rho e + \frac{1}{2}\rho u_j u_j\right)u_k\right]\right\} = \int_V \frac{\partial}{\partial x_i}\left(u_j \sigma_{ij}\right) dV + \int_V u_j \rho f_j\, dV - \int_V \frac{\partial q_j}{\partial x_j} dV \,. \tag{1.17}$$

Further simplification gives us the following form of the energy equation,

$$\rho\frac{\partial e}{\partial t} + \rho u_k \frac{\partial e}{\partial x_k} + \rho u_j \frac{\partial u_j}{\partial t} + \rho u_j u_k \frac{\partial u_j}{\partial x_k} = u_j \frac{\partial \sigma_{ij}}{\partial x_i} + \sigma_{ij}\frac{\partial u_j}{\partial x_i} + u_j \rho f_j - \frac{\partial q_j}{\partial x_j} \,. \tag{1.18}$$

For a gas, it is often reasonable to assume a perfect gas (*intermolecular forces are negligible [38]*) equation of state

$$p = \rho R T \,, \tag{1.19}$$

where R is the specific gas constant. In order to close the system of equations that govern the motion of a fluid it is necessary to consider a seventh equation that provides a thermodynamic relation between the state variables ($e = e(T, p)$). For this reason, an equation for calorically perfect gas (*constant specific heats*) is often applied,

$$e = c_v T \,, \tag{1.20}$$

where c_v is the specific heat at constant volume. This equation is called the *caloric equation of state.*

1.4 Research Objective

Detached Eddy Simulation is a hybrid turbulence model that proposes to use the Reynolds Averaged Navier Stokes turbulence model in the thin boundary layers and the Large Eddy Simulation turbulence model in the regions of massive separation. Thinking of the project, the goal has been to study "grey area" and grid construction effects on the performance of hybrid turbulence models. In order to achieve this goal, the first step is to implement the DES model in the code that is required for this simulation. This code, UNCLE, is an in-house unstructured incompressible Navier-Stokes solver. As DES was initially formulated based on the one-equation Spalart-Allmaras (SA) turbulence model, there is a requirement for the implementation of the SA model in this unstructured grid code. The bigger project involves an extensive amount of computer time as it needs the implementation of the hybrid turbulence models along with the basic models and then the validation of these models for variety of test cases, analyzing and comparing with the benchmark results. After establishing the models in the code, the grid effects on the performance of the hybrid turbulence models can be studied.

The objective of this thesis is to establish the SA turbulence model, and the hybrid turbulence models, Detached Eddy Simulation and Scale-Adaptive Simulation, in an unstructured grid code. The standard test case for a simulation involving the hybrid turbulence models will be a three-dimensional circular cylinder. This work includes the implementation of the above mentioned turbulence models and presentation of the results for the flow over a three-dimensional circular cylinder for three different Reynolds numbers, 3900, 13400, and 140,000.

1.5 Thesis Outline

In Chapter 2 the numerical procedures for turbulence modeling will be discussed. These procedures include an introduction to the Direct Numerical Simulations, the Reynolds-Averaged Navier Stokes models, the Large Eddy Simulation procedures, the new hybrid turbulence model, Detached Eddy Simulation, and also other procedures that have been introduced in the hybrid

turbulence modeling. In Chapter 3, the turbulence models will be presented which include the Spalart-Allmaras one equation turbulence model, Menter's Shear Stress Transport equation based on the $k-\omega$ and $k-\varepsilon$ models, the SA based DES model, the SST based DES model, the recent SAS model by Menter, and the SA based Delayed Detached Eddy Simulation (DDES) model. In Chapter 4, the in-house CFD codes, UNCLE and GHOST, will be discussed. The various cluster architecture built by the CFD group used in running the 3D simulations of this thesis are discussed. The grid generation process in the in-house grid generator code and also in GAMBIT will be briefly presented. Chapter 5 will contain the validation studies for three test cases, first the 2D Flat plate case, second the 2D Circular Cylinder case, and last the 3D Circular Cylinder case. The last chapter, Chapter 6 will contain the conclusions and the proposed future work.

Chapter 2 : TURBULENCE MODELING

Increases in computer power since the 1960's has given a great impetus for the advancement in turbulence modeling research. A number of approaches have been suggested for this turbulence modeling problem. This section deals with three main approaches for computational turbulence modeling: Reynolds-Averaged Navier Stokes equations (RANS), Direct Numerical Simulation (DNS), and Large Eddy Simulation (LES). The RANS models are solved to determine the mean velocity flow field by modeling all the scales in a turbulent flow. The DNS technique solves the Navier-Stokes equations by resolving all the length and time scales. In the LES technique large scale motions are computed directly whereas the effects of the small scale motions are modeled. The hybrid turbulence modeling approach is from the combination of the RANS and LES approaches and is the youngest approach of all; therefore, it which will be discussed in the current trends section.

2.1 Reynolds Averaged Navier-Stokes Equations

As mentioned earlier, a better understanding of the theory of turbulence came only after the pioneering work by Osborne Reynolds (1883, 1895). In 1883 it was the identification of the Reynolds number, *Re.* Then in 1895 [40], he concluded that turbulence was far too complicated to permit a detailed understanding [41] and, as stated by Tennekes and Lumley [5], *in turbulence the description of the flow at all points in time and space is not feasible.* Hence, Reynolds proposed to decompose all the values of the hydrodynamical [40] quantities in turbulent flows into mean and fluctuating components and to study only the mean values which vary in a comparatively smooth fashion with space and time. Further, to determine the mean values he suggested using time or space averaging. Beginning with this proposal the prevailing [41] view has been that turbulence consists of random fluctuations of various flow properties and hence it must be treated with statistical tools.

The three most prominent averaging methods in turbulence research are *time* averaging, *spatial* averaging, and *ensemble* averaging. Given a flow variable $f(\mathbf{x}, t)$, its time average, $F_T(\mathbf{x})$, is defined as

$$F_T(\mathbf{x}) = \lim_{T\to\infty} \frac{1}{T} \int_t^{t+T} f(\mathbf{x},t)dt \,. \tag{2.1}$$

For homogeneous turbulence, which is a turbulent flow that is uniform in all directions on an average, a spatial average is often used. A spatial average is defined for a flow variable $f(\mathbf{x}, t)$ as

$$F_V(t) = \lim_{V\to\infty} \frac{1}{V} \iiint_V f(\mathbf{x},t)dV \,. \tag{2.2}$$

For flows that decay in time, ensemble averaging is the preferred method. If $\left\{ f^{(i)}(\mathbf{x},t) \right\}_{i=1}^{N}$ is a sequence of realizations of a function $f(\mathbf{x}, t)$ defined for $\mathbf{x} \in \Omega \subset \mathbb{R}^{\mathbf{d}}$ and $t \in \left[0, t_f\right]$, then the ensemble average for f is [41]

$$F_E(\mathbf{x},t) = \lim_{N\to\infty} \frac{1}{N} \sum_{n=1}^{N} f^{(i)}(\mathbf{x},t) \,. \tag{2.3}$$

Here time averaging is considered and the averaged equations for continuity and Navier-Stokes will be presented. In the incompressible form of the governing equations, the energy equation is uncoupled from the continuity and momentum equations [37]. Hence the averaged equations for continuity and momentum are considered here onwards. For convenience the vector form of the equations is being considered.

If $f(\mathbf{x}, t)$ is defined in a domain $\Omega \subset \mathbb{R}^d$, $d = 1,2,3$ and for $t \in [0, t_f]$, then the *Reynolds decomposition* [41] of $f(\mathbf{x}, t)$ is given by $f(\mathbf{x},t) = \overline{f}(\mathbf{x}) + f'(\mathbf{x},t)$.

Start with the continuity equation,

$$\nabla \cdot U = 0 \,. \tag{2.4}$$

By the definition of time average the following relations hold:

$$\overline{\overline{u}} = \overline{u} \;;\; \overline{u'} = 0 \,.$$

Now decomposing the continuity equation into mean and perturbation values and then time averaging the equation gives

$$\nabla \cdot \left(\overline{\overline{u} + u'} \right) = 0 \;\Rightarrow\; \nabla \cdot \overline{\overline{u}} + \nabla \cdot \overline{u'} = 0$$

$$\Rightarrow \nabla \cdot \overline{u} = 0 . \tag{2.5}$$

Next, consider the following form of the Navier-Stokes equations for incompressible flow and no body forces,

$$U_t + U \cdot \nabla U = -\nabla P + \nu \nabla^2 U . \tag{2.6}$$

Starting with the advection term, take the time average,

$$\begin{aligned} U \cdot \nabla U &= (\overline{u} + u') \cdot \nabla (\overline{u} + u') \\ &= \overline{\overline{u} \cdot \nabla \overline{u}} + \overline{u' \cdot \nabla \overline{u}} + \overline{\overline{u} \cdot \nabla u'} + \overline{u' \cdot \nabla u'}. \end{aligned} \tag{2.7}$$

The second and third terms may be eliminated as follows,

$$\begin{aligned} \overline{\overline{u} \cdot \nabla u'} + \overline{u' \cdot \nabla \overline{u}} &= \lim_{T \to \infty} \frac{1}{T} \int_0^T \overline{u} \cdot \nabla u' dt + \lim_{T \to \infty} \frac{1}{T} \int_0^T u' \cdot \nabla \overline{u} dt \\ &= \overline{u} \cdot \nabla \left[\lim_{T \to \infty} \frac{1}{T} \int_0^T u' dt \right] + \left[\lim_{T \to \infty} \frac{1}{T} \int_0^T u' dt \right] \cdot \nabla \overline{u} \\ &= 0 \end{aligned} \tag{2.8}$$

Now consider the first term,

$$\begin{aligned} U_t &= \overline{(\overline{u} + u')}_t \\ &= \overline{u}_t . \end{aligned} \tag{2.9}$$

The RHS is treated similarly and the N-S equation is reduced to the following form,

$$\overline{\overline{u} \cdot \nabla \overline{u}} + \overline{u' \cdot \nabla u'} = -\nabla \overline{p} + \nu \nabla^2 \overline{u} . \tag{2.10}$$

The LHS terms can be simplified further as,

$$\nabla \cdot \overline{u}^2 + \nabla \cdot \overline{u'^2} = -\nabla \overline{p} + \nu \nabla^2 \overline{u} . \tag{2.11}$$

The Reynolds-Averaged Navier Stokes equations that have been derived contain more unknowns than earlier, as the fluctuating terms, such as $\overline{u'^2}$ on the LHS, are unknown. Hence reducing the number of unknowns to a solvable number is the so-called "*turbulence closure problem*". The terms, like $\overline{u'^2}$ form the *Reynolds stress tensor* which when multiplied by density has the dimensions of a stress. The term $\overline{u'^2}$ is written in a matrix representation:

$$\overline{u'^2} = \begin{pmatrix} \overline{u'^2} & \overline{u'v'} & \overline{u'w'} \\ \overline{v'u'} & \overline{v'^2} & \overline{v'w'} \\ \overline{w'u'} & \overline{w'v'} & \overline{w'^2} \end{pmatrix} . \tag{2.12}$$

It is to be recalled that the term $\overline{u'^2}$ has a divergence operator, and often the stress tensor term is represented in the following form,

$$\mathbf{R}\left(u',u'\right)=\nabla\cdot\begin{pmatrix}\overline{u'^2} & \overline{u'v'} & \overline{u'w'}\\ \overline{v'u'} & \overline{v'^2} & \overline{v'w'}\\ \overline{w'u'} & \overline{w'v'} & \overline{w'^2}\end{pmatrix}=\nabla\cdot\tau_{ij} \tag{2.13}$$

Hence the alternative form for the Reynolds averaged Navier Stokes equation for an incompressible fluid neglecting the body forces is

$$\nabla\cdot\overline{u}^2=-\nabla\overline{p}+\nu\nabla^2\overline{u}-\mathbf{R}\left(u',u'\right). \tag{2.14}$$

2.2 Direct Numerical Simulation

In Direct Numerical Simulation [42] the Navier-Stokes equations are numerically solved for the complete detail of all the flow variables in a turbulent flow field. As given in [6], *"direct numerical simulation means a complete three-dimensional and time dependent solution of the Navier-Stokes and continuity equations"*. These direct numerical simulations in theory are required to get the accurate solutions of the equations of motion. In principle they are required to accurately resolve all the scales of turbulent motion with the given initial and boundary conditions.

The foundations for DNS were laid by the meteorologists at the National Center for Atmospheric Research [39]. The first step came from the work of Orszag and Patterson [43] in 1972. They performed a 32^3 computation of isotropic turbulence for a Taylor microscale based Reynolds number of 35. The Taylor microscale Reynolds number is $Re_T^{-1/2}=\left(15/A\right)^{-1/2}\left(\lambda/l\right)$ where the Taylor microscale is given by $\lambda^2=\overline{u'^2}\Big/\overline{\left(\partial u'/\partial x\right)^2}$, l is the integral length scale, the constant A is on the order of 1. The next major step was by Rogallo [73] in 1981. He combined an extension of the algorithm by Orszag-Patterson and transformed governing equations to compute homogeneous turbulence subjected to mean strain. His work has become a cornerstone for homogeneous turbulent flows. Further details of the history of DNS can be found in Moin and Mahesh (1998) and the references therein.

Even though the predictions about flow behavior by DNS have been quite accurate as all the scales in the flow are resolved, there are many numerical issues with DNS, when applied to engineering flows. These include spatial and time resolution, specification of boundary conditions, Reynolds numbers, computational costs, and the shock waves in compressible turbulent flows.

Complete resolution of both the largest and the smallest length scales is required to define the turbulent flow field in DNS. For inhomogeneous flows the physical parameters, such as the characteristic width of the flow, determine the largest length scale whereas for homogeneous turbulence to ensure proper representation of large scales two-point correlations of the solution are required to decay nearly to zero within half the domain. The smallest scales that need to be resolved in both cases are on the order of the Kolmogorov length scale, $\eta = \left(\nu^3/\varepsilon\right)^{1/4}$. The measure of the smallest length scale, most of the time, is influenced by the numerical methods used. In spectral DNS methods the smallest scale required must capture the dissipation accurately, hence the smallest length scales are dependent on the energy spectrum, whose length scale is much greater than η. Finite differencing schemes, prone to larger numerical errors, require higher resolution at the small scales to retain the same degree of accuracy as spectral methods. The differentiation error and error from the non-linearity of the governing equations of motion are the two errors that demand higher resolution at smaller scales. However, a potentially more serious problem in spectral codes resulting from the non-linearity is aliasing which can cause numerical instability or excessive turbulence decay. Aliasing occurs when the nonlinear interactions among the resolved wave numbers produce waves with wave numbers greater than κ_{max}, which can be misinterpreted numerically [6].

Even though spectral methods are potentially more accurate than finite differencing or finite volume schemes, the latter methods are often considered in the case of more non-uniform and unstructured grids.

The time step in the computation of DNS should be on the order of magnitude of Kolmogorov time scale, $\tau = \left(\nu/\varepsilon\right)^{1/2}$. However, the time step is influenced by the accuracy required for DNS to resolve for resolving the wide range of scales accurately over time.

While solid boundaries with their no-slip boundary conditions posed no special issues, specifying the boundary conditions at open boundaries has always been a critical issue with

DNS. It is relatively straightforward to impose periodic boundary conditions in the statistically homogeneous direction of the flow, so the issue is primarily about inflow and outflow boundary conditions. This problem earlier had been handled by assuming the flow to be homogeneous in the streamwise direction and it was allowed to evolve statistically in time. Spalart [44] in 1988 presented a coordinate transformation that allowed the use of periodic boundary conditions in the streamwise direction, thereby allowing the flow to grow as a statistically stationary turbulent flow. Still, the method proposed by Spalart was restricted to a certain class of flows. An alternative method suggested was to add a random velocity field to a prescribed mean velocity field and allow the flow to evolve but the disturbances took considerably larger downstream distances to evolve into a true turbulence flow [42].

Computations of shock waves with DNS mainly have been for steady aerodynamic flows. Because it is expensive to compute the shock-thickness in these flows, shock capturing schemes have been useful tools for such flows. However, the potential problem arising from such schemes is that they are highly dissipative and may dissipate important scales of turbulence if the resolution is not sufficiently fine [42].

Even though the increase in computer power to date had let DNS to stretch over a larger variety of conditions, the Reynolds numbers are still below those required for most practical engineering flows. The exceedingly large computational costs of DNS increase rapidly with the Reynolds number, approximately on the order of $O\left(Re^3\right)$ [46]. This remains a critical drawback of DNS. Computations from DNS possess a high degree of accuracy and it can be viewed in some cases as comparable as or better than experimental benchmark data. Practically, the computational results from DNS can be used in testing the proposed closure approximations in the turbulence models and are also useful in closely observing the turbulent structures and collecting some useful information about the immeasurable quantities like pressure fluctuations.

2.3 Large-Eddy Simulation

In Large Eddy Simulations the energy carrying large scales of turbulence motion are resolved or represented explicitly and the effects of smaller scales that appear in the residual stress terms are modeled. Initial work on the LES model came from Smagorinsky [45] in 1963,

Lilly [75] in 1967, and Deardorff [47, 76] in 1970, 1974 and much of their work was motivated by meteorological applications and atmospheric boundary layers. Initially, in the testing and development phase, the primary focus of LES was in the area of isotropic turbulence. Important examples of this type include the work of Kraichnan [77] in 1976 and Chasnov [78] in 1991. Another common flow was fully-developed channel flow like those of Deardorff [47] in 1970, Schumann [79] in 1975, Moin and Kim [80] in 1982, and Piomelli [81] in 1993. Much more detail about the history of LES models and their evolutionary process is discussed by Galperin and Orszag [82] (1993).

By the nature of its formulation, the smallest scales in a LES model are modeled and can be much larger than the Kolmogorov length scales. The time step requirement by the LES model can be higher than the Kolmogorov time scale which allows the applicability of LES for much higher Reynolds numbers than DNS methods. However, DNS-like numerical issues such as the boundary condition specification difficulties and the degree of accuracy requirement in computing the derivatives for the smallest scales still hold for LES. An additional problem arises at the near wall regions where the largest eddies are quite small and if one needs to fully resolve these scales then numerically the requirements of LES models tends towards the DNS method. The goal of LES is not to compute all the dissipation scales but to compute the scales in the inertial range only. An LES model falls in a category between the class of RANS methods, in which turbulence motion is completely modeled, and the DNS methods, in which the all the scales need to be completely resolved.

A classical solution procedure for LES, in principle, can be classified into four steps,

i. The velocity field and the other flow variables are decomposed into the large and small scales. For this process a filtering operation is defined.
ii. The decomposition is applied to the governing equations separating the non-linear terms which are to be modeled.
iii. These non-linear terms are modeled.
iv. The filtered governing equations are solved explicitly for the larger scales.

Similar to the approach of Reynolds averaging the governing equations, LES decomposition was first introduced by Deardorff [47] but studied by Leonard [48] in detail for the incompressible Navier-Stokes equations.

LES decomposition for a velocity vector **U** is given as

$$\mathbf{U}(\mathbf{x},t) = \tilde{\mathbf{u}}(\mathbf{x},t) + \mathbf{u}'(\mathbf{x},t). \tag{2.15}$$

The $\tilde{\mathbf{u}}(\mathbf{x},t)$ term represents the resolved part, meaning larger scales, and the $\mathbf{u}'(\mathbf{x},t)$ term represents the unresolved scales or the smaller scales of the flow. If $\tilde{U}(x,y,z)$ represents the large scale field, defined as a low-pass filter, then the filtering operation [49] is given as

$$\tilde{U}(x,y,z) = \int_D \prod_{i=1}^{3} G_i(x_i, x_i') U(x,y,z)\, dx\, dy\, dz \equiv \tilde{u}(x,y,z), \tag{2.16}$$

where *G* is the filter function and *D* is the entire computational domain.

Even though many filtering techniques have emerged, a few notable filter functions have been the Gaussian filter function, the sharp Fourier cut-off filter, and the box filter.

The Gaussian filter is defined as

$$G_i(x_i, x_i') = \left(\frac{6}{\pi\Delta_i^2}\right)^{1/2} exp\left(\frac{-6(x_i - x_i')^2}{\Delta_i^2}\right), \tag{2.17}$$

where Δ_i is the filter width related to the grid size Δx_i. The sharp Fourier cut-off filter defined in the Fourier space is,

$$\hat{G}_i(k_i) = \begin{cases} 1, & for\ k_i < K_{ci} \\ 0, & otherwise \end{cases}, \tag{2.18}$$

where K_{ci} is the cut-off wave number given by the correlation $K_{ci} = \frac{\pi}{\Delta_i}$ and $\hat{G}_i(k_i)$ is the Fourier coefficient of the filter function G_i.

The box filter function is defined as

$$G_i(x_i, x_i') = \begin{cases} 1/\Delta_i, & for\ |x_i - x_i'| \le \Delta_i/2 \\ 0, & otherwise \end{cases}. \tag{2.19}$$

Once the low-pass filter for the large scales of motion is defined, the unresolved parts of the model or the smaller scales are defined as the high-pass filtered part for the velocity vector:

$$\mathbf{u}'(\mathbf{x},t) = \mathbf{U}(\mathbf{x},t) - \tilde{\mathbf{u}}(\mathbf{x},t). \tag{2.20}$$

The following relations hold as both the resolved and unresolved terms are not independent of time and space,

$$\tilde{\tilde{\mathbf{u}}}(\mathbf{x},t) \neq \tilde{\mathbf{u}}(\mathbf{x},t) \text{ and } \tilde{\mathbf{u}}'(\mathbf{x},t) \neq 0. \tag{2.21}$$

The LES decomposition is applied to the governing equations in the incompressible form and for convenience the vector form of the equations is considered. Start with the continuity equation for incompressible flow in vector form,

$$\nabla \cdot \mathbf{U} = 0 . \tag{2.22}$$

After a filtering operation to obtain the resolved scales, the continuity equation takes the following form [41],

$$\nabla \cdot \tilde{\mathbf{u}} = 0 . \tag{2.23}$$

Now consider the momentum equations,

$$\mathbf{U}_t + \mathbf{U} \cdot \nabla \mathbf{U} = -\nabla P + \nu \nabla^2 \mathbf{U} . \tag{2.24}$$

The reduced form of momentum equation after the filtering operation can be expressed as,

$$\tilde{\mathbf{u}}_t + \nabla \cdot \left(\widetilde{\mathbf{U}\mathbf{U}} \right) = -\nabla \tilde{p} + \nu \nabla^2 \tilde{\mathbf{u}} . \tag{2.25}$$

It is a relatively easy task to apply the filtering operation for the RHS terms and for the time derivative, but a little work is needed to be done for the non-linear advection terms on the LHS.

Consider the non-linear terms,

$$\nabla \cdot \left(\widetilde{\mathbf{U}\mathbf{U}} \right) = \nabla \cdot \left(\widetilde{(\tilde{\mathbf{u}}+\mathbf{u}')(\tilde{\mathbf{u}}+\mathbf{u}')} \right), \tag{2.26}$$

and then write the terms in the matrix form as follows,

$$\widetilde{(\tilde{\mathbf{u}}+\mathbf{u}')(\tilde{\mathbf{u}}+\mathbf{u}')} = \begin{bmatrix} \widetilde{(\tilde{u}+u')(\tilde{u}+u')} & \widetilde{(\tilde{u}+u')(\tilde{v}+v')} & \widetilde{(\tilde{u}+u')(\tilde{w}+w')} \\ \widetilde{(\tilde{u}+u')(\tilde{v}+v')} & \widetilde{(\tilde{v}+v')(\tilde{v}+v')} & \widetilde{(\tilde{v}+v')(\tilde{w}+w')} \\ \widetilde{(\tilde{u}+u')(\tilde{w}+w')} & \widetilde{(\tilde{v}+v')(\tilde{w}+w')} & \widetilde{(\tilde{w}+w')(\tilde{w}+w')} \end{bmatrix} . \tag{2.27}$$

One of the terms from the matrix is considered and then expanded to get the following form,

$$\widetilde{(\tilde{u}+u')(\tilde{v}+v')} = \widetilde{\tilde{u}\tilde{v}} + \widetilde{\tilde{u}v'} + \widetilde{u'\tilde{v}} + \widetilde{u'v'} . \tag{2.28}$$

Unlike the Reynolds decomposition, the second and third terms on the right-hand side are not zeroes and these are termed as *"*cross stress*"* terms. It is required to model the cross stress terms as they contain the small scale factors. The first term, $\widetilde{\tilde{u}\tilde{v}}$, on the right-hand side is called a Leonard stress and it can be calculated directly, as the equations for $\tilde{u}$ and $\tilde{v}$ are available.

Analogous to the Reynolds stress terms from the Reynolds decomposition, the last term

on the right-hand side is also named a *"*Reynolds stress*"* term. It is understood that even though the similarity in the names exist, the methods of modeling the Reynolds stresses differ from RANS to LES.

In general, the notation given to the stress terms are

$$\begin{aligned} L_{ij} &\equiv \widetilde{\tilde{u}\tilde{v}} - \tilde{u}\tilde{v}, \\ C_{ij} &\equiv \widetilde{\tilde{u}v'} + \widetilde{u'\tilde{v}}, \\ R_{ij} &\equiv \widetilde{u'v'}, \end{aligned} \tag{2.29}$$

where L_{ij} represents the Leonard stress, C_{ij} is the Cross stress and R_{ij} is the Reynolds stress.

In order to obtain the useful form of the momentum equations it is desirable to have the conservative form of $\nabla\cdot\left(\tilde{\mathbf{u}}\tilde{\mathbf{u}}\right)$ [41]. For this reason the non-linear terms are revisited and the left-hand side is rearranged as,

$$\tilde{\mathbf{u}}\tilde{\mathbf{u}} + \left[\left(\widetilde{(\tilde{\mathbf{u}}+\mathbf{u}')(\tilde{\mathbf{u}}+\mathbf{u}')}\right) - \tilde{\mathbf{u}}\tilde{\mathbf{u}}\right] \equiv \tilde{\mathbf{u}}\tilde{\mathbf{u}} + \tau_{SGS}\,. \tag{2.30}$$

Hence the momentum equation can be reduced to the following useful form,

$$\tilde{\mathbf{u}}_t + \nabla\cdot(\tilde{\mathbf{u}}\tilde{\mathbf{u}}) = -\nabla\tilde{p} + \nu\nabla^2\tilde{\mathbf{u}} - \nabla\cdot\tau_{SGS}\,, \tag{2.31}$$

where the LES subgrid scale stress is given by $\tau_{SGS} \equiv L_{ij} + C_{ij} + R_{ij}$.

At this point the governing equations have passed through the filtering operation and the large scale part of the LES formulation has been obtained. The next step is to model the subgrid scale stress.

In general, the small scales in turbulent flows tend to be isotropic and homogeneous in comparison with the larger scales and are considered to be able to be modeled using relatively simpler models than those used for Reynolds stress models [50]. For this reason the subgrid scale models are usually based on the eddy viscosity assumptions. Generally, the SGS models fall into three categories: eddy viscosity models, similarity models, and mixed models which combine both the eddy viscosity and similarity expressions [51]. Here, the discussion of the SGS models will be restricted to eddy viscosity models as we will be basically dealing with the Smagorinsky SGS model based on eddy viscosity assumptions.

Smagorinsky [45] (1963) was the first to introduce the modeling procedures for the subgrid scale stress (SGS). His formulation was based on the Boussinesq eddy viscosity assumption. The basic equations applied to the SGS model are

$$\tau_{SGS} = -2\nu_T \tilde{S}_{ij} \quad \text{and} \quad \nu_T = \left(C_S \Delta\right)^2 \left|\tilde{S}\right|, \tag{2.32}$$

$$\left|\tilde{S}\right| = \sqrt{2\tilde{S}_{ij}\tilde{S}_{ij}}\,, \tag{2.33}$$

$$\tilde{S}_{ij} = \frac{1}{2}\left(\frac{\partial \tilde{u}_j}{\partial x_i} + \frac{\partial \tilde{u}_i}{\partial x_j}\right). \tag{2.34}$$

$\tilde{S}_{ij}$ is the large scale strain rate tensor, $\tilde{u}_i$ is the large scale velocity, the eddy viscosity ν_T is calculated similarly to a mixing length formulation, and Δ is the grid spacing. C_S is the Smagorinsky constant which is on the order of 10^{-1} and usually varies from flow to flow. For example, as determined by Lilly [52] in 1966 $C_s \simeq 0.23$ for homogeneous isotropic turbulent flows, but in the case of turbulent channel flows $C_s \simeq 0.23$ had excessive damping on the large scale fluctuations and for this reason Deardorff [47] suggested $C_s \simeq 0.1$.

The Smagorinsky SGS model does enjoy success to an extent due to its simplicity and that it yields sufficient diffusion and dissipation [6] for numerical stability. But for the same reason that it is completely dissipative, the model is not adequate for the wall bounded flows. Also the model cannot account for the energy flow from smaller scales to larger scales which can be termed as *"backscatter"*.

Further modifications made to the Smagorinsky model in the near wall regions include the work by Moin and Kim [53] in using the Van Driest [54] damping functions to account for the near wall effects and then Piomelli's [55] choice of choosing a damping function to account for the asymptotic behavior of the shear stresses near the wall.

A SGS model based on the renormalization group (RNG) theory of Yakhot and Orszag [56] was proposed by Yakhot [57] in 1989 for channel flows. This model predicts the stresses near the wall to be zero requiring no additional damping functions, but an *ad hoc* factor was introduced by Yakhot [57] to account for the anisotropy of the smaller scales in the near wall region.

Germano [50] in 1991 proposed a SGS stress model based on the Smagorinsky SGS model, and this class of models was termed the dynamic models. Two filtering operations for the governing equations are used, one using the grid filter and the second one using the test filter. The filter width of test filter is larger than that of the grid filter from which it can be inferred that the test filter corresponds to a coarser mesh than the grid filter. The subgrid scale stresses are

obtained by the rescaled resolved stresses in the test filter band. The Smagorinsky constant is evaluated in the test filter band from the resolved stresses and then the same value is used to compute the subgrid scale stresses at the same point in space but at the next time step [6].

The twice filtered tensor, $T_{ij} = \widetilde{\widetilde{u_i u_j}} - \tilde{\tilde{u}}_i \tilde{\tilde{u}}_j$, and the SGS tensor, $\tau_{ij} = \widetilde{u_i u_j} - \tilde{u}_i \tilde{u}_j$, from the test filter are related to the Leonard stress, $L_{ij} = \widetilde{\tilde{u}_i \tilde{u}_j} - \tilde{\tilde{u}}_i \tilde{\tilde{u}}_j$, obtained from the test filter which is termed the Germano identity. Hence,

$$L_{ij} = T_{ij} - \tau_{ij}. \tag{2.35}$$

Here, the Leonard stress can be calculated explicitly whereas the subgrid stress tensors are to be modeled. The Smagorinsky's closure can be applied to the Germano identity,

$$\tau_{ij} \equiv \tau_{ij} - \frac{1}{3}\tau_{kk}\delta_{ij} = C_S \beta_{ij}, \tag{2.36}$$

$$T_{ij} \equiv T_{ij} - \frac{1}{3}T_{kk}\delta_{ij} = C_S \alpha_{ij}. \tag{2.37}$$

The values α_{ij} and β_{ij} should be treated as the SGS models (Smagorinsky) with the Smagorinsky constant removed and the other point to be noted is that C_S is actually $\left(C_S\right)^2$ from the Smagorinsky model. Using the Germano identity the Leonard stress tensor is

$$L_{ij} \equiv L_{ij} - \frac{1}{3}L_{kk}\delta_{ij} = C_S\left(\alpha_{ij} - \beta_{ij}\right). \tag{2.38}$$

However, the above equation contains five independent equations for evaluating a single variable, C_S, and hence is over determined. In order to overcome this situation two alternatives were proposed by Germano (1991) and Lilly (1992).

The correction given by Germano (1991) was to contract the above equation from the Germano identity with the strain-rate tensor $\tilde{S}_{ij}$ which is reformulated as

$$C_S = \frac{L_{ij}\tilde{S}_{ij}}{M_{ij}\tilde{S}_{ij}}, \tag{2.39}$$

where $M_{ij} = \left(\alpha_{ij} - \beta_{ij}\right)$. Unfortunately the denominator could become excessively small or locally vanish which might lead to computational instabilities. Lilly (1992) used a least squares approach in order to evaluate the value of C_S that best satisfies the model, given as

$$C_S = \frac{L_{ij} M_{ij}}{M_{ij}^2}. \tag{2.40}$$

Even after these corrections the model revealed another difficulty in that the C_S predicted by the above two models may strongly vary in space and can contain negative values which implies a negative SGS eddy viscosity which may cause instability to the computations. In order to avoid such problem averaging of the values both in time and space for numerators and denominators has been adopted. Later on averaging was suggested to be applied in the directions in which flow exhibits homogeneity; however, this process is restricted to simpler geometries. It is noted that schemes based on the spatial averages are still the most widely used LES methods for the apparent reason of their simplicity in implementation.

2.4 Current Trends

2.4.1 Hybrid Turbulence Models

The earlier sections cover in detail about the RANS, LES and DNS methods of turbulence modeling. The LES models by its nature falls in a category in between the DNS and the RANS models as these models do not completely model all the turbulent scales in a flow as in RANS but neither do they resolve all the scales of a flow as in DNS

As suggested by Spalart [58], the known major challenges about turbulence predictions have been the prediction of the growth and separation of the boundary layer along with the accuracy in assessing the Reynolds stresses after the separation. The Reynolds-Averaged Navier-Stokes equations are the most widely used today. For the past two decades many RANS models have been suggested and of them the *k*-*ε*, [74] the one-equation Spalart-Allmaras [60] turbulence model, and the two-equation Shear Stress Transport [62] (SST) turbulence model are popular. Even though the RANS models are very robust in predicting the boundary layer flows, in the prediction of the massively separated, unsteady turbulent flows these models tend to fail. DNS is out of question for the higher Reynolds numbers at which massive separation occurs because of its demand of fine grid spacing which increases the computational cost. The LES models have

the capability of handling the separation regions well as the large scales are resolved but not modeled. But when practical applications like a simulation on a airplane wing is considered the computational cost of LES goes high because of the number of grids points needed in the boundary layers because of the presence of large thin near-wall boundary layers containing small eddies whose local size is much smaller than the local boundary layer thickness. In such a case, Spalart [1] estimated the number of grid points that are needed to be on the order of 10^{11} and to get a clear solution the number of time steps needed are estimated to be $5x10^{6}$.

In order to retain the robustness of RANS models in accurately predicting the boundary layer flows and the well behaved LES models in the regions of massive separation at higher Reynolds number, a hybrid turbulence model was suggested by Spalart [1] in 1997. The non-affordable computational cost of the LES in the attached boundary layers and the failure of RANS models in accurately predicting the massively separated regions at high Reynolds numbers lead to the formulation of the hybrid turbulence model. The attached boundary layers are modeled and the large scale detached eddies are resolved or simulated in this new hybrid turbulence model and hence the name "Detached Eddy Simulation" (DES) is given to this model. The DES model operates in RANS mode in the attached boundary layers and away from the wall it switches to the LES mode.

Initially, the DES model was based on the one-equation Spalart-Allmaras turbulence model formulated by Spalart [1] in 1997. However, it was only in the year 2000 that an alternate DES was formulated based on Menter's two-equation Shear Stress Transport turbulence model by Travin, Shur, Strelets and Spalart [59]. Later on Menter came up with a Scale Adaptive Simulation model in 2003 and in this paper [63] his intention was to demonstrate that the SAS modeling approach can be operated in RANS and LES modes without explicit grid dependency as opposed to the case of DES which is dependent on the grid spacing. The models along with the grid issues will be discussed in the next chapter. In 2006, Spalart and others [66] came up with a new hybrid turbulence model based on DES model but had a correction factor to allow for smooth transition from RANS to the LES mode. This new version is called as "Delayed Detached Eddy Simulation" [66].

Chapter 3 : TURBULENCE MODELS

In this chapter, the turbulence models based on the Reynolds-Averaged Navier Stokes equations and also the more recently popular hybrid turbulence models are described in detail. The RANS models covered include the one-equation Spalart-Allmaras turbulence model, the two-equation *k*-ω and *k*-ε models, and Menter's Shear Stress Transport (SST) turbulence model. The hybrid turbulence models include the original formulation of the Detached Eddy Simulation (DES) by Spalart based on his one-equation Spalart-Allmaras turbulence model, the formulation of DES based on the Menter's SST model, the Scale-Adaptive Simulation by Menter, and finally the Delayed Detached Eddy Simulation (DDES) formulation.

3.1 One Equation Spalart – Allmaras Model

The one equation Spalart-Allmaras (SA) model solves a transport equation for the variable $\tilde{\nu}$ which is similar to the eddy viscosity. The equation is formulated using empiricism and the arguments of dimensional analysis, Galilean invariance, and selective dependence on the molecular viscosity [60]. The equation contains four terms which are a production term, a destruction or loss term, and two diffusion terms. The loss term depends on the distance to the wall. This turbulence model is compatible with both structured and unstructured grids. The insensitivity of this model to the free stream helps to obtain a stable solution.

The Reynolds stresses, which are the cause of the so-called "closure problem", are defined using the Boussinesq eddy viscosity concept as

$$-\overline{u_i u_j} = 2\nu_t S_{ij}, \qquad \text{where } S_{ij} \equiv \left(\frac{\partial U_i}{\partial x_j} + \frac{\partial U_j}{\partial x_i} \right) \Big/ 2 . \tag{3.1}$$

Alternatively, the strain rate can also be written as $S = \sqrt{2\Omega_{ij}\Omega_{ij}}$ where $\Omega_{ij} = \frac{1}{2}\left(\frac{\partial U_i}{\partial x_j} - \frac{\partial U_j}{\partial x_i} \right)$.

The turbulent viscosity or eddy viscosity, ν_T, is a function of $\tilde{\nu}$, which is termed the high Reynolds number viscosity. The functional relation is

$$\nu_T = \tilde{\nu} f_{v1}, \tag{3.2}$$

$$f_{v1} = \frac{\chi^3}{\chi^3 + c_{v1}^3}\ ,\ \chi = \frac{\tilde{\nu}}{\nu}, \tag{3.3}$$

where ν is the molecular viscosity and $c_{v1} = 7.1$. When $\tilde{\nu} \gg \nu$, then $f_{v1} \approx 1$ and $\nu_T \approx \tilde{\nu}$. The evolution of $\tilde{\nu}$ is governed by a transport equation

$$\frac{\partial \tilde{\nu}}{\partial t} + U_j \frac{\partial \tilde{\nu}}{\partial x_j} = c_{b1}\tilde{S}\tilde{\nu} - \left[c_{w1} f_w - \frac{c_{b1}}{\kappa^2} f_{t2}\right]\left(\frac{\tilde{\nu}}{d}\right)^2 + \frac{1}{\sigma}\left[\frac{\partial}{\partial x_k}\left[(\nu + \tilde{\nu})\frac{\partial \tilde{\nu}}{\partial x_k}\right] + c_{b2}\frac{\partial \tilde{\nu}}{\partial x_k}\frac{\partial \tilde{\nu}}{\partial x_k}\right] + f_{t1}\Delta U^2. \tag{3.4}$$

The first term on the right hand side is the production term. In this term, $\tilde{S}$ is a modeled magnitude of the strain rate

$$\tilde{S} = S + \frac{\tilde{\nu}}{\kappa^2 d^2} f_{v2}, \tag{3.5}$$

where *d* is the distance to the closest wall and f_{v2} is given by the correlation,

$$f_{v2} = 1 - \frac{\chi}{1 + \chi f_{v1}}. \tag{3.6}$$

The second term on the right hand side is the destruction or loss term. The function c_{w1} is given by the correlation

$$c_{w1} = \frac{c_{b1}}{\kappa^2}\frac{(1 + c_{b2})}{\sigma}, \tag{3.7}$$

where σ is the turbulent Prandtl number. The wall function f_w is defined as

$$f_w = g\left(\frac{1 + c_{w3}^6}{g^6 + c_{w3}^6}\right)^{1/6}, \tag{3.8}$$

$$r = \frac{\tilde{\nu}}{\tilde{S}\kappa^2 d^2},\ \ g = r + c_{w2}\left(r^6 - r\right). \tag{3.9}$$

The variable *r*, which is used in evaluating the wall function, f_w, is typically truncated at 10. As *r* approaches larger values the correlation that used to calculate the *g* function goes higher which lead to the value of the wall function f_w asymptotically to one. In order to avoid large values of *r* and the larger calculated values of *g*, *r* is truncated at 10.

The trip function terms, one added to the destruction term and another one added as the last term on the RHS side, provides a control over the laminar regions of the shear layers. As suggested by Spalart [1], one aspect of the control is keeping the flow laminar where desired and the other aspect being obtaining a transition where desired. The trip functions are defined as,

$$f_{t2} = c_{t3} exp\left(-c_{t4}\chi^2\right), \tag{3.10}$$

$$f_{t1} = c_{t1} g_t exp\left(-c_{t2}\frac{\omega_t^2}{\Delta U^2}\left[d^2 + g_t^2 d_t^2\right]\right), \tag{3.11}$$

$$g_t \equiv min\left(0.1, \frac{\Delta U}{\omega_t \Delta x}\right). \tag{3.12}$$

Here d is the distance to the closest wall and d_t is the distance from the field point, local grid point, to the trip, ω_t is the wall vorticity at the trip, ΔU is the difference between the velocity at the field point and the velocity at the trip, and Δx is the grid spacing along the wall at the trip [1].

Setting up the trip functions to be zero to avoid the extra calculations in the model, the following form of the SA model in terms of the eddy viscosity, which includes eight closure coefficients and three closure functions, is implemented in the in-house codes (UNCLE and GHOST):

$$\frac{\partial \tilde{\nu}}{\partial t} + U_j \frac{\partial \tilde{\nu}}{\partial x_j} = c_{b1}\tilde{S}\tilde{\nu} - c_{w1} f_w \left(\frac{\tilde{\nu}}{d}\right)^2 + \frac{1}{\sigma}\frac{\partial}{\partial x_k}\left[(\nu + \tilde{\nu})\frac{\partial \tilde{\nu}}{\partial x_k}\right] + \frac{c_{b2}}{\sigma}\frac{\partial \tilde{\nu}}{\partial x_k}\frac{\partial \tilde{\nu}}{\partial x_k}. \tag{3.13}$$

The closure constants are given as follows:

$$\begin{gathered} c_{b1} = 0.1355, \quad c_{b2} = 0.622, \quad \sigma = \frac{2}{3}, \quad \kappa = 0.41, \\ c_{w1} = \left(\frac{c_{b1}}{\kappa^2} + \frac{1 + c_{b2}}{\sigma}\right), \quad c_{w2} = 0.3, \quad c_{w3} = 2, \quad c_{v1} = 7.1, \\ c_{t1} = 1, \quad c_{t2} = 2, \quad c_{t3} = 1.1, \quad c_{t4} = 2. \end{gathered} \tag{3.14}$$

3.2 The Two Equation Models, k-ω and k-ε

3.2.1 The k-ω Model

After the introduction of the two equation model of turbulence by Kolmogorov in 1942, many improvements were made to the *k-ω* model. The *k-ω* model by Wilcox is considered to be a standard model of this type. The first improved model of *k-ω* by Wilcox was presented in 1988 [61] and the next improved version was formulated in 1998 with new closure coefficients for the dissipation term. The *k-ω* model by Wilcox is considered to be accurate in the boundary layers. However, the older version of the Wilcox's *k-ω* is sensitive to the free stream values away from the boundary layer. The improved version of *k-ω* (1998) [6] model is considered to be superior in predictive accuracy for free shear flows to its earlier (1988) version.

For this model, the kinematic eddy viscosity is given by the following correlation,

$$\nu_T = k/\omega\,. \tag{3.15}$$

The *k-ω* transport equations are

$$\frac{\partial k}{\partial t} + U_j \frac{\partial k}{\partial x_j} = \tau_{ij} \frac{\partial U_i}{\partial x_j} - \beta^* k\omega + \frac{\partial}{\partial x_j}\left[\left(\nu + \sigma^* \nu_T\right)\frac{\partial k}{\partial x_j}\right], \tag{3.16}$$

$$\frac{\partial \omega}{\partial t} + U_j \frac{\partial \omega}{\partial x_j} = \alpha \frac{\omega}{k} \tau_{ij} \frac{\partial U_i}{\partial x_j} - \beta\omega^2 + \frac{\partial}{\partial x_j}\left[\left(\nu + \sigma\nu_T\right)\frac{\partial \omega}{\partial x_j}\right]. \tag{3.17}$$

The auxiliary equations which are required for the calculations of the functions in the *k-ω* equations are

$$\beta = \beta_o f_\beta\,, \tag{3.18}$$

$$\beta^* = \beta_o^* f_{\beta^*}\,, \tag{3.19}$$

$$f_\beta = \frac{1+70\chi_\omega}{1+80\chi_\omega}\,, \tag{3.20}$$

$$\chi_\omega = \left|\frac{\Omega_{ij}\Omega_{jk}S_{ki}}{\left(\beta_o^*\omega\right)^3}\right|, \tag{3.21}$$

$$f_{\beta^*} = \begin{cases} 1, & \chi_k \le 0 \\ \dfrac{1+680\chi_k^2}{1+400\chi_k^2}, & \chi_k > 0 \end{cases}, \tag{3.22}$$

$$\chi_k \equiv \frac{1}{\omega^3}\frac{\partial k}{\partial x_j}\frac{\partial \omega}{\partial x_j}. \tag{3.23}$$

The mean strain rate tensor is defined as $S_{ij} \equiv \frac{1}{2}\left(\frac{\partial U_i}{\partial x_j} + \frac{\partial U_j}{\partial x_i}\right)$, and the mean rotation tensor is defined as $\Omega_{ij} = \frac{1}{2}\left(\frac{\partial U_i}{\partial x_j} - \frac{\partial U_j}{\partial x_i}\right)$. The correlations for the turbulence dissipation and turbulence length scale are respectively

$$\varepsilon = \beta^* \omega k \,,\; l = k^{1/2}/\omega \,. \tag{3.24}$$

The closure constants for the *k*-ω equation are

$$\alpha = \frac{13}{25}, \qquad \sigma = \frac{1}{2}, \qquad \sigma^* = \frac{1}{2},$$

$$\beta_o = \frac{9}{125}, \qquad \beta_o^* = \frac{9}{100}. \tag{3.25}$$

The key differences between the two versions, 1988 and 1998, of the Wilcox's *k*-ω model, as mentioned by Wilcox [6], are the coefficients of the dissipation terms, β^* and β. The functions f_β and f_{β^*}, which depend on χ_ω and χ_k respectively, do not appear in the older version (1988). Also, the model constants α and β_o are recalibrated to newer values, 0.56 and 0.075, from the older values of 0.52 and 0.072 respectively. Closer to a solid boundary ω is very large, keeping χ_ω and χ_k small and hence the new dissipation coefficients have minimal effects on the boundary-layer flows. In this manner the nature of the older version in predicting the accuracy in the boundary-layer flows is retained in the new version. However, χ_ω and χ_k are significantly larger for free shear flows and hence the new version predicts more dissipation and is less sensitive to the free stream values compared to the older version.

3.2.2 The k-ε Model

The *k-ε* model is one of the most popular two equation models. The earliest development for the *k-ε* model was by Chou (1945), Davidov (1961), and Harlow and Nakayama (1968). With the efforts of Jones and Launder in 1972 the *k-ε* model had a notable improvement and was referred to as a standard *k-ε* model after that. However, the closure coefficients were revisited and corrected by Launder and Sharma in 1974 and this model is in practice the standard *k-ε* model [6].

The kinematic eddy viscosity is given by the correlation

$$\nu_T = C_\mu k^2/\varepsilon . \tag{3.26}$$

The standard *k-ε* model is given as

$$\frac{\partial k}{\partial t} + U_j \frac{\partial k}{\partial x_j} = \tau_{ij} \frac{\partial U_i}{\partial x_j} - \varepsilon + \frac{\partial}{\partial x_j}\left[\left(\nu + \nu_T/\sigma_k \right) \frac{\partial k}{\partial x_j} \right], \tag{3.27}$$

$$\frac{\partial \varepsilon}{\partial t} + U_j \frac{\partial \varepsilon}{\partial x_j} = C_{\varepsilon 1} \frac{\varepsilon}{k} \tau_{ij} \frac{\partial U_i}{\partial x_j} - C_{\varepsilon 2} \frac{\varepsilon^2}{k} + \frac{\partial}{\partial x_j}\left[\left(\nu + \nu_T/\sigma_\varepsilon \right) \frac{\partial \varepsilon}{\partial x_j} \right]. \tag{3.28}$$

The closure coefficients for the *k-ε* model are

$$C_{\varepsilon 1} = 1.44, \quad C_{\varepsilon 2} = 1.92, \quad \sigma_k = 1.0, \quad \sigma_\varepsilon = 1.3, \quad C_\mu = 0.09 . \tag{3.29}$$

The turbulence dissipation and the turbulence length scale are given by the correlations,

$$\omega = \frac{\varepsilon}{C_\mu k}, \; l = \frac{C_\mu k^{3/2}}{\varepsilon} . \tag{3.30}$$

3.3 Menter's Two Equation Turbulence Models

Menter's models are two-equation eddy viscosity turbulence models with an emphasis on the engineering perspective [62]. The basic problem of two equation models has been the prediction of the separation in adverse pressure gradient flows. In response, Menter has developed a new two-equation turbulence model based on the elements of existing models.

Menter's first choice of model was the *k-ω* [61] model which is well-behaved in the sublayer of the boundary layer and its superior compared to the *k-ε* model in the logarithmic part

of the boundary layer, especially for adverse pressure gradient flows and compressible flows. A notable disadvantage in this model [61] is its failure in predicting the asymptotic behavior of the turbulence as it approaches the wall. However, the model does retain its accuracy in predicting the mean velocity profiles and the skin friction of high-Reynolds number flows. A key disadvantage is that the model [61] is highly sensitive to the freestream values outside the boundary layer.

A new baseline model is developed on the basis of Menter's original two equation turbulence models which have the advantage of both the models. The idea is to retain the accurate formulation of the *k-ω* model in the boundary-layer region and to that add the advantage of the *k-ε* model in the region of free shear layers to reduce the sensitivity to the freestream flow. To achieve this idea the *k-ε* model is transformed into an equivalent *k-ω* formulation.

Formulation of the Baseline Model:

The original [61] *k-ω* model is

$$\frac{D\rho k}{Dt} = \tau_{ij}\frac{\partial u_i}{\partial x_j} - \beta^*\rho\omega k + \frac{\partial}{\partial x_j}\left[\left(\mu + \sigma_{k1}\mu_t\right)\frac{\partial k}{\partial x_j}\right], \tag{3.31}$$

$$\frac{D\rho\omega}{Dt} = \frac{\gamma_1}{\nu_t}\tau_{ij}\frac{\partial u_i}{\partial x_j} - \beta_1\rho\omega^2 + \frac{\partial}{\partial x_j}\left[(\mu + \sigma_{\omega 1}\mu_t)\frac{\partial \omega}{\partial x_j}\right]. \tag{3.32}$$

The transformed *k-ε* model is

$$\frac{D\rho k}{Dt} = \tau_{ij}\frac{\partial u_i}{\partial x_j} - \beta^*\rho\omega k + \frac{\partial}{\partial x_j}\left[\left(\mu + \sigma_{k2}\mu_t\right)\frac{\partial k}{\partial x_j}\right], \tag{3.33}$$

$$\frac{D\rho\omega}{Dt} = \frac{\gamma_2}{\nu_t}\tau_{ij}\frac{\partial u_i}{\partial x_j} - \beta_2\rho\omega^2 + \frac{\partial}{\partial x_j}\left[(\mu + \sigma_{\omega 2}\mu_t)\frac{\partial \omega}{\partial x_j}\right] + 2\rho\sigma_{\omega 2}\frac{1}{\omega}\frac{\partial k}{\partial x_j}\frac{\partial \omega}{\partial x_j}. \tag{3.34}$$

A blending function F_1 is introduced combine these two models. F_1 and $1-F_1$ are multiplied with the *k-ω* and the *k-ε* models respectively to obtain the baseline version. To retain the characteristics of the *k-ω* model the blending factor F_1 is set to one in the boundary-layer and the log-layer regions and gradually switches to zero in the wake region and the free shear layers to take advantage of the *k-ε* model. The eddy viscosity for the baseline model is defined as

$$v_t = \frac{k}{\omega}. \tag{3.35}$$

The definition for the shear stress tensor is given by

$$\tau_{ij} = \mu_t \left(\frac{\partial u_i}{\partial x_j} + \frac{\partial u_j}{\partial x_i} - \frac{2}{3}\frac{\partial u_k}{\partial x_k}\delta_{ij} \right) - \frac{2}{3}\rho k \delta_{ij}. \tag{3.36}$$

The combined transport equations for the baseline model are

$$\frac{D\rho k}{Dt} = \tau_{ij}\frac{\partial u_i}{\partial x_j} - \beta^* \rho \omega k + \frac{\partial}{\partial x_j}\left[(\mu + \sigma_k \mu_t)\frac{\partial k}{\partial x_j} \right], \tag{3.37}$$

$$\frac{D\rho\omega}{Dt} = \frac{\gamma}{v_t}\tau_{ij}\frac{\partial u_i}{\partial x_j} - \beta\rho\omega^2 + \frac{\partial}{\partial x_j}\left[(\mu + \sigma_\omega \mu_t)\frac{\partial \omega}{\partial x_j} \right] + 2(1-F_1)\rho\sigma_{\omega 2}\frac{1}{\omega}\frac{\partial k}{\partial x_j}\frac{\partial \omega}{\partial x_j}. \tag{3.38}$$

To generate the new closure coefficients, Menter proposed a similar blending function. If ϕ_1 and ϕ_2 represents the original *k*-ω and *k*-ε model constants respectively, then the relation between ϕ_1 and ϕ_2 and the SST model constant ϕ is given as

$$\phi = F_1\phi_1 + (1-F_1)\phi_2. \tag{3.39}$$

The closure constants for set 1 (ϕ_1) from the *k*-ω model are

$$\sigma_{k1} = 0.5, \quad \sigma_{\omega 1} = 0.5, \quad \beta_1 = 0.075, \quad \beta^* = 0.09, \quad \kappa = 0.41,$$
$$\gamma_1 = \beta_1/\beta^* - \sigma_{\omega 1}\kappa^2/\sqrt{\beta^*}. \tag{3.40}$$

The closure constants for set 2 (ϕ_2) from the *k*-ε model are

$$\sigma_{k2} = 1.0, \quad \sigma_{\omega 2} = 0.856, \quad \beta_2 = 0.0828, \quad \beta^* = 0.09, \quad \kappa = 0.41,$$
$$\gamma_2 = \beta_2/\beta^* - \sigma_{\omega 2}\kappa^2/\sqrt{\beta^*}. \tag{3.41}$$

The blending function is defined as

$$F_1 = \tanh(\arg_1^4), \tag{3.42}$$

$$\arg_1 = min\left[max\left(\frac{\sqrt{k}}{0.09\omega y}, \frac{500\nu}{y^2\omega} \right); \frac{4\rho\sigma_{\omega 2}k}{CD_{k\omega}y^2} \right], \tag{3.43}$$

where *y* is the distance to nearest surface and $CD_{k\omega}$ is the positive portion of the cross diffusion term and is given as

$$CD_{k\omega} = \max\left(2\rho\sigma_{\omega 2}\frac{1}{\omega}\frac{\partial k}{\partial x_j}\frac{\partial \omega}{\partial x_j}, 10^{-20}\right). \tag{3.44}$$

Formulation of Shear-Stress Transportation Model:

Reynolds Stress models with respect to the aerodynamic applications account for the important effect of the transport of the principal shear stress, whereas the eddy viscosity models does not account for the transport effects. The baseline model was modified to take the transport effects into effect which leads to the formulation of the Shear Stress Transport Model.

The eddy viscosity for the SST model is defined as

$$\nu_t = \frac{\alpha_1 k}{\max(\alpha_1\omega; \Omega F_2)}. \tag{3.45}$$

Otherwise the Shear Stress Transportation model is identical to the baseline formulation except for the closure constants. The closure constants for set 1 are given as follows

$$\sigma_{k1} = 0.85, \quad \sigma_{\omega 1} = 0.5, \quad \beta_1 = 0.075, \quad \beta^* = 0.09, \quad \alpha_1 = 0.31, \quad \kappa = 0.41,$$

$$\gamma_1 = \beta_1/\beta^* - \sigma_{\omega 1}\kappa^2/\sqrt{\beta^*}, \tag{3.46}$$

where Ω is the absolute value of vorticity. The blending function for the SST model is defined as

$$F_2 = \tanh(\arg_2^2), \tag{3.47}$$

$$\arg_2 = \max\left(2\frac{\sqrt{k}}{0.09\omega y}; \frac{500\nu}{y^2\omega}\right). \tag{3.48}$$

This improved version, which includes the transport effects, of the baseline model shows a significant improvement in for the flows involving adverse pressure gradients and is able to accurately predict pressure-induced separation.

3.4 Hybrid Turbulence Models

3.4.1 Formulation of DES Equations based on SA Turbulence model

The hybrid turbulence model, DES, was first formulated by Spalart [1] in 1997. Formulation of the DES model was based on the one-equation SA turbulence model. In the SA model, when the destruction term is balanced with the production term then the eddy viscosity becomes proportional to the square of the distance to the wall and to the local deformation rate, $\tilde{\nu} \propto Sd^2$. This is similar to the subgrid scale model of Smagorinsky whose eddy viscosity is proportional to the square of the grid spacing, $\nu_T \propto S\Delta^2$, where Δ is the grid spacing. Hence the basic concept that the distance closest to the wall could be replaced by the proportional length scale, Δ. The new length scale, $\tilde{l}$, is given by

$$\tilde{l} = min\left(d_w, C_{DES}\Delta\right), \tag{3.49}$$

where d_w is the distance closest to the wall, C_{DES} is the new adjustable model constant, and Δ is based on the largest dimension of the local grid cell, which is given by

$$\Delta = max\left(\delta_x, \delta_y, \delta_z\right). \tag{3.50}$$

When $d \ll \Delta$, the DES model results in a model that functions as a SA model in the attached boundary layer. When $\Delta \ll d$ the model acts as a subgrid scale model in the regions of the flow away from the wall which includes the separated regions and wake regions. One thing that can be observed is that when $\tilde{l}$ is substituted with d_w the model reduces to the standard SA model. Once the field point is away from the attached boundary layer the model becomes grid dependent and the model performs as a subgrid scale version of the SA model.

The new adjustable model constant C_{DES} is assessed by experimenting with the homogeneous turbulence requiring a reasonable behavior from the computed energy spectrum at small scales. The model constant was suggested to be on the order of 1 by Spalart [1]. The C_{DES} coefficient was calibrated to 0.65 for a homogeneous turbulence flow. This same value is used to carry out the simulation for a three dimensional turbulent flow over a circular cylinder.

Even though the formulation of the DES model has been a fairly simple process, there remains concern about the "grey area". When the SA model length scale, d_w, is on the same order of magnitude as $C_{DES}\Delta$ then the question is how the DES model behaves when these two length scales are roughly on the same order of magnitude. It is necessary to understand this "grey area" region and hence the transition point from RANS mode to LES mode becomes critical.

A shift in the grey area region is possible with the increase in number of grid points in the spanwise direction as well as when the grid is further refined in the grey area region. The extent of grid dependency of this hybrid model is to be understood with changing grids and the grid spacing.

An additional issue that arises with unstructured grids is the definition of the grid spacing. For the hexahedral grid shown, the conventional definition of Δ can be applied in a fairly direct fashion, but more complicated cell volumes (such as tetrahedral or combined hexahedral-tetrahedral) do not have that luxury. If other means of defining the grid spacing are used, the region of RANS-LES transition can shift significantly. This has implications for both the location of the grey area and the magnitude of the dissipation term in the LES region. Also, the change in the method of evaluation of the grid spacing can lead to the change in the solution. It is due to the nature of dependency of the model on the grid spacing calculation.

A correction for the DES length scale has been suggested by Spalart *et al* [66] for the flows with low Reynolds numbers. In the LES mode, the eddy viscosity normalized by the molecular viscosity decreases both with grid refinement and with low Reynolds numbers. In this case the DES length scale misinterprets the decrease due to low Reynolds numbers for that due to wall proximity, and hence reduces the eddy viscosity more than is warranted. The suggested modification in the length scale is given as

$$l_{DES} = min\left(l_{RANS}, \Psi C_{DES}\Delta\right), \tag{3.51}$$

where l_{DES} is the DES length scale, l_{RANS} is the distance closest to the wall and with C_{DES}, Δ being defined earlier, and Ψ is the correction factor introduced equivalent to $\chi \equiv \tilde{\nu}/\nu$. Under the assumption that the convection and diffusion in the turbulence transport are negligible, the subgrid model driven by the length scale, $l_{DES} = \Psi C_{DES}\Delta$, is reduced to a Smagorinsky-like model, $\tilde{\nu} = \left(C\Delta\right)^2 S$, where C is a constant.

The correlation for Ψ is given as

$$\Psi^2 = \frac{\frac{f_w}{f_w^*} - \frac{c_{b1}}{c_{w1}\kappa^2 f_w^*}\left[f_{t2} + \left(1 - f_{t2}\right) f_{v2}\right]}{f_{v1}\left(1 - f_{t2}\right)}. \tag{3.52}$$

The equilibrium function is given as

$$f_w = \phi\left(g\left[r\left(f_w, \chi\right)\right]\right), \tag{3.53}$$

$$r\left(f_w, \chi\right) = \frac{c_{b1}\left(1 - f_{t2}\right)}{c_{w1}\kappa^2 f_w - c_{b1} f_w}, \quad \phi\left(g\right) \equiv g\left(\frac{1 + c_{w3}^6}{g^6 + c_{w3}^6}\right)^{1/6}. \tag{3.54}$$

The above non-linear algebraic correlations are observed to be the functions of $\chi \equiv \tilde{\nu}/\nu$. The limiter for the equilibrium function, f_w^*, is set to 0.424.

It is observed that f_w / f_w^* is a weak function of $\tilde{\nu}/\nu$ for a range of $\tilde{\nu} > \nu/10$. Hence, the correlation for Ψ is replaced with an appropriate expression

$$\Psi^2 = min\left[10^2, \frac{1 - \frac{c_{b1}}{c_{w1}\kappa^2 f_w^*}\left[f_{t2} + \left(1 - f_{t2}\right) f_{v2}\right]}{f_{v1} max\left(10^{-10}, 1 - f_{t2}\right)}\right]. \tag{3.55}$$

The above formulation results in stronger value of Ψ for the lower values of subgrid eddy viscosity and when the subgrid eddy viscosity values are higher Ψ is inactive or 1.

3.4.2 Formulation of DES Equations based on Menter's SST Turbulence model

The DES model based on Menter's SST turbulence model was formulated by Travin, Shur, Strelets and Spalart in 2002 [59]. Though the original DES model was based on the SA model with its length scale replaced, it was argued that a DES model can be obtained from any RANS model by appropriate change in the length scale which is explicitly or implicitly involved in any RANS turbulence model. In case of Menter's SST model, the modification is applied to the *k-ω* portion of the model.

In the Menter SST model the length scale in terms of *k-ω* is given by

$$l_{k-\omega} = k^{1/2} / (\beta^* \omega). \tag{3.56}$$

Modifying the dissipative term of the k - transport equation yields

$$D_{RANS}^{k} = \rho\beta^{*} k\omega = \rho k^{3/2} / l_{k-\omega}. \tag{3.57}$$

Replacing $l_{k-\omega}$, with the DES length scale, $\tilde{l}$, given as

$$\tilde{l} = min(l_{k-\omega}, C_{DES}\Delta), \tag{3.58}$$

where C_{DES} is a model constant.

$$\Delta = max\left(\delta_x, \delta_y, \delta_z\right), \tag{3.59}$$

where Δ is the largest dimension of the local grid cell. Substituting this in the above equation to obtain

$$D_{DES}^{k} = \rho k^{3/2} / \tilde{l}, \tag{3.60}$$

and hence the DES model based on the Menter's SST model is obtained.

Coming to the correction factor for the models with low Reynolds number terms, as discussed in the earlier section, the length scale modification for the low Reynolds number terms is given as,

$$l_{DES} = min\left(l_{RANS}, \Psi C_{DES}\Delta\right). \tag{3.61}$$

3.4.3 Scale-Adaptive Simulation (SAS) Turbulence Model

Menter in 2003 presented a one-equation turbulence model (eddy-viscosity model) which is capable of resolving turbulent structures without any explicit grid dependency. Also, he argues that a reduction in the eddy viscosity allows a LES-like resolution of the turbulence flow field and that can be achieved if a natural destruction term can be added to an eddy-viscosity model. For this purpose he used the KE1E one-equation model for high Reynolds numbers, which he originally derived in [64], to demonstrate the relation between the one-equation and the two-equation models and also to explain the grid sensitivity of the Baldwin-Barth [65] one-equation model. In order to achieve the goal of demonstrating the relation between the one- and two-equation models, a *k*-*ε* model was transformed into a one equation eddy viscosity model, the KE1E model. The Baldwin Barth method was followed [64] and the time derivative of eddy viscosity, from the definition of eddy viscosity given for the *k*-*ε* model, was expressed by the time derivatives of the *k* and *ε* and hence by replacing the derivatives with the *k*-*ε* equation itself

in an appropriate manner a one-equation model was formulated. Two more equations were considered in order to close the system, out of which one was the eddy viscosity definition itself and the other the definition of the turbulent shear stress.

A von Karman length scale is adapted by this model as a scale determining variable, which determines the local scale of the flow field and hence allows the model to adapt to the length scale that is present in the flow. The model is therefore named the Scale-Adaptive Simulation (SAS) turbulence model.

The kinematic eddy viscosity definition for the KE1E model is given as

$$\nu_t = c_\mu \frac{k^2}{\varepsilon}. \tag{3.62}$$

The turbulent shear stress is

$$\left|-\overline{u'v'}\right| = \nu_t \left|\frac{\partial u_i}{\partial x_j}\right| = a_1 k\,, \tag{3.63}$$

$$a_1 = \sqrt{c_\mu},\ S = \frac{\partial u_i}{\partial x_j}. \tag{3.64}$$

The one-equation KE1E model is

$$\frac{\partial(\rho\nu_t)}{\partial t} + \frac{\partial(\rho U_j \nu_t)}{\partial x_j} = c_1 \mu_t S - c_2 \rho \left(\frac{\nu_t}{L_{vK}}\right)^2 + \frac{\partial}{\partial x_j}\left(\frac{\mu_t}{\sigma}\frac{\partial \nu_t}{\partial x_j}\right). \tag{3.65}$$

The model constants are given as

$$c_1 = 0.144, \qquad \sigma = 1, \qquad c_2 = 1.86, \qquad c_\mu = 0.09\,. \tag{3.66}$$

The von Karman length scale L_{vK} is

$$L_{vK} = \frac{(S \cdot S)}{\left(\frac{\partial S}{\partial x_j} \cdot \frac{\partial S}{\partial x_j}\right)}, \tag{3.67}$$

and the length scale in the boundary layers is

$$L_{vK} = \left|\frac{\partial U_1 / \partial x_2}{\partial^2 U_1 / \partial x_2^2}\right|, \tag{3.68}$$

where U_1 is the velocity parallel to the wall and x_2 is the coordinate normal to the surface.

A problem with the proposed length scale is a singularity occurs when it goes to zero and hence it is not successful when used in a mixing length problem. To correct this, it was argued

that as the length scale is contained in the destruction term, and so it can be limited by any other term of same dimensions. The modified destruction term is

$$c_2\rho\left(\frac{\nu_t}{L_{vK}}\right)^2 \rightarrow c_2\rho\, min\left[\left(\frac{\nu_t}{L_{vK}}\right)^2; c_{\lim}\frac{\partial \nu_t}{\partial x_j}\frac{\partial \nu_t}{\partial x_j}\right]. \tag{3.69}$$

However, after testing, it was found that the original length scale, considered to be the true size of turbulent eddies, was more promising than the limited length scale and the singularity problem had to be considered only when all the three velocity components are zero at the same location. This could be eliminated [63] by adding a small number to the denominator to insure a non-zero result and redefining the length scale to be

$$L_{vK-SAS} = \left|\frac{\frac{\partial U_i}{\partial x_j}\frac{\partial U_i}{\partial x_j}}{\frac{\partial^2 U_l}{\partial x_m^2}\frac{\partial^2 U_l}{\partial x_n^2}}\right|. \tag{3.70}$$

Replacing the original length scale with L_{vK-SAS} and rewriting the formulation yields,

$$\frac{\partial\left(\rho\nu_t\right)}{\partial t} + \frac{\partial\left(\rho U_j \nu_t\right)}{\partial x_j} = c_1\mu_t S - c_2\rho\left(\frac{\nu_t}{L_{vK-SAS}}\right)^2 + \frac{\partial}{\partial x_j}\left(\frac{\mu_t}{\sigma}\frac{\partial \nu_t}{\partial x_j}\right). \tag{3.71}$$

Finally, the length scale is modified to in order to be operated in RANS and LES modes and to give correct LES decay rates:

$$\tilde{L}_{vK-SAS} = max\left(L_{vK-SAS}, C_{SAS}\tilde{\Delta}\right), \tag{3.72}$$

$$\tilde{\Delta} = min\left(\Delta x, \Delta y, \Delta z\right),\ C_{SAS} = 0.6\,. \tag{3.73}$$

The modified length scale to operate in the RANS and LES modes is an option for the model in order to make sure of getting the correct LES decay rates. Otherwise, the SAS model is a turbulence model without an explicit grid dependency.

3.4.4 Formulation of DDES Equations based on SA Turbulence Model

The DES turbulence model can exhibit incorrect behavior in thick boundary layers and in the shallow separation region which is titled as a ‘grey area’ region. When the grid spacing parallel to the wall is less than the boundary layer thickness, the LES turbulence model takes

over as the length scale is fine enough for the DES to switch into a LES mode from RANS mode. Once the DES limiter is activated in such ambiguous grids, this limiter reduces the eddy viscosity and hence the modeled Reynolds stresses. However, the grid is not fine enough to support the LES content and also the resolved Reynolds stresses in LES mode do not completely replace the modeled Reynolds stresses from the RANS mode. This leads to the depletion of the stresses which in turn leads to the reduction in the skin friction computations leading to a premature separation.

Considering these issues with the original DES model by Spalart [1], a new version of DES called Delayed Detached Eddy Simulation (DDES) was proposed in 2006. As described by Spalart [66], DDES is a derivative of the proposed solution within the DES equations by Menter and Kuntz [67], who use the blending functions of the SST model for the identification of the boundary layers to prevent a premature switch to LES. The arguments of these functions [66], except for the low Reynolds numbers, is the ratio of the internal length scale to the closest distance to the wall, $\sqrt{k}/\omega y$. However, there is no such internal length scale present in the SA model. Instead the parameter *r*, which is ratio of model length scale to the wall distance, is modified to obtain the new model. This new version (DDES) is applicable to any eddy viscosity model with slight modifications applied to the model constants.

The correction to the parameter *r* is

$$r_d \equiv \frac{\nu_t + \nu}{\sqrt{U_{i,j}U_{i,j}}\kappa^2 d^2}, \tag{3.74}$$

and the modified parameter is used in the function

$$f_d \equiv 1 - \tanh\left(\left[8r_d\right]^3\right). \tag{3.75}$$

Here ν_t is the kinematic eddy viscosity, ν is the molecular viscosity, and the term $\nu_t + \nu$ in the numerator can be replaced by $\tilde{\nu}$ for the SA model. The term $U_{i,j}$ represents the velocity gradients, *d* is the wall distance, and κ is the von Karman constant.

The modification to the DES length scale $\tilde{d}$ to obtain the length scale for DDES version is,

$$\tilde{d} \equiv d - f_d max\left(0,\, d - C_{DES}\Delta\right). \tag{3.76}$$

Similar to the parameter *r* in the SA model, r_d shifts from 1 in the logarithmic region to 0 towards the edge of the boundary layer. To ensure that the model is in LES region, the function f_d is set to 1 in that region. However, setting f_d to 0 in the redefined length scale retains the RANS mode and setting it to 1 it retains the original DES formulation. The length scale in the one-equation SA model is the distance closest to the wall, d_w which is replaced with the modified length scale.

With the increase in popularity of DES like models, some of the grid issues are becoming apparent. These hybrid models are dependent on the grid construction and the grid spacing except for the base SAS model which is argued to be operative in the RANS and LES regions without explicit grid dependency. The overall objective of this project is to study the effects of the grid dependencies on the performance of these hybrid turbulence models in the context of three-dimensional unstructured grid code. The tools that have been developed to study these problems are detailed in the next chapter.

Chapter 4 : FLOW SOLVERS

In this chapter the two in-house codes, UNCLE and GHOST, used for the computations in this thesis will be discussed. Implementation of the Spalart-Allmaras (SA) one-equation turbulence model along with the hybrid turbulence model (DES) in the UNCLE and GHOST codes will be presented in detail. The information about the hardware that is used in these computations will be presented in brief. The two grid generation procedures that were used for carrying out theses simulations will be discussed, one using a grid generator code written in Fortran90 and the second using the commercial grid generation software, GAMBIT.

4.1 UNCLE

UNCLE is an in-house CFD code at the University of Kentucky, originally written by Dr. George Huang. It is designed to meet the challenges of physical problems with complex geometries, and complicated boundary conditions on parallel computers while maintaining high computational efficiency [68]. The laminar form of the code was validated by Dr. Chen Hua at the University of Kentucky using various test cases [69]. It is a two/three-dimensional, finite-volume, unstructured incompressible Navier-Stokes solver for steady and unsteady flow fields. It is highly flexible in terms of grid geometry as it can handle volumes of various types such as triangular, quadrilateral, tetrahedral and hexahedral. METIS [70], a program based on multilevel 26 graph partitioning schemes, is used for grid partitioning. The parallel construction of code is done using message passing interface (MPI) protocols. UNCLE relies on a cell-centered pressure-based method that is based on the SIMPLE algorithm with second order accuracy in both time and space. A second order upwind scheme is adopted to compute the advection terms and a second order central difference scheme is used for computing the diffusion terms. A collocated grid system with the Rhie and Chow momentum interpolation method [71] is employed to avoid the checkerboard solution of the pressure based scheme. Fluxes on the

volume faces are determined through interpolation of cell-centered values. The time discretization is a second-order fully implicit scheme.

In order to discuss the numerical methods in UNCLE, it will be a good starting point to revisit the governing equations in brief. The governing equations for unsteady incompressible viscous flow neglecting body forces and heat transfer are,

Mass Conservation:
$$\frac{\partial}{\partial t}\int_V \rho dV = -\oint_S \rho u_i n_i dS\,, \tag{4.1}$$

Momentum Conservation:
$$\frac{\partial}{\partial t}\int_V \rho u_j dV = -\oint_S \rho u_i u_j n_i dS - \oint_S p n_j dS + \oint_S \tau_{ij} n_i dS\,, \tag{4.2}$$

Energy Conservation:
$$\frac{\partial}{\partial t}\int_V \rho E dV = -\oint_S \rho u_i n_i E dS - \oint_S p u_j n_j dS + \oint_S u_j \tau_{ij} n_i dS\,, \tag{4.3}$$

where specific internal energy is $E = e + \frac{1}{2}\left(u^2 + v^2 + w^2\right)$. Here, ρ is the density, u_i are the velocity vector components, n_i is the unit normal vector of the interface, p is the pressure, and τ_{ij} is the tensor of shear stress force.

Convective and Diffusive Fluxes:

In Figure 4-1, P_1, P_2 and V_1, V_2 represent the node and the vertex points of a face respectively. Here, (ξ,η) are the coordinates in the direction of P_1 to P_2 and V_1 to V_2 respectively. The third dimension, say for a hexahedral cell which has four vertices for a face, ζ is the direction vector pointing into the paper and V_1, V_2, V_3, V_4 are the vertices of a four sided face with V_3 behind V_1 and V_4 behind V_2. The code follows a left hand thumb rule convention, when the index finger of the left hand is placed in the direction of the vertices, say from V_1 to V_2 then the thumb of the left hand represents the direction of the node points to be considered, that is P_1 to P_2. UNCLE can handle four kinds of cell structures: triangular, quadrilateral, tetrahedral, and hexahedral; however, this thesis will focus on simulations using grids with quadrilateral and hexahedral cells. The integration volumes and areas vary with the varying cell structures.

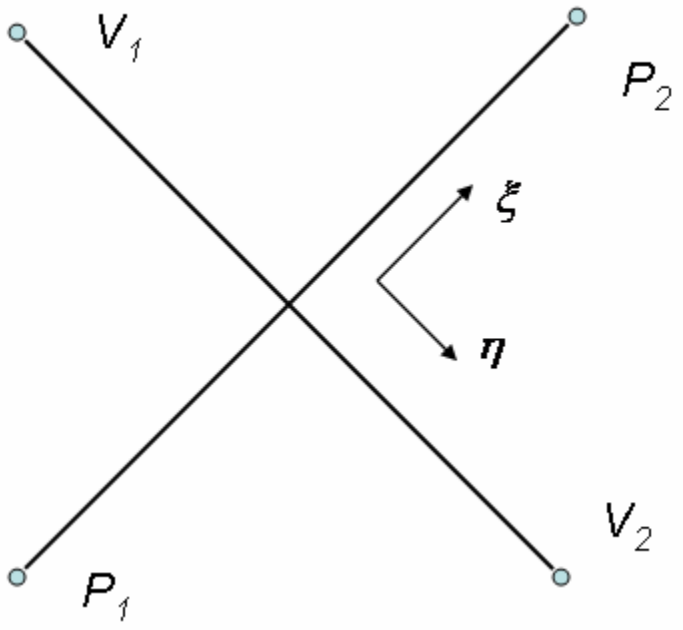

Figure 4-1 Left-Hand Thumb rule Convention for a control volume cell

Taylor series expansion is used to obtain the flow properties at the interfaces. The equations are

$$\phi^{LHS} = \phi_{P_1} + \left.\frac{\partial \phi}{\partial x}\right|_{P_1} \left(x_f - x_{P_1}\right) + \left.\frac{\partial \phi}{\partial y}\right|_{P_1} \left(y_f - y_{P_1}\right) + \left.\frac{\partial \phi}{\partial z}\right|_{P_1} \left(z_f - z_{P_1}\right) + HOT\,, \tag{4.4}$$

$$\phi^{RHS} = \phi_{P_2} + \left.\frac{\partial \phi}{\partial x}\right|_{P_2} \left(x_f - x_{P_2}\right) + \left.\frac{\partial \phi}{\partial y}\right|_{P_2} \left(y_f - y_{P_2}\right) + \left.\frac{\partial \phi}{\partial z}\right|_{P_2} \left(z_f - z_{P_2}\right) + HOT\,, \tag{4.5}$$

where ϕ represents any of the scalar quantities and velocity vector components, while the subscripts P_1 and P_2 represent the node points of a face and V_1 and V_2 correspond to the vertices of the same face. The vertices follow the left hand thumb rule convention. The superscripts LHS and RHS are for the left (P_1) and right (P_2) hand sides of the face (interface) and HOT stands for higher order terms.

The equation that can be used to obtain the flow properties at the face is

$$\phi_f = \frac{1}{2}\left(\phi^{LHS} + \phi^{RHS}\right) - \frac{1}{2} sign\left(1, \dot{m}\right)\left(\phi^{LHS} + \phi^{RHS}\right). \tag{4.6}$$

Gauss's divergence theorem is used to calculate the gradients at the cell centers

$$\int_V \frac{\partial \phi}{\partial x_i} dV = \int_A \phi n_i dA\,, \tag{4.7}$$

$$\frac{\partial \phi}{\partial x_i} \approx \frac{\sum_{k=1}^{N_{face}} \phi n_{i,k} A_k}{V}, \tag{4.8}$$

where ϕ is the flow property to be calculated at the cell center, V is the volume of the cell, A is the area of face, n_i is the unit normal vector of the interface, and N_{face} is the total number of faces corresponding to the cell for which the flow property is being calculated. For diffusive fluxes, gradients at the interface can be evaluated using the following equations:

$$\begin{aligned}
\frac{\partial \phi}{\partial x} &= \frac{\partial \phi}{\partial \xi}\frac{\partial \xi}{\partial x} + \frac{\partial \phi}{\partial \eta}\frac{\partial \eta}{\partial x} + \frac{\partial \phi}{\partial \zeta}\frac{\partial \zeta}{\partial x}, \\
\frac{\partial \phi}{\partial y} &= \frac{\partial \phi}{\partial \xi}\frac{\partial \xi}{\partial y} + \frac{\partial \phi}{\partial \eta}\frac{\partial \eta}{\partial y} + \frac{\partial \phi}{\partial \zeta}\frac{\partial \zeta}{\partial y}, \\
\frac{\partial \phi}{\partial z} &= \frac{\partial \phi}{\partial \xi}\frac{\partial \xi}{\partial z} + \frac{\partial \phi}{\partial \eta}\frac{\partial \eta}{\partial z} + \frac{\partial \phi}{\partial \zeta}\frac{\partial \zeta}{\partial z}.
\end{aligned} \tag{4.9}$$

Cell-Centered Pressure method based on SIMPLE algorithm:

As mentioned before, UNCLE uses the SIMPLE algorithm. A cell centered pressure based method is built on the SIMPLE algorithm with second order accuracy in both time and space. An initial pressure field P^n is used to obtain $u^n, v^n,$ and w^n by solving the momentum equations in a sequential manner. The delta form is used for the solution method on the LHS terms and the momentum equations can be written

$$\begin{aligned}
a_p \Delta u &= \sum_{nb} a_{nb} \Delta u + RHS_u, \\
a_p \Delta v &= \sum_{nb} a_{nb} \Delta v + RHS_v, \\
a_p \Delta w &= \sum_{nb} a_{nb} \Delta w + RHS_w,
\end{aligned} \tag{4.10}$$

where the subscript p denotes the cell (node point) to be solved, a_p is the coefficient at the cell center, and a_{nb} represents the coefficient of each individual neighbor of that cell. The coefficients a_p and a_{nb} are

$$a_p = \sum_{nb} a_{nb}, \tag{4.11}$$

$$a_{nb} = max\left(-\dot{m}_f, 0\right) + \mu_f \left(\xi_x n_1 + \xi_y n_2 + \xi_z n_3\right) A, \tag{4.12}$$

where A is the area of the interface, ξ_x, ξ_y, ξ_z represent the local coordinate system on the interface, and $\dot{m}_f$ is the mass flux at the interface. The RHS terms are

$$\begin{aligned}
RHS_u &= -\sum_{i=1}^{N_{face}} \left[\dot{m}_i u_i^n - \left(\tau_{11}^n - p^n\right)_i n_{i,1} A_i - \left(\tau_{21}^n\right)_i n_{i,2} A_i - \left(\tau_{31}^n\right)_i n_{i,3} A_i \right], \\
RHS_v &= -\sum_{i=1}^{N_{face}} \left[\dot{m}_i v_i^n - \left(\tau_{12}^n\right)_i n_{i,1} A_i - \left(\tau_{22}^n - p^n\right)_i n_{i,2} A_i - \left(\tau_{32}^n\right)_i n_{i,3} A_i \right], \\
RHS_w &= -\sum_{i=1}^{N_{face}} \left[\dot{m}_i w_i^n - \left(\tau_{13}^n\right)_i n_{i,1} A_i - \left(\tau_{23}^n\right)_i n_{i,2} A_i - \left(\tau_{33}^n - p^n\right)_i n_{i,3} A_i \right].
\end{aligned} \tag{4.13}$$

The momentum equations represented in first order delta form are solved using Gauss-Seidel point substitution. After this, the velocities at the current time step are given by

$$u^* = u^n + \Delta u, \quad v^* = v^n + \Delta v, \quad w^* = w^n + \Delta w. \tag{4.14}$$

However, the velocity obtained from solving the momentum equations does not necessarily satisfy the continuity equations. For this reason, the velocity is interpolated on to the interface and in order to get rid of checkerboard solutions the velocity at the interface needs to be solely driven by the pressure difference which is directly evaluated at the interface. To achieve this, interpolated interfacial velocity is divided into two components: the velocity component without the contribution of pressure and the velocity component with the contribution of pressure. The former is evaluated at the cell center by

$$\tilde{u}^* = u^* + \frac{\partial p^n}{\partial x}\frac{V_p}{a_p}, \quad \tilde{v}^* = v^* + \frac{\partial p^n}{\partial y}\frac{V_p}{a_p}, \quad \tilde{w}^* = w^* + \frac{\partial p^n}{\partial z}\frac{V_p}{a_p}, \tag{4.15}$$

and then are interpolated on to the faces of that cell. The latter is obtained from the pressure difference of the adjacent nodal points, P_1 and P_2, such that the velocity at interface is expressed by

$$u_f^* = \tilde{u}_f^* - \left(\frac{\partial p^n}{\partial x}\right)_f \frac{V_f}{a_f}, \quad v_f^* = \tilde{v}_f^* - \left(\frac{\partial p^n}{\partial y}\right)_f \frac{V_f}{a_f}, \quad w_f^* = \tilde{w}_f^* - \left(\frac{\partial p^n}{\partial z}\right)_f \frac{V_f}{a_f}. \tag{4.16}$$

Here, the ratio of the volume to the area, V_f / a_f, at the face is obtained by interpolating the volume to area ratio of the cell on to the face.

In order to satisfy the continuity equation, corrections are added to the velocities evaluated at the interface as given above. After adding the corrections to the velocities they are substituted into the continuity equation

$$\sum_{i=1}^{N_{face}} \rho\left[\left(u_f^* + \Delta u_f'\right)n_1 + \left(v_f^* + \Delta v_f'\right)n_2 + \left(w_f^* + \Delta w_f'\right)n_3\right]A = 0\,,$$

$$\Rightarrow \sum_{i=1}^{N_{face}} \rho\left[\Delta u_f' n_1 + \Delta v_f' n_2 + \Delta w_f' n_3\right]A = -\sum_{i=1}^{N_{face}} \rho\left[u_f^* n_1 + v_f^* n_2 + w_f^* n_3\right]A\,, \tag{4.17}$$

where the RHS represents the mass imbalance in the control volume cell. One then assumes that there is a corresponding pressure correction field p' that drives the velocity corrections according to

$$\begin{aligned}
\Delta u_f' &\approx -\left(\frac{\partial p'}{\partial x}\right)_f \left(\frac{V}{a}\right)_f \\
&= \left(\frac{V}{a}\right)_f \left[\left(p_{P_2}' - p_{P_1}'\right)\xi_x + \left(p_{V_2}' - p_{V_1}'\right)\eta_x\right] \qquad (4.18)\\
&\approx \left(\frac{V}{a}\right)_f \left[\left(p_{P_2}' - p_{P_1}'\right)\xi_x\right],
\end{aligned}$$

$$\begin{aligned}
\Delta v_f' &\approx -\left(\frac{\partial p'}{\partial y}\right)_f \left(\frac{V}{a}\right)_f \\
&= \left(\frac{V}{a}\right)_f \left[\left(p_{P_2}' - p_{P_1}'\right)\xi_y + \left(p_{V_2}' - p_{V_1}'\right)\eta_y\right] \qquad (4.19)\\
&\approx \left(\frac{V}{a}\right)_f \left[\left(p_{P_2}' - p_{P_1}'\right)\xi_y\right],
\end{aligned}$$

$$\begin{aligned}
\Delta w_f' &\approx -\left(\frac{\partial p'}{\partial z}\right)_f \left(\frac{V}{a}\right)_f \\
&= \left(\frac{V}{a}\right)_f \left[\left(p_{P_2}' - p_{P_1}'\right)\xi_z + \left(p_{V_2}' - p_{V_1}'\right)\eta_z\right] \qquad (4.20)\\
&\approx \left(\frac{V}{a}\right)_f \left[\left(p_{P_2}' - p_{P_1}'\right)\xi_z\right].
\end{aligned}$$

The equations for the pressure correction are obtained by substituting the velocity correction equations into the mass imbalance equation,

$$a_p p_p' = \sum_{nb} a_{nb} p_{nb}' + b\,, \tag{4.21}$$

where $$a_p = \sum_{nb} a_{nb}, \quad a_{nb} = \rho\left[\left(\frac{V}{a}\right)_f \xi_x n_1 + \left(\frac{V}{a}\right)_f \xi_y n_2 + \left(\frac{V}{a}\right)_f \xi_z n_3\right] A\,, \tag{4.22}$$

$$b = -\sum_{nb} \rho\left[u_f^* n_1 + v_f^* n_2 + w_f^* n_3\right] A\,. \tag{4.23}$$

Now that the pressure correction has been obtained, the pressure field can be updated,

$$p_P^{n+1} = p^n + \alpha_p p'\,, \tag{4.24}$$

where α_p is the under-relaxation factor for pressure and its range is typically 0.5-0.8. Then the velocity correction on the interfaces as well as the nodal points is updated.

Time Discretization:

A second order fully implicit scheme is employed for time discretization. Consider a one-dimensional example

$$\frac{3\phi^{n+1} - 4\phi^n + \phi^{n-1}}{2\Delta t} + \frac{\partial f\left(\phi^{n+1}\right)}{\partial x} = 0\,, \tag{4.25}$$

where ϕ is a primitive variable, f is the interfacial flux, and n indicates the index in time. In order to obtain ϕ^{n+1}, a deferred iterative algorithm is employed,

$$\left(\phi^{n+1}\right)^{m+1} = \left(\phi^{n+1}\right)^m + \left(\Delta\phi\right)^m\,. \tag{4.26}$$

Here, m represents the subiteration level. Substituting (4.26) equation in the (4.25) equation yields

$$\frac{3\left(\Delta\phi\right)^m}{2\Delta t} + \frac{\partial f\left(\Delta\phi\right)^m}{\partial x} = \frac{\phi^n - \phi^{n-1}}{2\Delta t} - \frac{3\left(\left(\phi^{n+1}\right)^m - \phi^n\right)}{2\Delta t} - \frac{\partial f\left(\phi^{n+1}\right)^m}{\partial x}\,. \tag{4.27}$$

The LHS of the above equation is evaluated based on the first order upwind differencing scheme and the RHS is recognized as explicit and is implemented in a straightforward manner to discretize the spatial derivative term. The solution for ϕ^{n+1} is obtained by using inner iterations to reach a converged solution for the RHS and at least one subiteration is performed at every time step so the method is fully implicit.

Partitioning Approach using METIS:

METIS [70] is the partitioning approach used to divide the unstructured grid for the cell centered pressure based method. It can partition an unstructured grid into any number of zones and is compatible with many platforms, convenient for running CFD codes on supercomputers to a variety of cluster architectures. This approach does not split the control volumes on the boundaries but communication of the nodal values at these boundaries is needed. For this reason the Message Passing Interface (MPI) is implemented in this unstructured grid code for parallel computation or the communication of the nodal values. An excellent load balancing between the partitioned grids is achieved by METIS [70].

4.1.1 Implementation of SA Model in UNCLE

In UNCLE code, the Menter's SST turbulence model was implemented previously. However, in order to carry out the simulations for the hybrid turbulence model, DES, the one-equation Spalart-Allmaras model is implemented in the UNCLE code. For convenience, the SA equation is presented,

$$\frac{\partial \tilde{\nu}}{\partial t}+U_j\frac{\partial \tilde{\nu}}{\partial x_j}=\underbrace{c_{b1}\tilde{S}\tilde{\nu}}_{\text{Production}}-\underbrace{c_{w1}f_w\left(\frac{\tilde{\nu}}{d}\right)^2}_{\text{Destruction}}+\underbrace{\frac{1}{\sigma}\frac{\partial}{\partial x_k}\left[(\nu+\tilde{\nu})\frac{\partial \tilde{\nu}}{\partial x_k}\right]}_{\text{Diffusion}}+\underbrace{\frac{c_{b2}}{\sigma}\frac{\partial \tilde{\nu}}{\partial x_k}\frac{\partial \tilde{\nu}}{\partial x_k}}_{\text{Diffusion-II}}. \tag{4.28}$$

The convective fluxes and the diffusive fluxes are treated similar to the velocity field, discussed in the previous section. The discretization of the turbulence equation is similar to the momentum equations except for the treatment of the right hand side which will be discussed here. The equation is solved in delta form and the time discretization is second order fully implicit.

Similar to the momentum equations, the turbulence equation is evaluated in delta form,

$$a_p\Delta\tilde{\nu}=\sum_{nb}a_{nb}\Delta\tilde{\nu}+\underbrace{RHS}_{\textbf{Source}}, \tag{4.29}$$

$$a_p = \underbrace{\frac{Loss\ Term}{\tilde{\nu}}}_{\text{For Stability}} + \sum_{nb} a_{nb}\,, \tag{4.30}$$

$$a_{nb} = max\left(\text{-}\dot{m}_f, 0\right) + \left(\nu + \tilde{\nu}\right)\left(\xi_x n_1 + \xi_y n_2 + \xi_z n_3\right) A\,, \tag{4.31}$$

$$RHS = c_{b1}\tilde{S}\tilde{\nu} - c_{w1} f_w \left(\frac{\tilde{\nu}}{d}\right)^2 + \frac{c_{b2}}{\sigma}\frac{\partial \tilde{\nu}}{\partial x_k}\frac{\partial \tilde{\nu}}{\partial x_k}\,. \tag{4.32}$$

The coefficients of the neighboring cells are evaluated similar to the momentum equations, however the loss term divided by the transport equation variable similar to eddy viscosity is added to the coefficient of the local cell a_p to increase numerical stability. The right-hand side of the discretized equation, which is the source term, is formed by the production term, destruction term, and one of the diffusion terms. The equation is solved for $\Delta\tilde{\nu}$ and the turbulent viscosity, $\nu_T = \tilde{\nu} f_{v1}$, is evaluated and is updated to solve the momentum equation for the next time step. It should be mentioned that turbulence equations are solved after the momentum and continuity equations are solved in a given subiteration, so they are staggered.

4.1.2 Implementation of SAS Model in UNCLE

In addition to the SA model, and SA-DES model in the UNCLE code, the Scale Adaptive Simulation (SAS) hybrid turbulence was implemented in the UNCLE model. The SAS model, as mentioned earlier, is argued to be a hybrid turbulence model which is not explicitly grid dependent like the DES hybrid turbulence model. The purpose of implementing was to study the behavior of this model and compare it with the DES model. Revisiting the SAS model,

$$\frac{\partial \nu_t}{\partial t} + \frac{\partial\left(U_j \nu_t\right)}{\partial x_j} = \underbrace{c_1 \nu_t S}_{Production} \underbrace{- c_2 \left(\frac{\nu_t}{L_{vK-SAS}}\right)^2}_{Destruction} + \underbrace{\frac{\partial}{\partial x_j}\left(\frac{\nu_t}{\sigma}\frac{\partial \nu_t}{\partial x_j}\right)}_{Diffusion} \tag{4.33}$$

The convective and diffusive fluxes in the equation are discretized and treated in the same way as that of the momentum equations. It can be observed from equation (4.33) that it has a production term, a destruction term, and a diffusion term. The SAS model has the same form as the SA model and hence the discretization of the SAS equation is similar to the SA model except that it has a double derivative term in the length scale which requires an extra effort. The equation is solved in the delta form and the time discretization is second order fully implicit.

The discretized equation is solved in delta form as

$$a_p \Delta \nu_t = \sum_{nb} a_{nb} \Delta \nu_t + \underbrace{RHS}_{\text{Source}}, \tag{4.34}$$

$$a_p = \underbrace{\frac{Loss\ Term}{\nu_t}}_{\text{For Stability}} + \sum_{nb} a_{nb}, \tag{4.35}$$

$$a_{nb} = max\left(-\dot{m}_f, 0\right) + \left(\nu_t\right)\left(\xi_x n_1 + \xi_y n_2 + \xi_z n_3\right) A, \tag{4.36}$$

$$RHS = c_1 \nu_t S - c_2 \left(\frac{\nu_t}{L_{vK-SAS}} \right)^2, \tag{4.37}$$

$$L_{vK-SAS} = \left| \frac{\dfrac{\partial U_i}{\partial x_j} \dfrac{\partial U_i}{\partial x_j}}{\dfrac{\partial^2 U_l}{\partial x_m^2} \dfrac{\partial^2 U_l}{\partial x_n^2}} \right|. \tag{4.38}$$

The Gauss's divergence theorem is used to evaluate the double derivative terms in the length scale calculation. The approach used to calculate the first and second derivatives is

$$\int_V \frac{\partial \phi}{\partial x_i} dV = \int_A \phi n_i dA, \tag{4.39}$$

$$\frac{\partial \phi}{\partial x_i} \approx \frac{\sum_{k=1}^{N_{face}} \phi n_{i,k} A_k}{V}, \tag{4.40}$$

$$\frac{\partial^2 \phi}{\partial x_i^2} \approx \frac{\sum_{k=1}^{N_{face}} \dfrac{\partial \phi}{\partial x_i} n_{i,k} A_k}{V}. \tag{4.41}$$

The discretized equation is solved in the delta form for $\Delta \nu_t$ and ν_t is updated to solve the momentum equation. As mentioned earlier, the turbulence variables are solved after solving the momentum and continuity equations.

4.2 GHOST

GHOST is a two-dimensional, finite volume, steady/unsteady, incompressible Navier-Stokes solver. It uses standard chimera overset grids for parallel computing. GHOST is a very well established code which was tested for a variety of test cases including transitional turbo machinery flows and active flow control. It uses QUICK scheme with second order accuracy to discretize the advection terms and a second order central differencing scheme for the diffusive terms. The advection terms in the turbulence equations (RANS models) are evaluated by the Total Variation Diminishing (TVD) scheme. The cell-centered values are interpolated onto the interfaces in order to obtain the interfacial fluxes. A second order upwind time discretization is employed for the temporal terms, using a delta form sub-iterative scheme. GHOST was also designed to minimize memory usage which was accomplishes through extensive use of the allocation and de-allocation of variables in FORTRAN90. It uses a cell-centered partitioning approach and the internode communication protocol is MPI. It has mechanisms to do a form of automatic load balancing. Similar to UNCLE, GHOST uses a second order fully implicit method for time discretization.

GHOST is designed to use structured grids and the variables are stored in individual arrays in *i, j* format, for example, $\phi_1, \phi_2, \phi_3 ..... \phi_n$. For a structured grid, the majority of calculations are performed as a series of bi-directional sweeps in nested double loops. The matrices resulting from each subiteration based on the QUICK and TVD schemes as well as evaluation of source/sink terms are solved with ADI-type decomposition into a pair of sweeps alternately in *i-* , *j-* directions which are solved sequentially in tri-diagonal matrices. Unlike UNCLE which uses a Gauss-Seidel point solver, GHOST uses a TDMA solver, which solves a tri-diagonal matrix.

The one-equation Spalart-Allmaras turbulence model and the hybrid turbulence model, DES were implemented in the GHOST code for cross validation with UNCLE.

4.3 HARDWARE DETAILS - KENTUCKY FLUID CLUSTERS

The Kentucky Fluid Clusters, shortly called the KFC systems, are housed at the University of Kentucky. Even though most of the computational work for this thesis is carried out on the KFC4 and the KFC5 platforms, the details of the earlier machines KFC1 and KFC2 will also be presented to make the readers aware of the increasing computer power and the efforts taken to keep up with the current trends in computer architectures.

KFC1: Year of construction of this machine is spring 2001. This machine had 20 dual AMD nodes. Each node having two 1.4 GHz Athlon MP Processors with 384MB RAM per processor and 40GB of disk space for each node.

KFC2: This machine has been operational since February 2003 and currently housed at the UK KAOS. It contained 47 nodes (including 3 spare nodes) with 50 2000+ XP Athlon processors and 256MB RAM per processor. A channel-bonded network with four 48-way switches, four NICs per node was used. But now it is cut down to 24 nodes.

KFC4: This machine has been operational since February 2004 and is currently housed in the UK CFD Cluster room. It has 48 nodes with AMD Athlon XP 2500+ 1.826 GHz 32 bit Barton processor on each node (1 processor per node) and 512 MB RAM per processor. The nodes are linked by two networks: a single Fast Ethernet 100 Mb/s switch and a single Gigabit 1 Gb/s switch.

KFC5: This machine became operational in September 2005 and is currently housed in the UK CFD Cluster room. It has 47 nodes with AMD Athlon 2.08 GHz 64 bit processor on each node (1 processor per node) and 512 MB RAM per processor. It uses a single Gigabit 1 Gb/s switch for networking purposes.

KFC6I: This machine became operational in December 2006 and is currently housed in the UK CFD Cluster room. It consists of 24 nodes with Intel e6400 Core 2 Duo 2.13 GHz 64 bit 2MB shared L2 Cache processor on each node (1 processor per node) and 1 GB RAM per processor. It uses a single 48 port Gigabit 1 Gb/s switch for networking purposes.

KFC6A: This machine was also operational in December 2006 and is currently housed in the UK CFD Cluster room. It contains 23 nodes with AMD Athlon 64x2 4600+ (65W) 2.4 GHz 2x512Kb Cache (socket AM2) processor on each node (1 processor per node) and 1 GB RAM per processor (DDR2 667MHz). It uses a single 24 port Gigabit 1 GB/s switch for networking.

Figure 4-2 Kentucky Fluid Clusters – UK CFD Cluster Room

A photo of the UK CFD Cluster room is presented in Figure 4-2. One of the three dimensional simulations in this thesis use an unstructured grid (hexahedral cells) with 1084800 grid points and partitioned into 18 zones using METIS. On the KFC5 machine (one zone per node) it takes about 14 hours of wall time to run 2000 iterations with an active turbulence model. On the same grid with same number of partitions it takes about twice the CPU time on KFC4 compared to the KFC5 system. The final time step that is typically used for these runs is $5x10^{-4}$. The huge 3D computations are mainly carried out on KFC5 due to superior speed, while for carrying out the validation process, the KFC4 platform suffices.

4.4 GRID GENERATION

4.4.1 Grid Generation with g.f90 and plot3d.f90

The grid issues with the recently developed hybrid turbulence models, DES and DDES, put more emphasis on the grid generation process. It is definitely necessary to have highly controlled grids in order to study the transition from the RANS to LES regions. Even though grid generation software like GAMBIT is sufficient for a general grid, finer control over the exact grid structure is desirable. For this reason the in-house grid generation codes g.f90 and plot3d.f90 are modified to generate a 2D/3D unstructured grid that is readable by UNCLE.

Grid Generator code, g.f90:

The *g.f90* code is the in-house grid generator which is used to generate 2D grids for the GHOST code. This code uses a Cartesian coordinate system that is capable of varying the stretching ratios and hence making the grid generation more flexible. Geometries ranging from simple to complicated can be generated from the code, for example, grid for a flat plate, grid for a cylinder, and grid for airfoils. It has the facility of partitioning the grids by mentioning the grid sizes, the boundaries, and the number of zones in the input file for the g.f90 code. Individual subroutines are used for generating different kinds of grids. For generating a grid for the present task a subroutine called *"qcirc"* was added. The subroutine works individually and the only input needed is the number of control volume cells and the boundary conditions. The other required quantities like the coordinate system including the stretching ratios are calculated by the subroutine itself. The grid starts from a circular form and stretches out to a square; the reason for adopting this kind of grid generation is that the boundary conditions can be applied in a fairly direct fashion. The input file, with comments, for generating a 3D grid from g.f90 with the subroutine *"qcirc*" is given in Table 4-1.

Apart from the grid files for GHOST, the code outputs a plot3d.plt file which is an input file for plot3d.f90.

Table 4-1 Input file for g.f90 (for generating the circle extended to quadratic grid)

```
/*3D !A THREE DIMENSIONAL GRID
      !SPACE
 0.3 5 peri ! 0.3- Z-SPACING, 5- NUMBER OF GRID POINTS IN Z-DIRECTION, PERI- PERIODIC BOUNDARIES
IN SPANWISE DIRECTION
 /*number_of_zone ! SPECIFY NUMBER OF ZONES
 1  !THE QCIRCLE IS A SINGLE ENTITY, SO 1
 /*zone_number 1 ! WHICH ZONE ARE WE IN? ITS FIRST
      !SPACE
 qcircle 159 100 5 2 ! QCIRCLE- G.F90 IDENTIFIES THE QCIRC ROUTINE, 159,100- GRID PTS IN I- & J-
DIRECTION, 5- BC'S, 2- GHOST PTS
 0.0 0.00024166042529 ! CENTER COORDINATES
 0.0 360.0 0.5 8 !
 0.0 0.0 w 0.0 !
 1.00 1.0   !STRETCHING RATIO FOR CYLINDER
 * wall 0 1 -99999 100000 1 1 0       ! WALL BC, 0 1 - SPECIFIES DIRECTION,FROM I= -99999 TO I=
100000, FROM J= 1 TO J= 1, 0- NO PATCHES
 * inlet   0 -1 60 100 99999 99999 0 ! INLET BC
 * outflow 0 -1 1  20 99999 99999 0 ! OUTFLOW BC
 * outflow 0 -1 20 60 99999 99999 0 ! OUTFLOW BC
 * outflow 0 -1 100 160 99999 99999 0 ! OUTFLOW BC
 /end ! END OF THE INPUT FILE
```

Grid Generator code, plot3d.f90:

As mentioned earlier, plot3d.f90 needs an input file plot3d.plt which is generated from g.f90. The code needs information about the coordinate system, the total number of control volume cells, and the boundary conditions. It outputs the input files needed by UNCLE which uses unstructured grids. The code can handle both 2D and 3D grids. As the grid generated for the present study follows unique directions in sweeping in the *i*-, *j*- directions, it was required to modify the code in order to account for such changes. The code was modified both for 2D and 3D versions in the code. The output files *"cell.dat"*, *"face.dat", "vertex.dat",* and their format along with explanation are briefly presented in Table 4-2.

Table 4-2 Input files for UNCLE (Unstructured grid)

Cell.dat

```
!Total cell number       !Grid type
       62964       95718   3D
```

Vertex.dat

```
       79500 ! Total number of vertices
!Vertex Number       x                       y                    z
           1  0.500000000000000        0.00000000000000D+000   0.00000000000000D+000
           2  0.499572879193651        2.06624871244066D-002   0.00000000000000D+000
           3  0.498292246503335        4.12896727361662D-002   0.00000000000000D+000

           .         .                       .                       .
```

Face.dat

```
      172515 ! Total number of faces
!Vertices number            {Vertex numbers for a face}           {Node numbers for face}
!surrounding a face  V1          V2            V3         V4           P1         P2
           4       16060       15901           1         160           1         159
           4       16061       15902           2         161           2           1
           4       16062       15903           3         162           3           2
           .         .           .             .           .           .           .
           7 ! Total number of Boundary Conditions
         636  wall* * ! Total number of wall boundary conditions
           4       15902       15901           1           2       62965           1
           .         .           .             .           .           .           .
         160  inle* * ! Total number of inlet boundary conditions
           4       31701       31702       15802       15801       63601       15642
           .         .           .             .           .           .           .
         240  outf* * ! Total number of outflow boundary conditions
           4       31742       15842       15841       31741       63997       15682
           .         .           .             .           .           .           .
          76  outf* * ! Total number of outflow boundary conditions
           4       31643       15743       15742       31642       63761       15583
           .         .           .             .           .           .           .
         160  outf* * ! Total number of outflow boundary conditions
           4       31661       31662       15762       15761       63837       15602
           .         .           .             .           .           .           .
       15741  peri * 1 0.0 0.0 0.3 ! Total number of Periodic BC's in SPANWISE (+Z) direction
           4         161           2           1         160       64237           1       79978
           .         .           .             .           .           .           .         .
       15741  peri * 1 0.0 0.0 -0.3 ! Total number of Periodic BC's in SPANWISE (-Z) direction
           4       63761       63760       63601       63602       79978       47224       64237
           .         .           .             .           .           .           .         .
```

The 2D cylinder grid generated from the g.f90 and plot3d.f90 codes is presented in Figure 4-3. For a 3D model, the grid spacing is uniform in the spanwise direction, so a 3D grid can be thought of as a series of 2D grids placed at equal distances. In order to confirm the functioning of this grid for UNCLE, it was necessary to validate the grid against benchmark results. The validation was carried out for a simpler laminar flow with Reynolds number, Re_D = 100 for both 2D and 3D grids and the results are compared with the Hua *et al* [69] results on UNCLE using a GAMBIT generated grid.

Table 4-3 Boundary conditions for Laminar test case

	2D simulation	3D simulation
Initial condition	$u=1; v=0; p=0$	$u=1; v=0; w=0; p=0$
Boundary conditions	Inflow: $u=1; v=0; \partial p/\partial x_i=0$ Outflow: $\partial u/\partial x_i=0; \partial v/\partial x_i=0; \partial p/\partial x_i=0$ Wall: $u=0; v=0; \partial p/\partial x_i=0$	Inflow: $u=1; v=0; w=0; \partial p/\partial x_i=0$ Outflow: $\partial u/\partial x_i=0; \partial v/\partial x_i=0; \partial w/\partial x_i=0; \partial p/\partial x_i=0$ Wall: $u=0; v=0; w=0; \partial p/\partial x_i=0$ spanwise is periodic

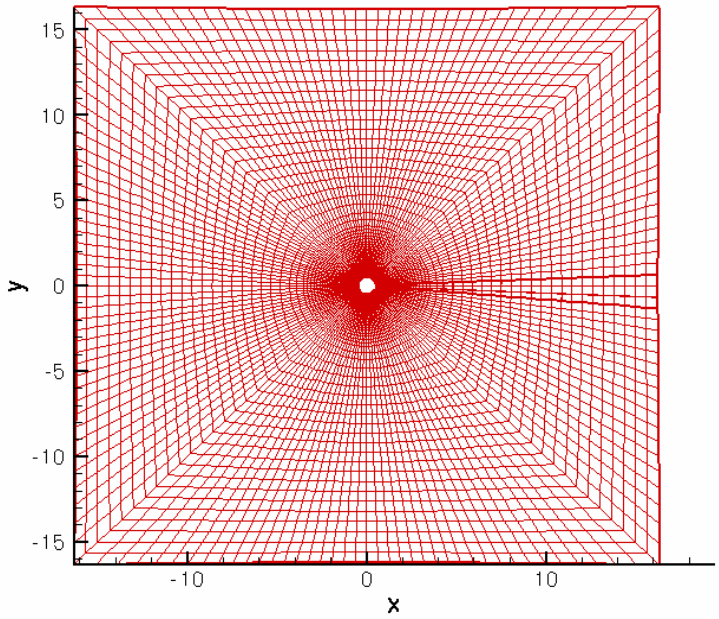

Figure 4-3 2D Grid Generated from G.F90

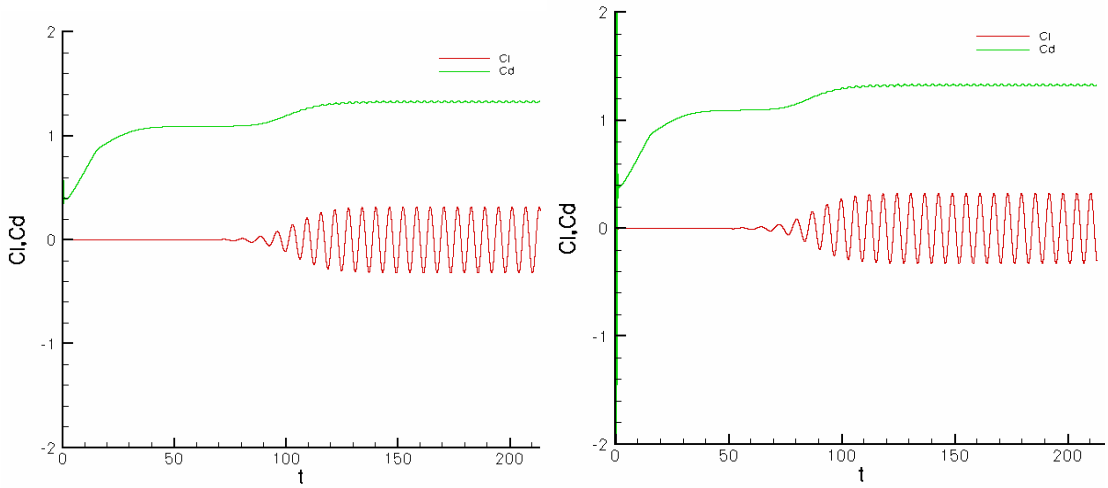

Figure 4-4 (a) Lift-Drag plot for 2D cylinder Re_D=100 (b) Lift-Drag plot for 3D cylinder Re_D=100

It can be observed from the results presented, in Table 4-4 and Figure 4-4, that the Strouhal number, drag and lift coefficients are in agreement with the Hua *et al* [69] results.

Table 4-4 Comparison of Present Test Case with Hua *et al* [69] results

2D Cylinder, Re_D=100		3D Cylinder, Re_D=100	
Chen Hua	St = 0.165 C_L = ±0.314 C_D = 1.325±0.008	Chen Hua	St = 0.164 C_L = ±0.322 C_D = 1.327±0.009
Present Result	St = 0.164 C_L = ±0.318 C_D =1.3271±0.0085	Present Result	St = 0.16324 C_L = ±0.326 C_D =1.3263±0.009

Because of the initial problems faced in the generation of an UNCLE grid from g.f90 code, GAMBIT was used to generate the grid. There was initially a leakage in the wake region of the cylinder which allowed higher mean velocity values. However, this problem has been fixed. As the simulations that are carried out are three dimensional, include a turbulence model, and have over a million grid points, it increases the complexity of the problem and hence increases the computation time while significantly limiting the time step. Approximately, it takes about 7-8 weeks of wall time to obtain 50T non-dimensional time units with a final time step of $5x10^{-4}$. Initially, grid generated by GAMBIT was used for the 3D simulations and due to the limitations of the number of nodes (currently 3 jobs are running on about 54 nodes, 18 each) and the computational time required for these runs, the grid generated from the grid generator code was employed for the later simulations which include the simulation of the flow over the circular cylinder using a SAS hybrid turbulence model.

It has always been complicated to run the 3D simulations for the reason that the time step needs to be decreased with increasing Reynolds numbers which need a much refined grid. Typically, a 3D simulation with a Reynolds number, *Re*=140,000, where the initial conditions for the velocity field are $u = 1; v = 0; w = 0; p = 0$ and for the SA turbulence model the condition is $\tilde{\nu} = 5\nu$, and with a million grid points is estimated to take about 4-5 weeks of time to get into the real flow because of the initial instability causing it to oscillate requiring to use a much smaller time step, say $1x10^{-6}$ at the start. A code is written in Fortran90 to avoid such a situation. The code takes the output from a 2D simulation using the same conditions that we are going to use

for a 3D simulation and then the velocity field and pressure field values are interpolated on to the 3D grid and these values are used as the initial conditions for the 3D simulation. This is tested for a much coarser grid with 80X80X30 and also for the Scale Adaptive Simulation model which is implemented in UNCLE. The lift-drag plot from the simulation of the 3D circular cylinder with a grid size of 80X80X30 is presented in Figure 4-5. It can be observed from the drag curve in Figure 4-5 that initially there is noise in the flow which is on the order of 10^3. However, when the same simulation is started with better initial conditions the noise do not show up in the lift-drag curves as shown in Figure 4-6. This is an advantage when doing a 3D simulation as the time taken to overcome the initial noise is reduced and an improved set of initial conditions are used for the 3D simulations.

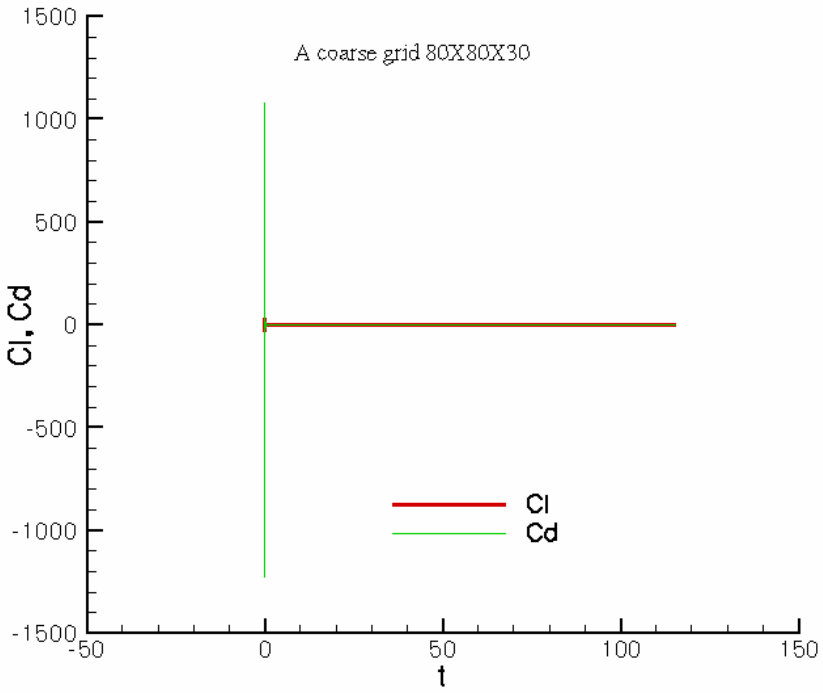

Figure 4-5 Lift-Drag plot of the 3D cylinder grid, 80X80X30

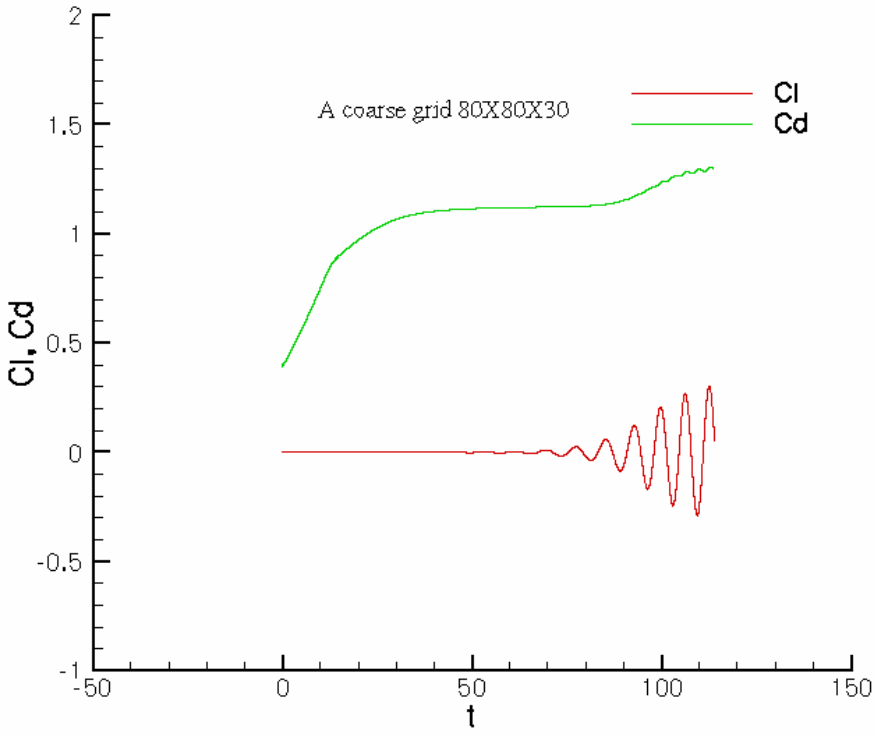

Figure 4-6 Lift-Drag plot of the 3D cylinder grid started with a better initial conditions

4.4.2 Grid Generated from GAMBIT

GAMBIT is commercial mesh generation software that comes with Fluent. Due to the above stated reasons the initial simulations use the grid generated from GAMBIT. The grid that is being used for the full-fledged problem of flow over a three dimensional circular cylinder will be discussed in this section while the details of the other grids which are used for validation and testing purpose are skipped and will be discussed along with the presentation of the results. A schematic of the grid that is currently used for the three dimensional simulations is presented in Figure 4-7.

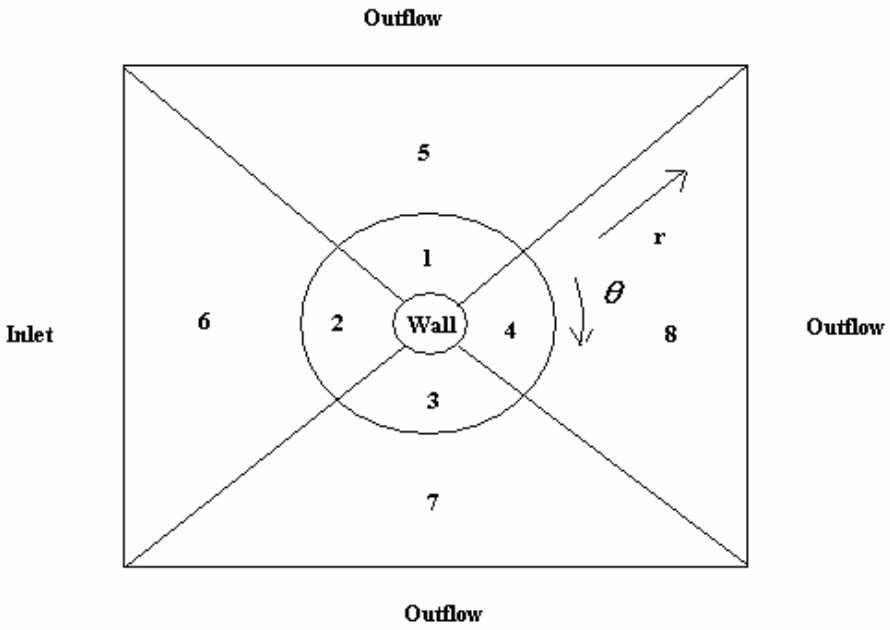

Figure 4-7 Schematic for the circular cylinder grid

The circular cylinder has a diameter of 1. It stretches out from the circular form to the square away from the wall for a cleaner specification of the boundaries. Lengthwise the grid stretches from -15.0 to 15.0 in the x-axis direction and height of the grid is also -15.0 to 15.0 in the y-axis direction. In the spanwise direction it is extended from 0.0 to 2.0. As shown in the figure, the grid is divided into 8 zones for a better meshing. The outer circle has a diameter of 3.0. The inner zones 1, 2, 3 each have 50x120 cells, 50 in the θ direction and 120 in the r direction with the stretching ratio of 0.165 in θ direction and inner zone 4 has 76x120 cells, 76 in the θ direction and 120 in the r direction with the same stretching ratio 0.165 in r direction and with uniform spacing in the θ direction and the outer zones 5, 6, 7 each have 50x40 cells, 50 in the θ direction and 40 in the r direction with the stretching ratio of 0.7 in the r direction and the outer zone 8 has 76x40 cells, 76 in the θ direction and 40 in the r direction with the same stretching ratio 0.7 in the r direction. In the θ direction the grid points are uniformly placed (equal grid spacing) whereas the grid is only stretched in the r direction. The initial grid spacing is 5.0×10^{-5} near the wall. The spanwise direction has 30 grid points with uniform spacing. The boundaries are shown in the figure except for the periodic boundary, which are applied in the spanwise directions (+Z and –Z).

Chapter 5 : RESULTS

The implemented one-equation Spalart-Allmaras turbulence model including the SA based DES hybrid turbulence model in the unstructured grid code, UNCLE, is tested on a two-dimensional flat plate, a two-dimensional circular cylinder, and a three-dimensional circular cylinder. As this thesis is mainly aimed at testing the hybrid turbulence model, DES, the focus is on the three-dimensional results. The reason for choosing a three-dimensional circular cylinder as a test case for testing the DES model is because of its simple geometry, its symmetric nature, and because it is a standard test case that is used for DES studies. The two-dimensional test cases are considered to check whether the basic form of the turbulence model was implemented properly. The results for the test cases are presented in this section.

5.1 Two-Dimensional Flat Plate

Initially, the one-equation SA model in UNCLE and GHOST codes was validated comparing the results to the well-established results of the SST model in the GHOST code on a two-dimensional flat plate. A snapshot of the grid is presented in Figure 5-1. The grid stretches from 0.0 to 5.0 in the x-axis direction and from 0.0 to 0.5 in the y-axis direction. The number of grid points in the x-axis direction is 200 with a stretching ratio of 1.05 and in the y-axis direction the number of grid points is 120 with a stretching ratio of 1.07. The boundary conditions applied for this test case are: one inlet boundary condition, two outflow boundary conditions, and one wall boundary condition. The inlet boundary condition is applied at x = 0.0 from y = 0.0 to 0.5 and the velocity is set to U = 1.0. The outflow boundary conditions applied at y = 0.5 from x = 0.0 to 5.0 and at x = 5.0 from y = 0.0 to 0.5 are $\partial u/\partial x_i = 0; \partial v/\partial x_i = 0; \partial w/\partial x_i = 0; \partial p/\partial x_i = 0$. No slip boundary condition is applied at the wall at y = 0.0 from x = 0.0 to 5.0. The Reynolds number for this validation case is Re = 2,000,000. In the case of the SA model, the transport variable of the SA turbulence model initialized with $\tilde{\nu} = 3\nu$, where ν is the molecular viscosity.

In the case of the SST model, the transport variable k is initialized with $(FSTI)^2$, where $FSTI$ is the turbulence intensity which is set to 0.1 and ω is initialized as $\rho k/(\nu FSTVIS)$, where $FSTVIS$ is the turbulence viscosity which is set to 10.0.

The stretching ratio in the y-axis direction is selected such that the y^+ value is less than 1. The definition of y^+ is

$$y^+ = \frac{yu^*}{\nu} \text{ where, } u^* = \sqrt{\frac{c_f}{2}}. \tag{5.1}$$

For flat plate boundary layers a standard correlation for turbulent flows is $c_f = \frac{0.0576}{Re_x^{-1/5}}$, where $Re_x = \frac{Ux}{\nu}$.

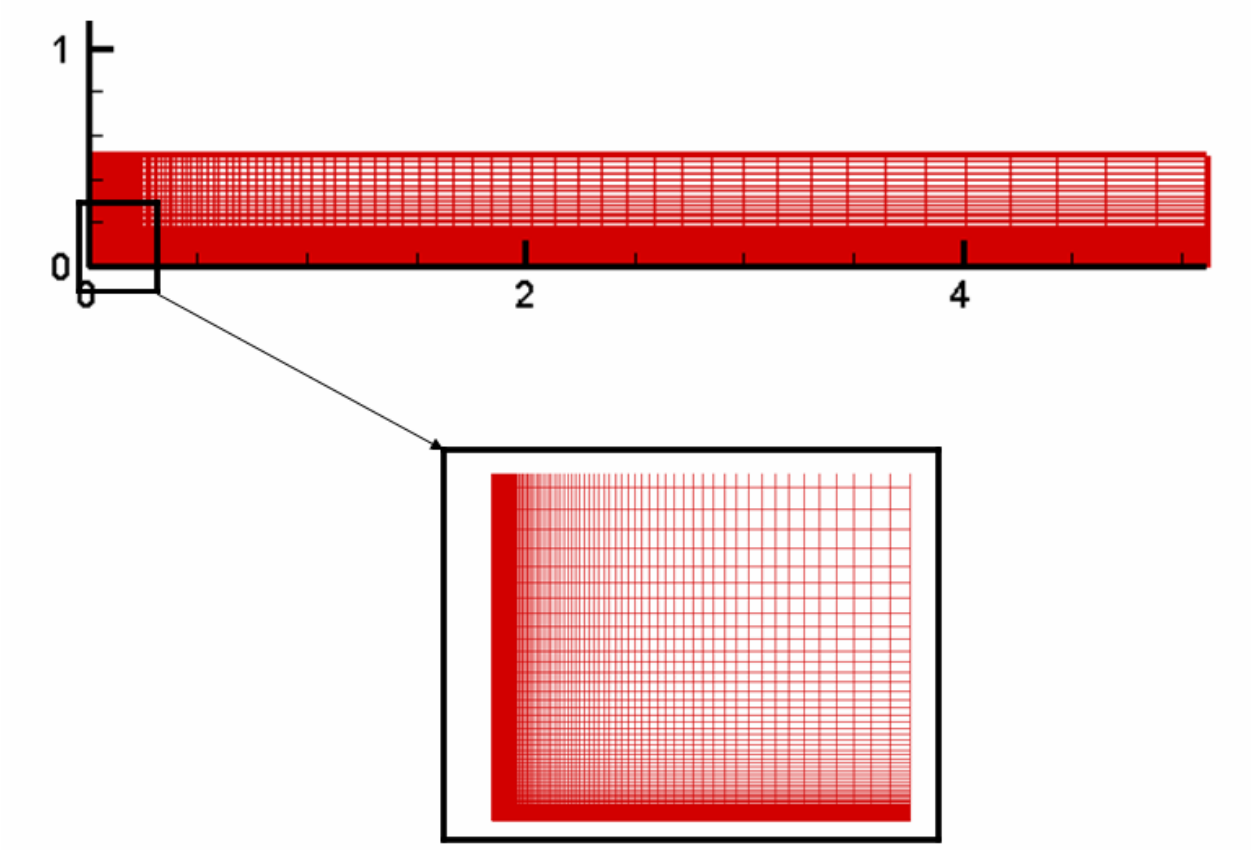

Figure 5-1 2D Flat Plate Grid

The analysis based on the skin friction coefficient plots are considered to be a useful comparison in the case of flow over a flat plate. The skin friction coefficients evaluated based on the momentum thickness values are generally regarded as a more accurate representation of the skin friction coefficient values compared to the skin friction coefficients calculated based on the *x* values. The expression is provided by Karman-Schoenherr [Hopkins and Inouye (1971)] and is given as,

$$\frac{1}{c_f} = 17.08\left(\log_{10} Re_\theta\right)^2 + 25.11 \log_{10} Re_\theta + 6.012 \text{, where } Re_\theta = \frac{U\theta}{\nu}. \qquad (5.2)$$

The momentum thickness can be calculated as $\theta = \int_0^\infty \frac{u}{U}\left(1 - \frac{u}{U}\right) dy$. (5.3)

Numerically the momentum thickness is calculated by integrating the expression, $u(1-u)$ (considering the freestream velocity *U = 1.0*), from the surface to the boundary layer thickness value for given *x* value. In the in-house codes, the c_f values are evaluated based on, $c_f = \frac{\tau_w}{\frac{1}{2}\rho U^2}$ where $\tau_w = \mu \frac{\partial u}{\partial y}$, at the cell centers based on *x* values. The skin friction plots for this case are presented in Figure 5-2. For comparison, skin friction coefficient distribution evaluated based on *x* and skin friction coefficients evaluated based on the momentum thickness, θ are presented. The plots presented are for c_f versus *x* (from the in-house codes) for both UNCLE and GHOST with SST and SA models, and for c_f versus θ for both UNCLE and GHOST with SST and SA models, and also for the theoretical values of the skin friction calculated using the standard correlation, $c_f = \frac{0.0576}{Re_x^{-1/5}}$. It should be note that in Figure 5-2 theta stands for the c_f calculated based on θ, *x* stands for c_f calculated based on *x*, and "Theoretical" curve is the theoretical values calculated using the standard correlation based on *x*. The "correlation" term in the plots represents the c_f calculated using the correlation presented in equation (5.2).

The skin friction coefficients calculated by SST models in UNCLE and GHOST based on the *x* values are well in agreement with each other and also with the c_f values evaluated using the theoretical correlation. But, the SA models in UNCLE and GHOST over predict the coefficients of skin friction based on the *x* values.

The skin friction coefficient values calculated based on θ using the correlation in equation (5.2), by the SA, SST models in UNCLE and SA, SST models in GHOST are well in agreement with each other. However, the skin friction coefficients evaluated and plotted against the momentum thickness values, θ, by the SST models in UNCLE and GHOST are little lower in magnitude when compared with the correlations curve and the coefficients of skin friction by SA models in UNCLE and GHOST are higher when compared with the correlations curve. The little jump at the end of the plate is because of the outflow boundary condition.

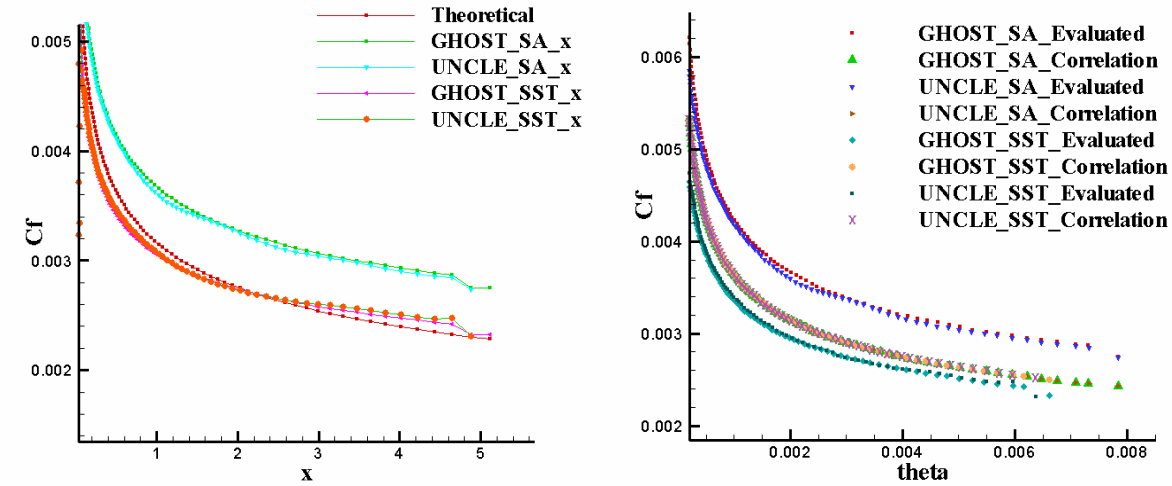

Figure 5-2 Skin Friction Plot for a 2D Flat Plate

The discrepancies in predicting the skin friction coefficient values is observed in SA models in both UNCLE and GHOST codes indicating that the implemented SA model in both the codes are consistent with each other. However, the discrepancies can be partly because of the reason that we are making a comparison between fundamentally two different models. The discrepancy means that the very near wall conditions are off but the overall boundary layer shape θ is reasonable. However, effort will be made to make the model closer to accurate in its predictions.

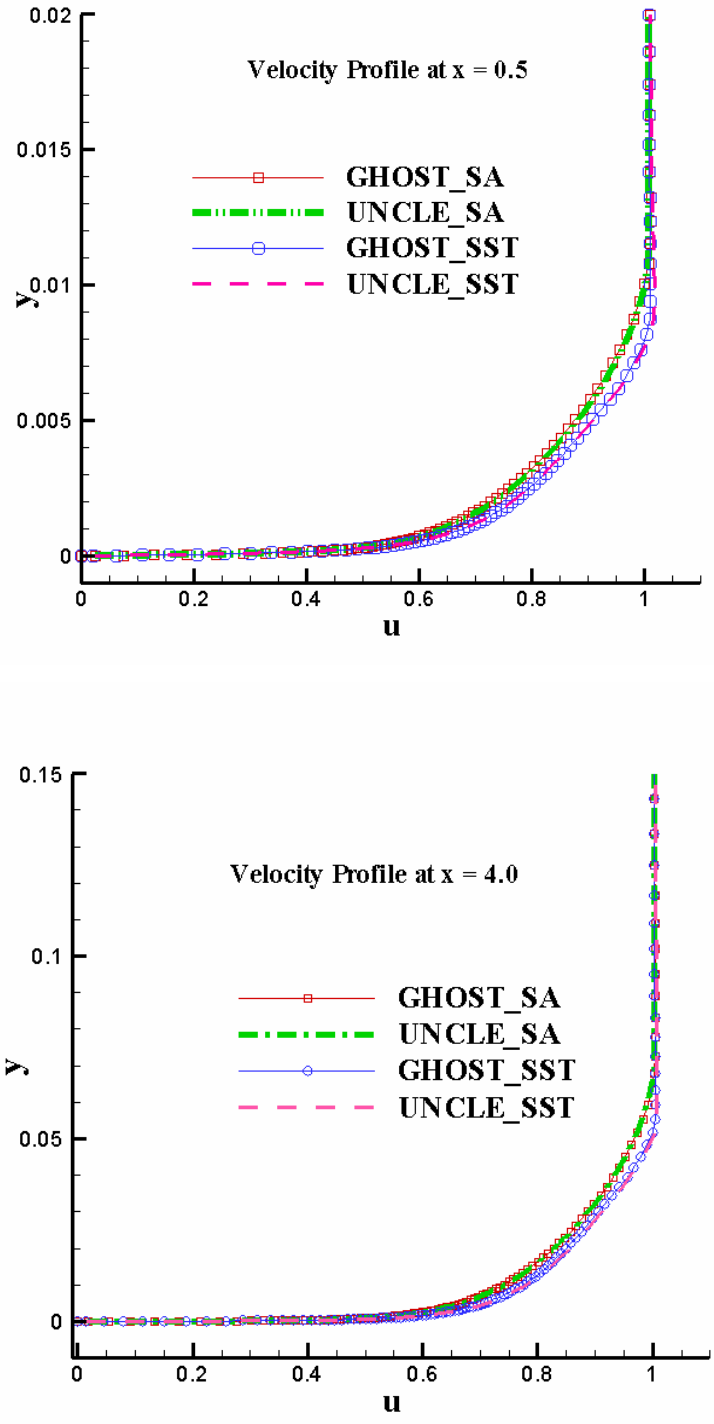

Figure 5-3 (a) Velocity Profile at *x*=0.5 and (b) Velocity Profile at *x*=4.0 for a 2D Flat Plate

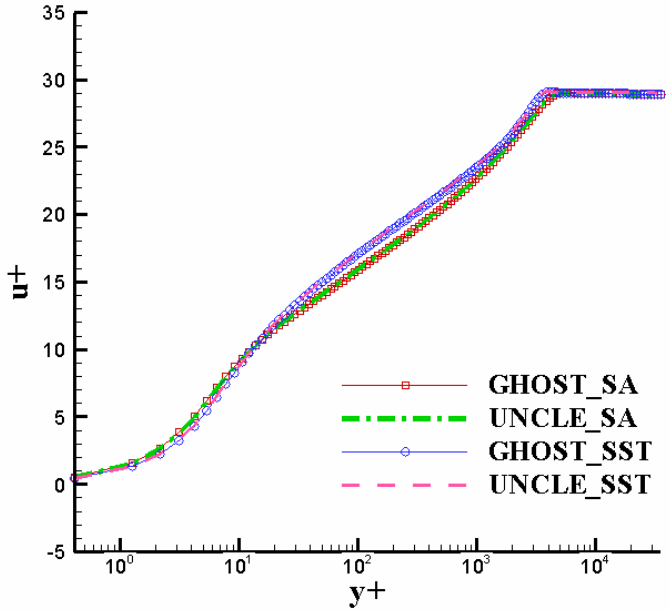

Figure 5-4 Velocity profile at *x*=4.0

The velocity profiles at x = 0.5 and x = 4.0 are presented in Figure 5-3. The reason for presenting the profiles at the beginning of the plate (x = 0.5) and nearly at the end of the plate (x = 4.0) is to observe the development of the boundary layer profile. On comparing the velocity profiles both at x = 0.5 and x = 4.0, it can be observed from the plots that the velocity predictions by SA model in UNCLE and GHOST are little higher when compared with SST model in UNCLE and GHOST, but still are in agreement with each other. The little discrepancy in the results reflects the fact that we are comparing a one-equation turbulence model with a two-equation turbulence model. Also, the velocity profile at x = 4.0 is presented on the logarithmic scale in terms of u^+ and y^+ in Figure 5-4. It can be observed in the very near wall region both the SA and SST models behave similarly, but away from the wall in the sublayer region, a little discrepancy can be found between the two models. In the logarithmic region, the SST model behaves well compared with SA model, but again in the defect or the outer layer, both the models behave similarly. Though a discrepancy in the behavior of the SA model is observed, the velocity profile indicates that the basic shape is reasonable and the model clearly indicates the boundary layer regions (sublayer, log layer, and outer layer).

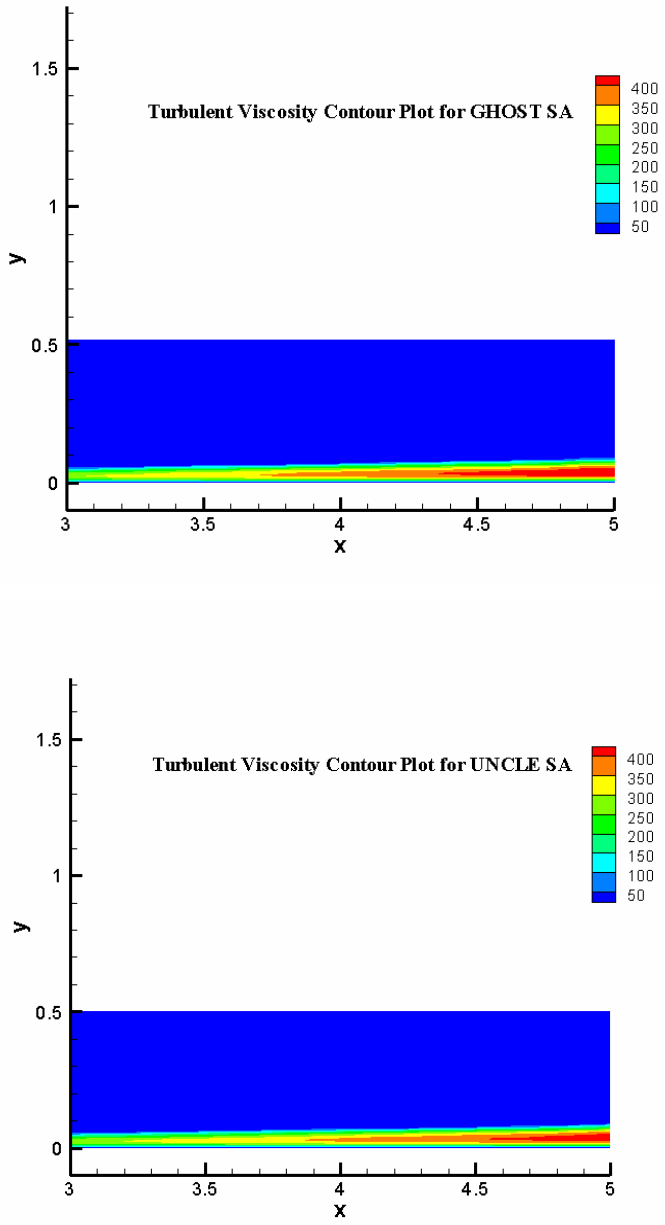

Figure 5-5 (a) Turbulent viscosity contour (SA-G) (b) Turbulent viscosity contour (SA-U)

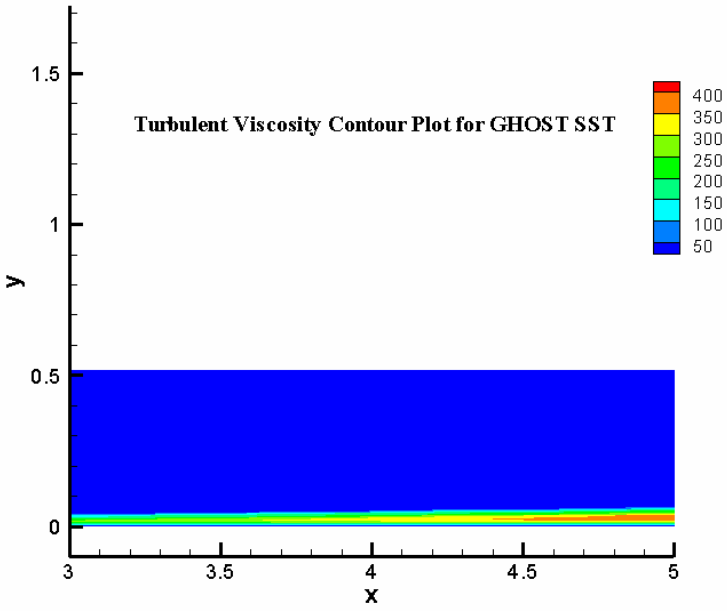

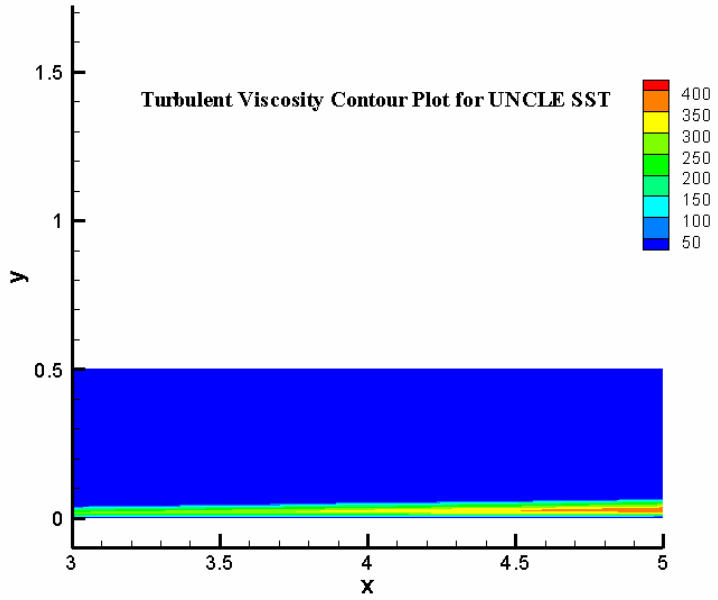

Figure 5-6 (a) Turbulent viscosity contour (SST-G) (b) Turbulent viscosity contour (SST-U)

The contour plots for the turbulent viscosity are presented in Figure 5-5 and Figure 5-6 for the SA-UNCLE, SA-GHOST, SST-UNCLE, and SST-GHOST cases. Presented contour plots of turbulent viscosity are normalized with the molecular viscosity, ν .However, for a quantitative

observation the turbulent viscosity values are extracted from the individual contour plots at x=4.0 and is presented for comparison in Figure 5-7. From the plot it can be seen that the turbulent viscosity values near the surface for the SA model in UNCLE and GHOST have a good match with the SST model in UNCLE and GHOST. However, away from the surface the SA model in UNCLE and GHOST follows the same profile but have higher values compared to the SST model in UNCLE and GHOST. The turbulent viscosity values for the SST model in GHOST and UNCLE follow the same profile.

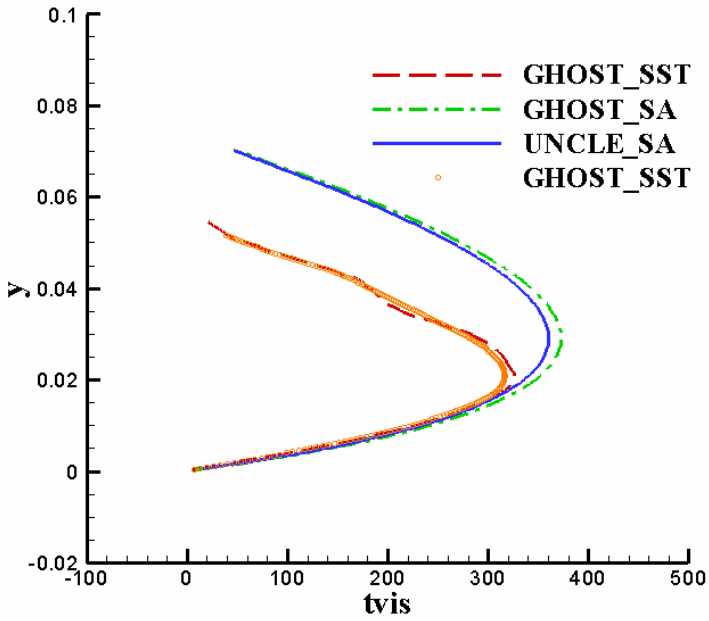

Figure 5-7 Turbulent viscosity at x=4.0 from the contour plot

With this test case the basic implementation of the SA-DES model in the UNCLE code is tested. The results look reasonable when compared with the results from the well established GHOST model. The small discrepancies in the results when both the models are compared can be due to the reason that they are different models.

5.2 Two-Dimensional Circular Cylinder

Another test case that is considered to test if the implemented SA model in the UNCLE code is working is a two-dimensional circular cylinder. The data for these simulations are present in Travin *et al* [72]. The grid contains 200 grid points in the circumferential direction and with 140 grid points in the radial direction. The grid runs from -15.0 to 15.0 in the x-axis direction and -15.0 to 15.0 in the y-axis direction, the center of the cylinder being at (0, 0). The boundary conditions for this test case are: one inlet boundary condition, three outflow boundary conditions, and one wall boundary condition. The inflow boundary is at x = -15.0 from y = -15.0 to 15.0 and the velocity is set to U = 1.0. The outflow boundary conditions are applied at the top at y = 15.0 from x= -15.0 to 15.0, at the bottom at y = -15.0 from x = -15.0 to 15.0, and at x = 15.0 from y = -15.0 to 15.0. No slip boundary condition is applied at the surface of the cylinder. The Reynolds number used for this test case is Re = 140,000. The grid for this test case is shown in Figure 5-8.

The 2D cylinder grid is used for the runs with laminar initial SA, SST, SA-DES, SST-DES models, and, turbulent initial SA, SA-DES models. The motivation for doing the simulations with two different initial conditions, laminar and turbulent, is from Travin *et al* [72]. A laminar initial flow in a SST model means the turbulence model is turned on but the turbulence intensity (FSTI) and the turbulence viscosity (FSTVIS) in the model is set to a very low value. A turbulent initial flow in a SST model means the turbulence model is turned on and the turbulence intensity in the model is set to a value of 0.01 and the turbulence viscosity is set to 10.0 which represents that the flow is started with turbulence in it. In the SST model, the transport variables k is initialized as $(FSTI)^2$ and ω is initialized with $\left(\rho k / \left(\nu FSTVIS\right)\right)$. In the case of the SA model, a laminar initial flow has a inflow boundary condition set to $\tilde{\nu} = 0$, where $\tilde{\nu}$ is the transport variable of the SA turbulence model, and in a turbulent initial flow the inflow boundary condition is set to $\tilde{\nu} = 5\nu$, where ν is the molecular viscosity. The transport variable of the SA model is initialized as $\tilde{\nu} = 5\nu$ in the domain of the 2D circular cylinder for both the laminar initial and turbulent initial flows.

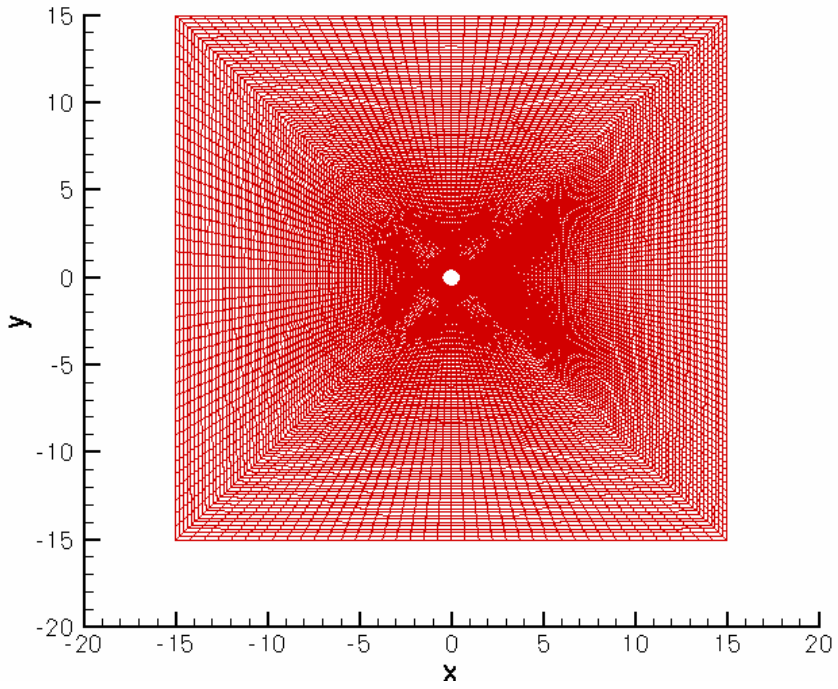

Figure 5-8 2D Circular cylinder grid

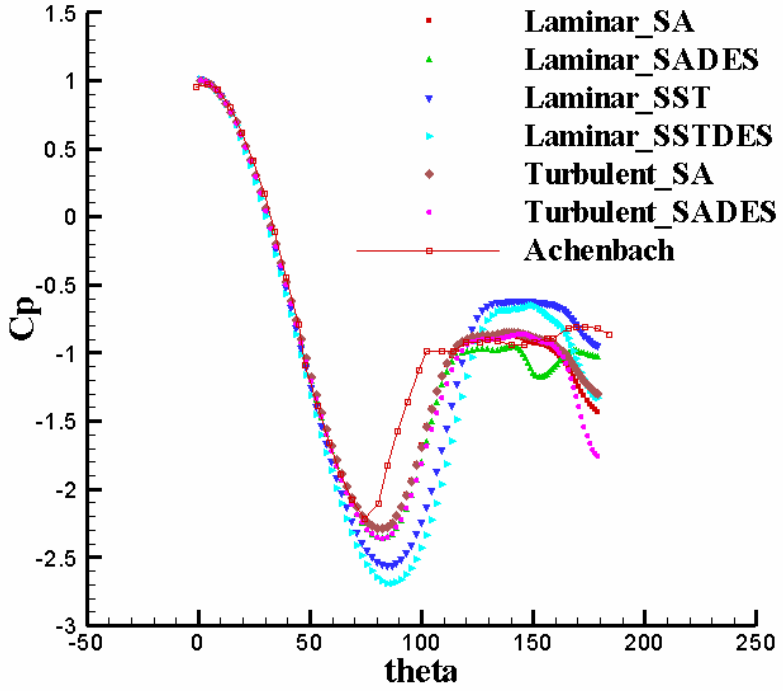

Figure 5-9 Pressure coefficient distribution at the surface of the circular cylinder

The pressure and the skin friction plots are presented in Figure 5-9 and Figure 5-10 respectively. The results of the SA and the SA-DES model from UNCLE code for both laminar initial (LSA, LSADES) and turbulent initial (TSA, TSADES) flows along with the SST (LSST) models in UNCLE code are compared with each other and with the experimental results by Achenbach [85] at a Reynolds number $Re = 2.6\text{x}10^5$. Experiments for flow over a smooth circular cylinder were performed by Achenbach [85] up to Reynolds numbers of $5\text{x}10^6$ in a wind tunnel section with the dimensions of 500 x 900 mm and with the air surrounding the cylinder. The diameter of the cylinder is 150 mm with the spanwise length of 500 mm. The pressure distribution at the surface of the cylinder for the SA and SA-DES models with laminar and turbulent initial conditions are in match with each other. However, the predictions of the pressure distribution by the SA, SA-DES models with laminar and turbulent initial conditions only agree with the results by Achenbach [85] in the $\theta \sim 0$ to 50° region, and in the recovery region. But it should be noted that the present simulation is two-dimensional and is been compared with an experiment conducted on 3D cylinder flow. The skin friction coefficient predictions by all the models were higher in magnitude compared with skin friction coefficients evaluated by Achenbach [85]. The deviation of the skin friction coefficient curve from the usual trend in case of the SST and SST-DES models compared with the skin friction coefficients by the SA and SA-DES models suggests that the SST model implementation in UNCLE needed corrections. Based on this assumption the three dimensional test cases are narrowed down to the SA model. The lift-drag plots for all the models are presented in Figure 5-11 and the corresponding values of the drag coefficients are presented in Table 5-1 along with the available results from Travin *et al* [72]. However, there was no perfect test case available in [72] to match with for these simulations but some closer matches were found to compare the results. The purpose of this particular simulation is justified by mentioning the requirement of testing the implemented model for an unsteady flow. The Strouhal number for the laminar SA and SA-DES cases are compared with the results from Travin *et al* [72] at a Reynolds number of $Re = 5\text{x}10^4$ with grid size of 210x135, using laminar SA and SA-DES models respectively, where as for the turbulent SA case the results of TS1, using turbulent initial SA model, from [72] with grid size of 118x105x30 at $Re = 140000$. The drag values for the turbulent SA and SA-DES cases are compared with results from [72] $Re = 140000$ with grid size of 150x109, using turbulent initial

SA and SA-DES models respectively, where as the laminar SA case was compared with results of LS7, using laminar initial SA model, with grid size of 118x109x30 at *Re* = 140000.

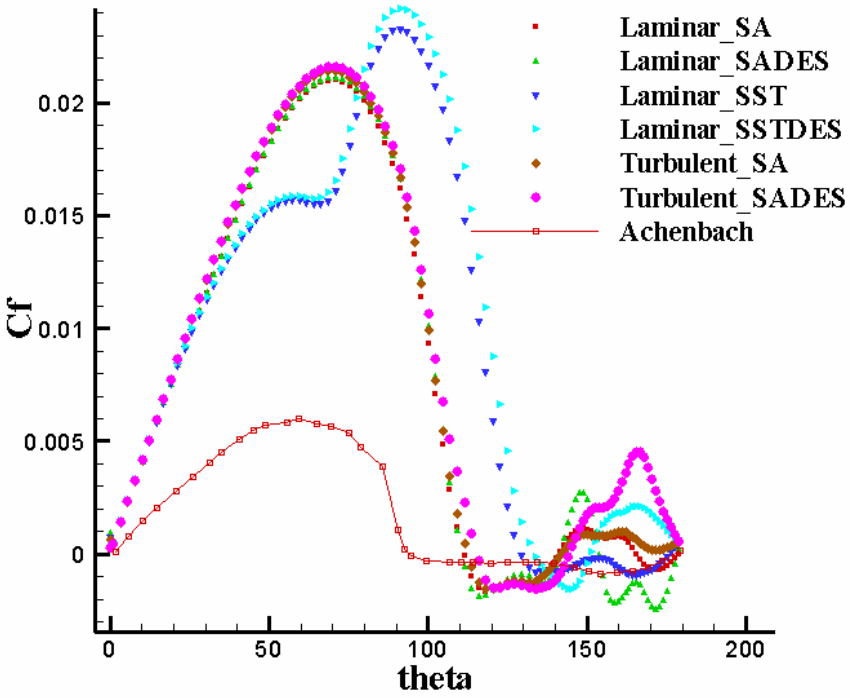

Figure 5-10 Skin friction plot of 2D circular cylinder

Table 5-1 Comparison of present 2D simulation with results in Travin *et al* [72]

Test case	Drag coeff.	Drag coeff. from present result	*St* [72]	*St* (present)
Laminar SA	0.87	0.9183	0.22	0.291
Laminar SA-DES	-	0.9929	0.2	0.302
Laminar SST	-	0.5990	-	0.347
Laminar SST-DES	-	0.6978	-	0.364
Turbulent SA	0.56	0.8825	0.3	0.293
Turbulent SA-DES	0.83	0.9603	0.3	0.304

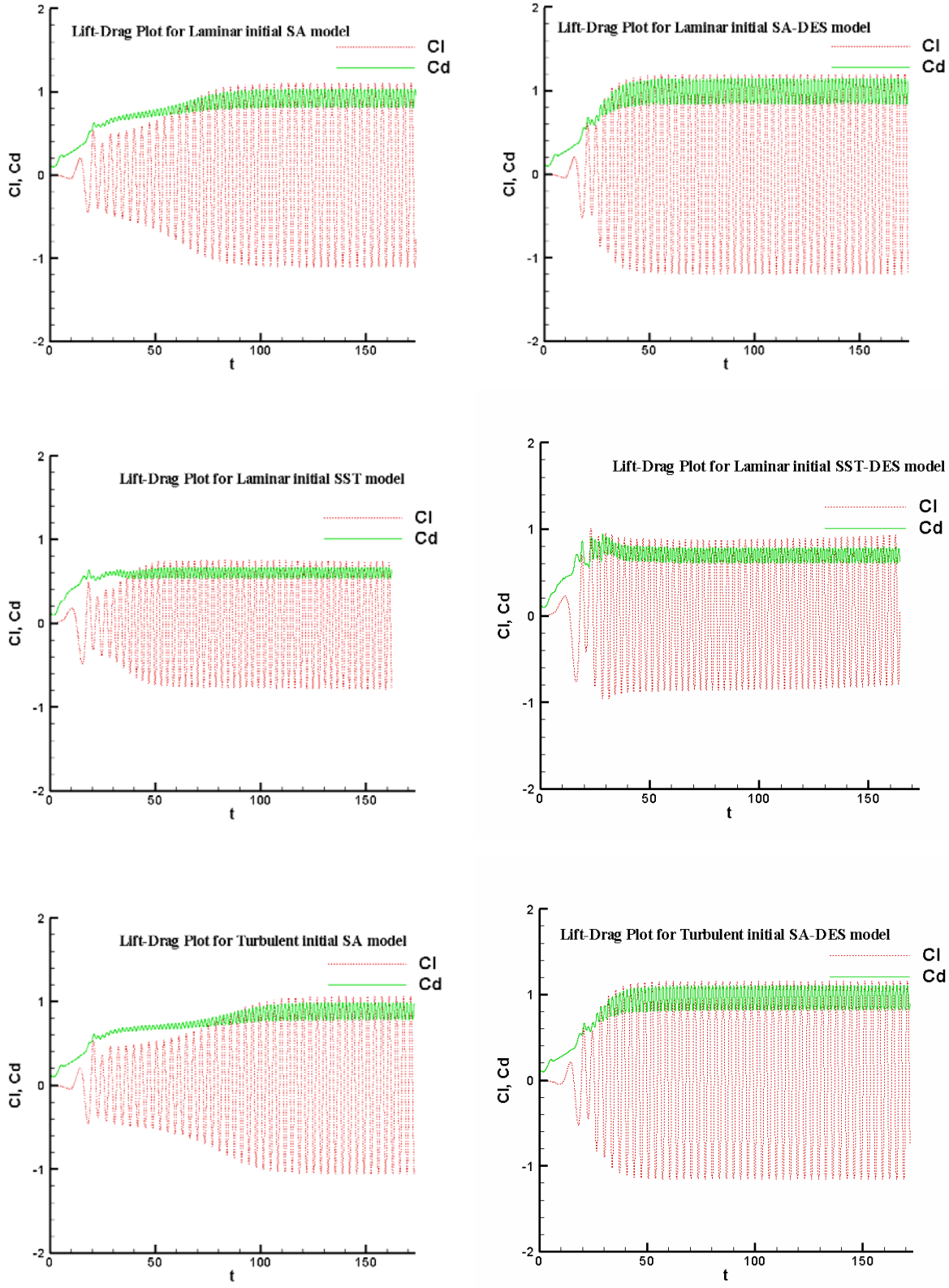

Figure 5-11 Lift-Drag plots for 2D circular cylinder at Re = 1.4 X 10^5

With this test case the basic implementation of the models in the UNCLE code have been tested for the unsteady flow. Further test cases were narrowed down to the SA based models for the reason that the skin friction coefficient distributions show significant discrepancies from the expected results in the case of the SST model. It should be noted that discrepancies were found in the earlier test case, flow over a 2D flat plate, in case of the SA model when compared with the SST model. From the present test case it is clear that there is an implementation problem with the SST model in UNCLE. However, as discussed in the earlier section efforts will be made to make the SA model closer to accurate.

5.3 Blocking Test on Two-Dimensional Circular Cylinder

When the boundaries are close to surface of the cylinder, there is a blocking issue to be considered and a correction is needed for the freestream velocity value. In order to investigate the blocking issue a two-dimensional circular cylinder with two different grids differing in the positions of the outer boundaries is considered.

Mass is conserved in the domain that defines the fluid flow by the principle of conservation of mass. When the boundaries are close and when the flow reaches the top of the cylinder there is a reduction in the cross-sectional area, so in order to maintain the mass conservation principle the freestream velocity is increased to compensate for the change in area. The output tools in the code usually consider the freestream velocity to be 1.0 and there arises a need for correction to the output plots that consider the freestream velocity for the calculations. However when the boundaries are far the reduction in area is relatively small and the correction needed is negligible.

To demonstrate these issues two grids are considered, one with the outer boundary placed at a distance of 15R and other one with the outer boundary placed at a distance of 30R. The grids are presented in Figure 5-12 and Figure 5-13. The boundary conditions of this test case are same as that of the previous 2D circular cylinder and also the initial conditions for the SA and the SA-DES case are same as in the previous test case, with turbulent initial conditions. This test case is run at the Reynolds number of $Re = 3900$.

The grid with outer boundary placed at 15R square has 226 grid points in the circumferential direction and all the grid points are uniformly spaced. It has 160 grid points in the radial direction. Whereas, the grid with outer boundary placed at 30R square has 226 grid points in the circumferential direction with all the grid points uniformly spaced and 190 grid points in the radial direction. The initial grid spacing for both the grids is $5x10^{-5}$.

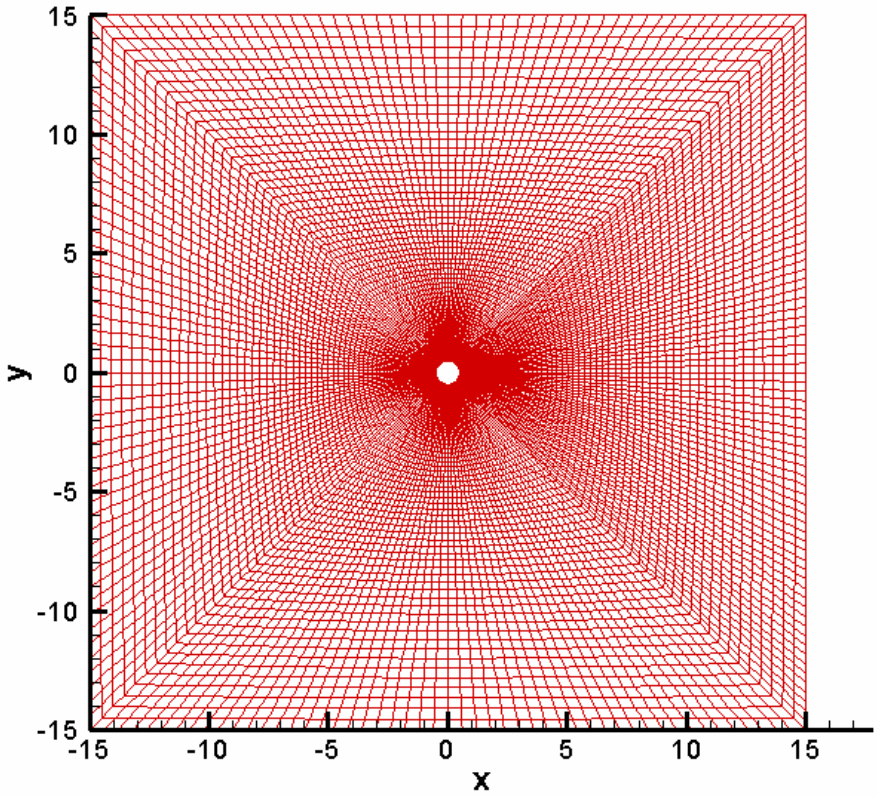

Figure 5-12 2D Grid of a Circular Cylinder with 15R square

The pressure plot and the coefficient of skin friction plot are presented in Figure 5-14. There is a notable increase in the values of the coefficient of pressure for the grid in the 15R square case when compared with the grid in the 30R square case. Results for both the SA and the SA-DES models are presented for comparison. There is a quantitative difference in the predictions of the SA model and the SA-DES models which can be observed from the pressure plot. The centerline velocity plot, defined as velocity in the streamwise direction at $y = 0$ in the

wake region, is presented in Figure 5-15. It can be observed from the centerline plot that the velocity profile near the surface in the wake region does not vary with change in position of the outer boundaries, but away from the surface of the cylinder the velocity profile differs quantitatively with the change in position of the outer boundaries for both the SA and the SA-DES models. In order to show the flow behavior in the wake region, the vorticity plots are presented in Figure 5-16 and Figure 5-17. The lift-drag plots are presented in Figure 5-18 and Figure 5-19. The lift and drag coefficients along with the Strouhal number are presented in Table 5-2. From these values it can be observed that there is a measurable change in the lift and drag coefficients including the Strouhal number when 15R square case is compared with the 30R square case.

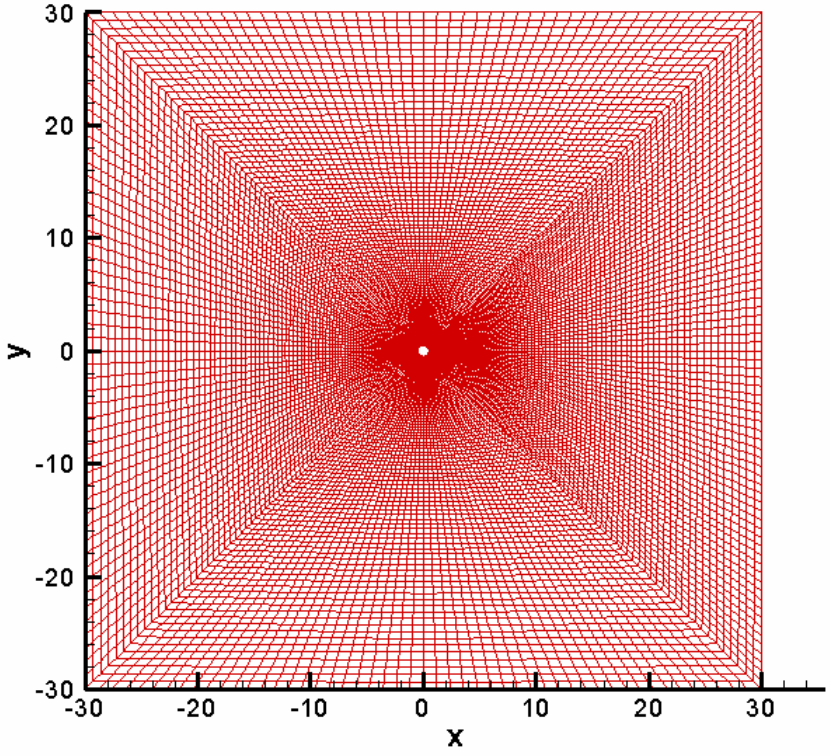

Figure 5-13 2D Grid of a Circular Cylinder with 30R square

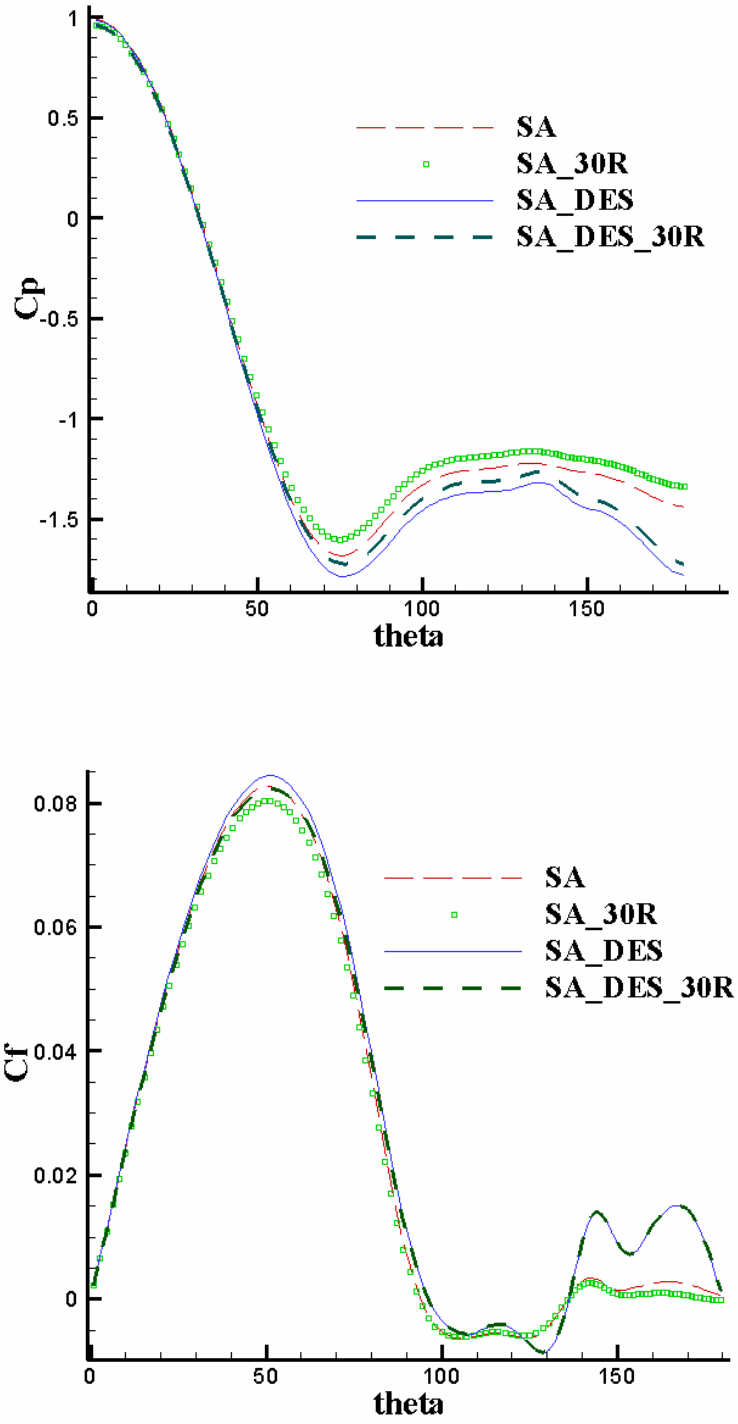

Figure 5-14 (a) Pressure and (b) Skin friction coefficient distributions for blocking comparison

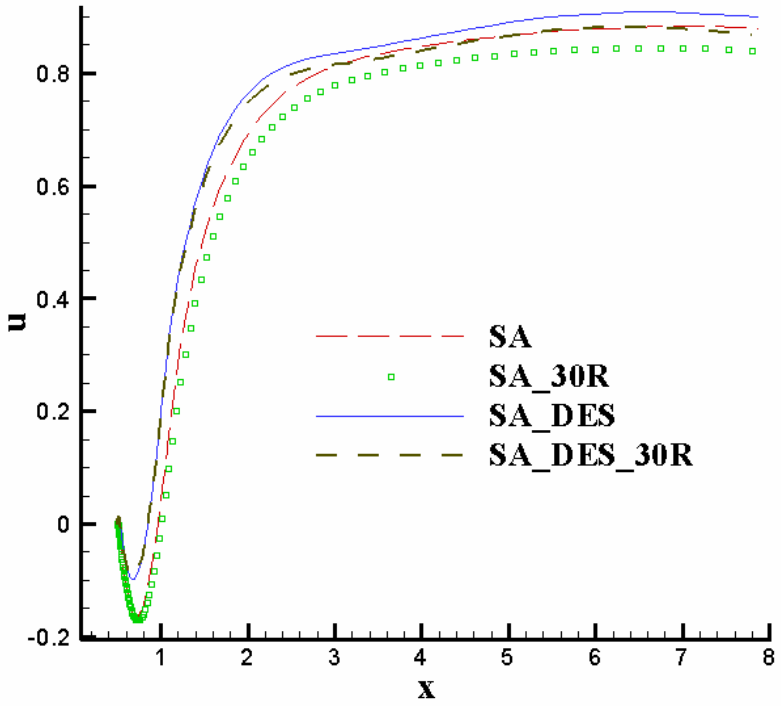

Figure 5-15 Centerline Velocity Plot for blocking comparison

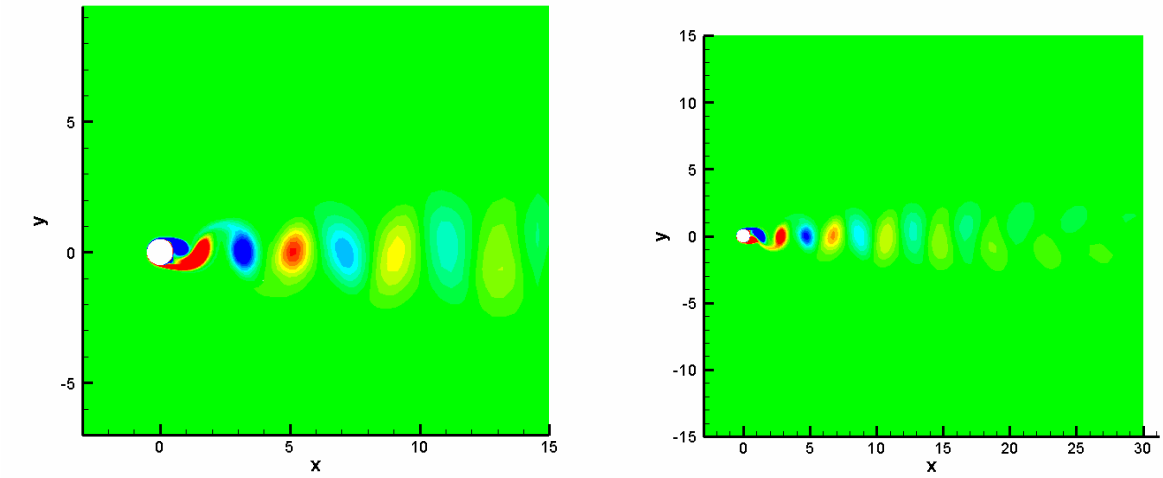

Figure 5-16 Vorticity plot for (a) SA model and (b) SA model with the grid of 30R

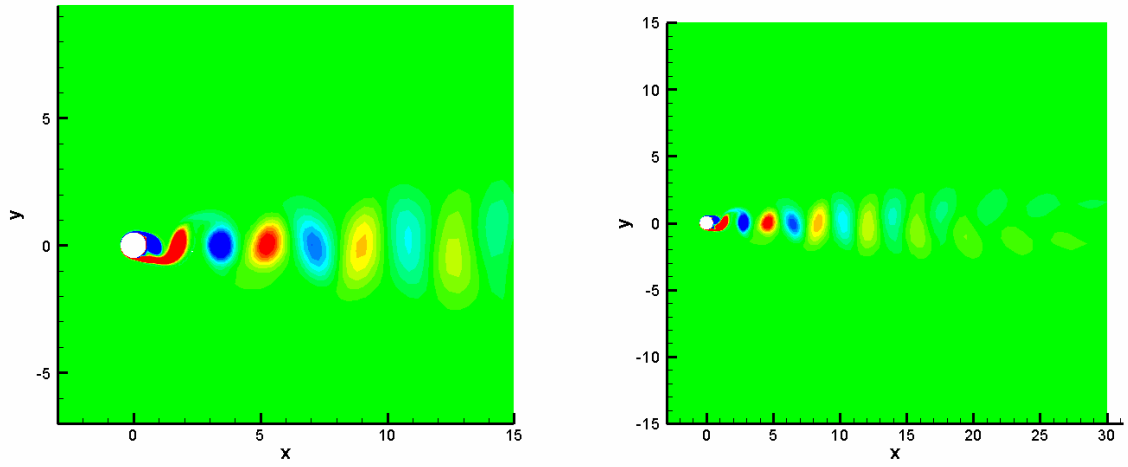

Figure 5-17 Vorticity plot for (a) SA-DES model and (b) SA-DES model with the grid of 30R

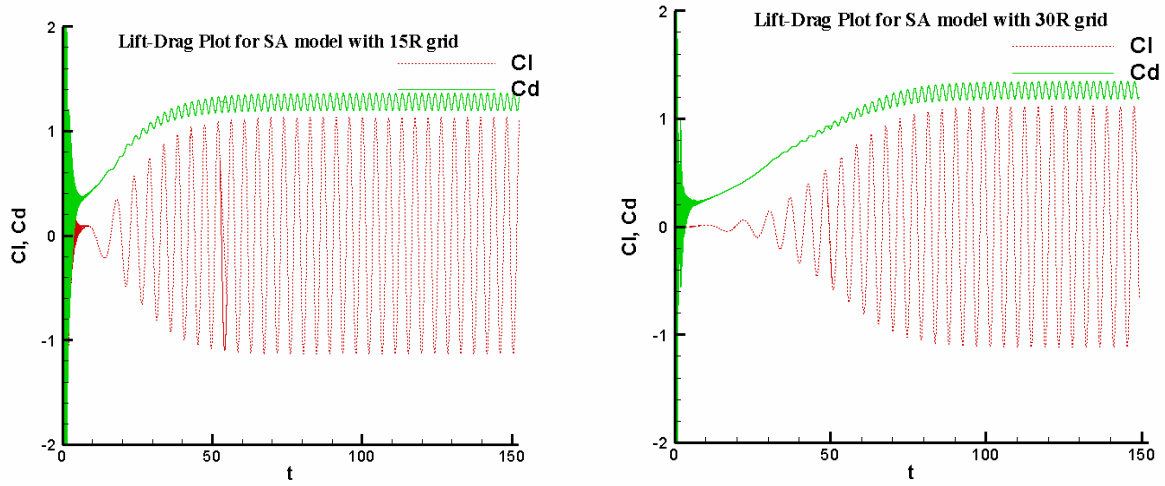

Figure 5-18 Lift-Drag plots for (a) SA model and (b) SA model with the grid of 30R

Table 5-2 Lift-Drag coefficients and Strouhal number for 2D circular cylinder

	C_L	C_D	Strouhal number
SA model with R15	±1.133	1.278 ± 0.081	0.229
SA model with R30	±1.114	1.260 ± 0.079	0.227
SA-DES model with R15	±1.368	1.433 ± 0.164	0.244
SA-DES model with R30	±1.347	1.416 ± 0.162	0.242

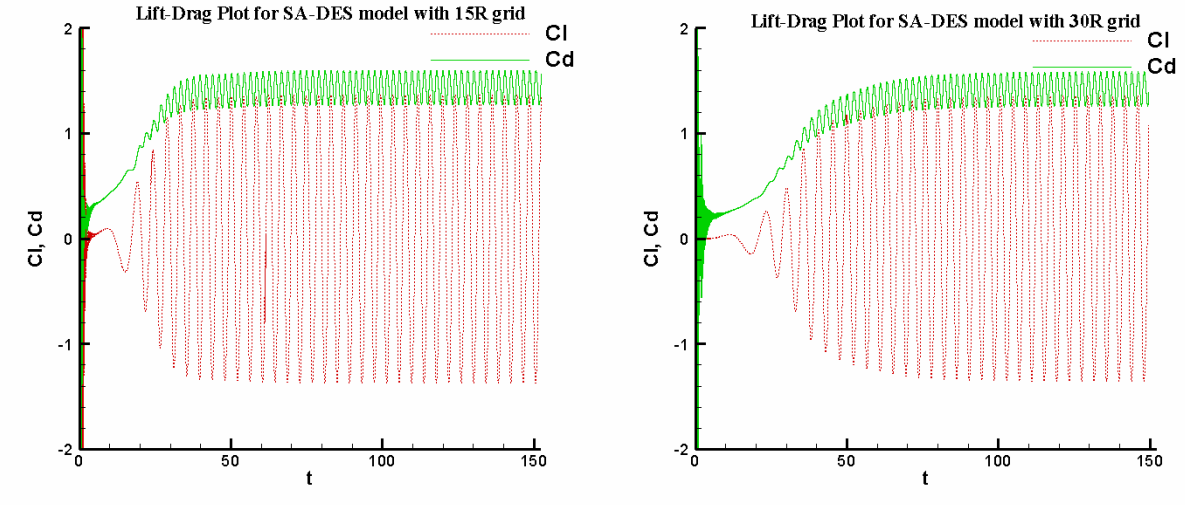

Figure 5-19 Lift-Drag plots for (a) SA-DES model and (b) SA-DES model with the grid of 30R

With this test case, the blocking effects have been shown and the differences in the pressure distribution at the surface with the change in location of boundaries from the surface are demonstrated. A correction for blocking will be discussed when looking at the 3D results.

5.4 Three-Dimensional Circular Cylinder

5.4.1 SA-DES case in UNCLE with Re = 1.4×10^5

Initially a coarser grid is employed to carry out a full fledged three dimensional test case for flow over a circular cylinder. A three dimensional circular cylinder is used as the test case for the validation of SA based DES hybrid turbulence model. An initial grid with 660,000 grid points has been used with 200 grid points spaced uniformly in the circumferential direction, 110 in the radial direction, and 30 in the spanwise direction spaced uniformly. The radius r/D = 0.5 is used for the validation purpose to compare with the available results with the same radius. A snap shot of the grid in the XY plane is presented in Figure 5-20. It is an unstructured grid and hexahedral cells are used. The grid runs from -15.0 to +15.0 in the x and y directions and 0.0 to

+2.0 in the z-direction. The boundary conditions applied for this case are: one inlet boundary condition, three outflow boundary conditions, one wall boundary condition, and a periodic boundary condition. Periodicity is applied for the first grid plane and the last grid plane in the spanwise direction. No slip conditions are applied to the surface of the cylinder and the inlet velocity is set to U = 1.0. For convenience the grid is extended to a square on the outside boundaries to make the application of the boundary conditions easier. Results from the paper of Travin *et al* [72] and the referenced experiments within that paper are considered for the validation. The grid construction and the initial conditions are replicated from the Travin *et al* [72] definitions. The tripless version of the SA model is used with the implementation of the DES model in it and $\tilde{\nu}$ is initiated to 5 times the molecular viscosity for this case.

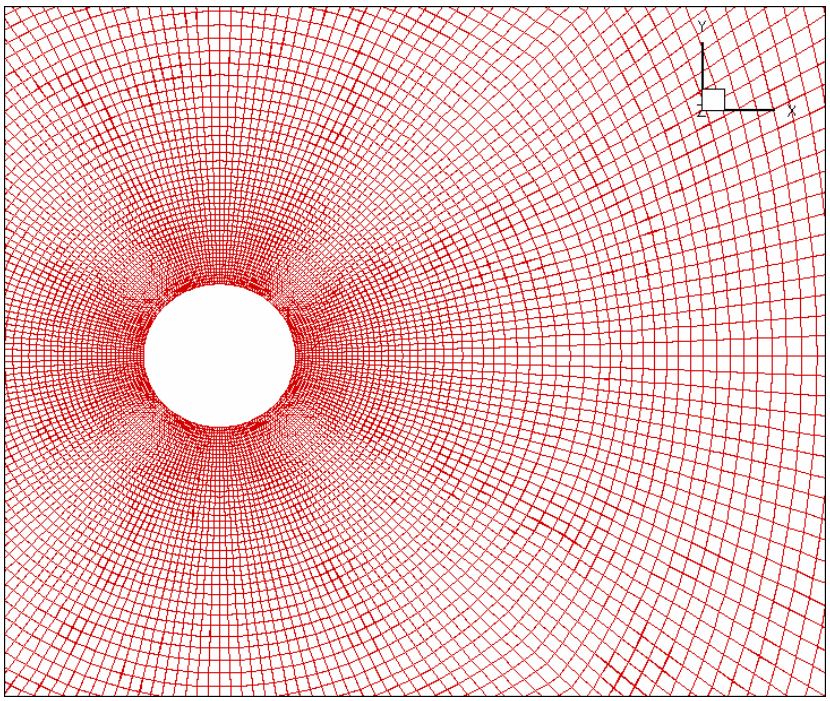

Figure 5-20 A snapshot of 3D Circular Cylinder Grid for Re = 1.4 X 10^5

Figure 5-21 shows the pressure coefficient and the skin friction coefficient plots averaged over time and space from the model at a Reynolds number of 140,000. The pressure distribution is compared with the experimental results from van Nunen [84], at a Reynolds number Re = 7.6x10^6, Roshko [83], at a Reynolds number of Re = 8.5x10^6, and Achenbach [85], at a Reynolds number of Re = 2.6x10^5, and the simulations by Travin *et al* [72] at a Reynolds number of Re =

140,000. The experimental results from van Nunen [84] are referred from Travin *et al* [72]. Experiments on the flow over a circular cylinder at high Reynolds number ranging from 10^6 to 10^7 were conducted in a wind tunnel section by Roshko [83] which can be pressurized to 4 atm. The diameter of the cylinder is 18 in. with a spanwise length of 8.5 ft and the height and width of the domain are 8.5 ft and 11 ft. The experimental details of Achenbach [85] are discussed in the earlier section in the 2D cylinder test case. The comparison of the present results with the experiments with higher Reynolds number is justified by mentioning that the motivation for this test case was from Travin *et al* [72] and in his paper the comparisons were made with the experimental results by van Nunen [84] and Roshko [83]. The computations of the coefficient of pressure are in good agreement with the experimental results from Roshko [83]. The minimum value of the pressure coefficient occurs at $\theta = 76°$, the flow separates at $\theta = 113°$, and the recovery is after $\theta = 115°$. Also, the pressure distribution in the present simulation is in good agreement with the results by Achenbach [85] and does a better job when compared with others. Even though the magnitude of the minimum pressure value is over predicted in the present simulation, it does a better job compared with others. And, the lower values in the wake region compared with the results by Travin *et al* [72] may be due to differences in the grid construction. Coming to the skin friction coefficient curve, the values were compared with the results with the experimental results by Achenbach [85], at a Reynolds number of $Re = 3.6\text{x}10^6$, and $Re = 2.6\text{x}10^5$, and with the CFD simulation by Travin *et al* [72]. The results have a better match with the skin friction coefficients obtained by Achenbach [85] at $Re = 3.6\text{x}10^6$ than with Travin *et al* [72]. When compared with the results by Achenbach [85] at $Re = 2.6\text{x}10^5$, present simulation under predicts the skin friction coefficient values, but does a better job compared with Travin *et al* [72]. The wavy pattern in the wake region is likely a grid refinement issue again which is to be rectified in the next simulation by adding more number of grid points. Longer integration periods may also be necessary for obtaining average values (the integration has covered over 150 non-dimensional ($t = D/U$) time units, but the average has only been taken over the last eight oscillation cycles).

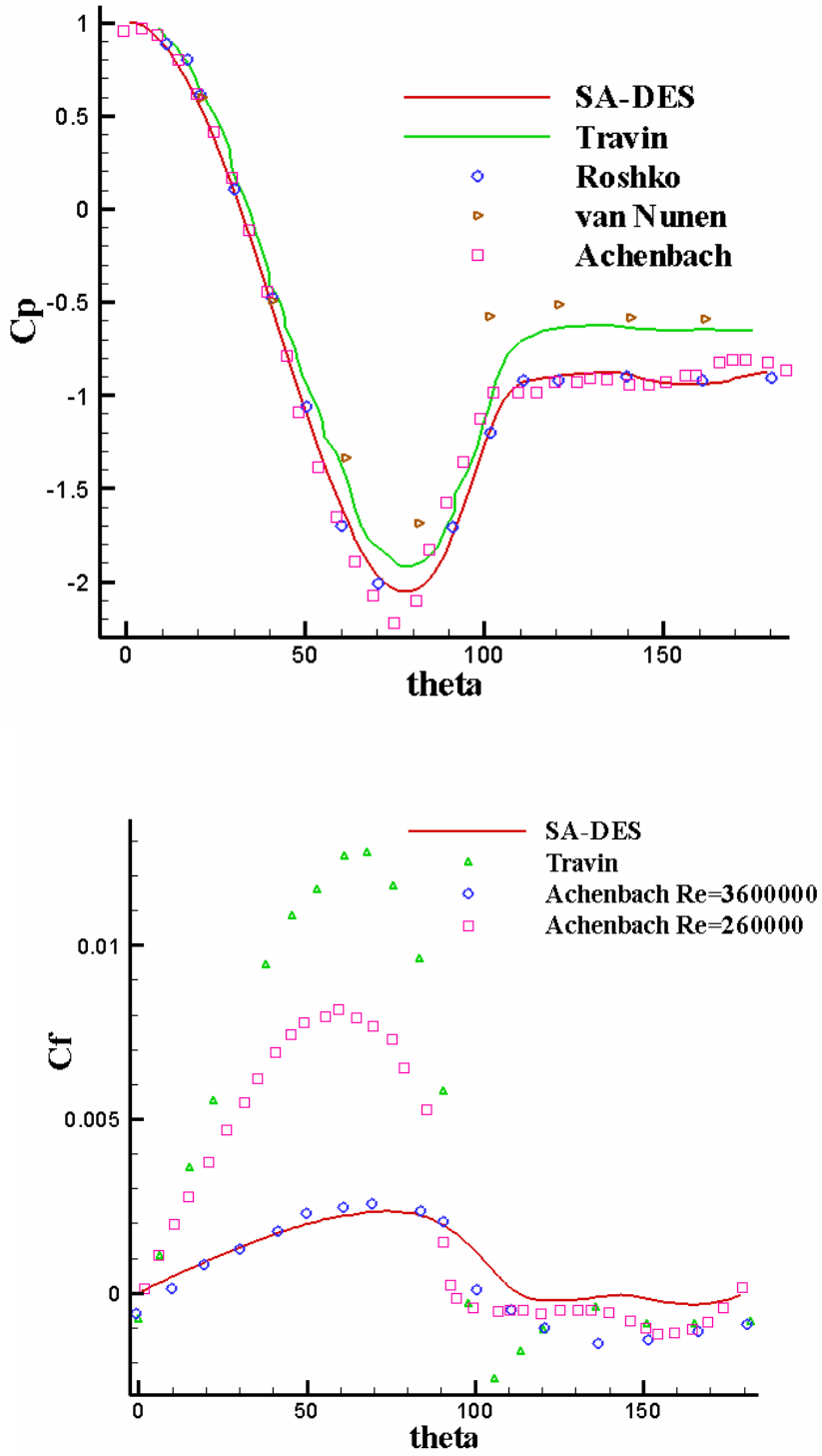

Figure 5-21 (a) Pressure plot and (b) Skin friction plot of 3D cylinder at Re = 1.4 X 10^5

The lift-drag plot along with the vorticity plot is presented in Figure 5-22 and the centerline velocity plot averaged in time and space is presented in Figure 5-23. The average drag coefficient as in Travin *et al* [72] for Re = 1.4×10^5 is 0.57 with a Strouhal number of 0.3 and the presented results has a drag coefficient of 0.76 with a Strouhal number of 0.275 in Figure 5-22(a). The drag value is higher and the Strouhal number is lower compared to Travin *et al* [72]. This again can be due to the grid resolution issues. Also, it can be observed that the vorticity plot do not contain the turbulent structures indicating that the grid is to be refined in the wake region. In the centerline velocity plot, current result is compared to the simulation of Travin *et al* [72] and to the experimental results by Cantwell and Coles [86]. Experiments on flow over 3D cylinder are conducted in a wind tunnel section by Cantwell and Coles [86] for Reynolds number *Re* = 140000. The wind tunnel has the height of 10 ft and width of 304.8 cm, and the cylinder has a diameter of 10.14 cm and is 2.97 m long. By observing the velocity curve, the occurrence of minimum value of the velocity is at $x = 0.34$ and the minimum in case of experimental value also occurs at $x = 0.34$. And the recovery of the velocity after the occurrence of the minimum value is after $x = 0.34$ in agreement with the experimental results, but differs in the magnitude of velocity. However, in the result from Travin *et al* [72] the raising curve is observed only after $x = 1.0$. Even though an exact match cannot be found, qualitatively the velocity profile has the basic shape of a centerline velocity curve. In order to get more accurate result a longer averaging over the time intervals also a finer grid is needed.

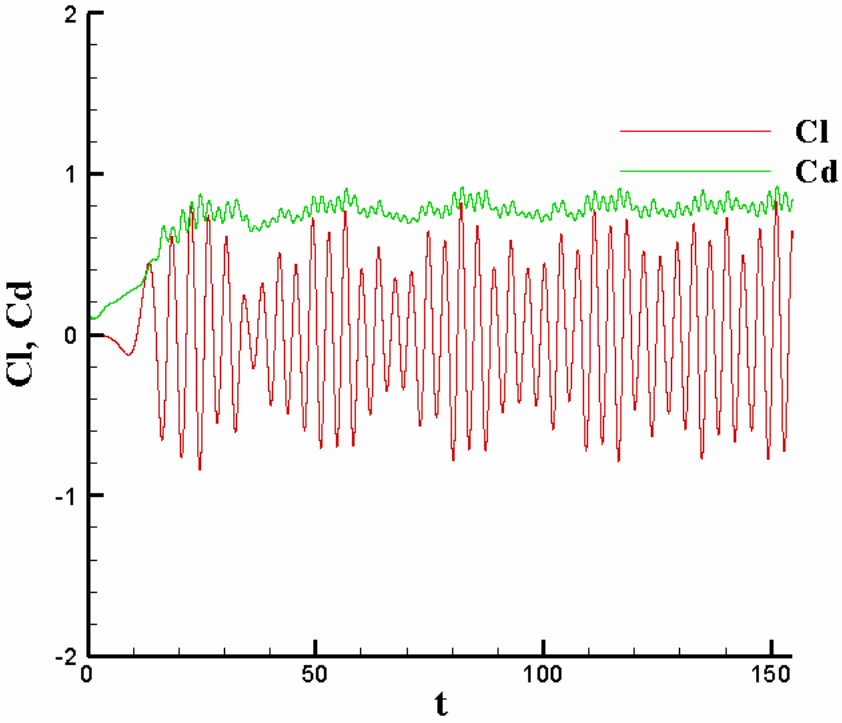

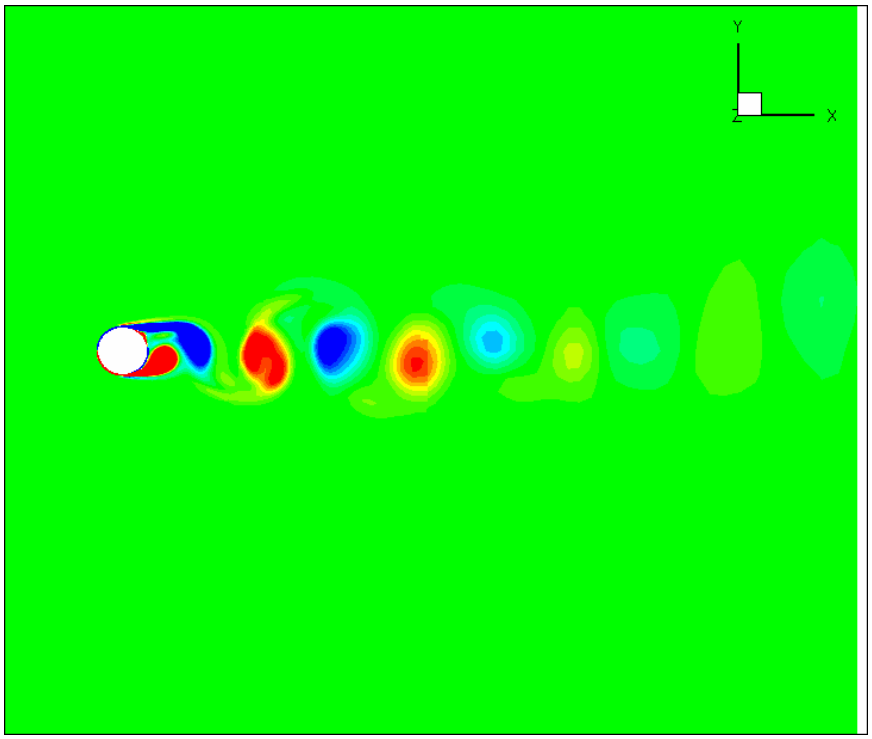

Figure 5-22 (a) Lift-Drag plot and (b) Vorticity plot at Re = 1.4 X 10^5

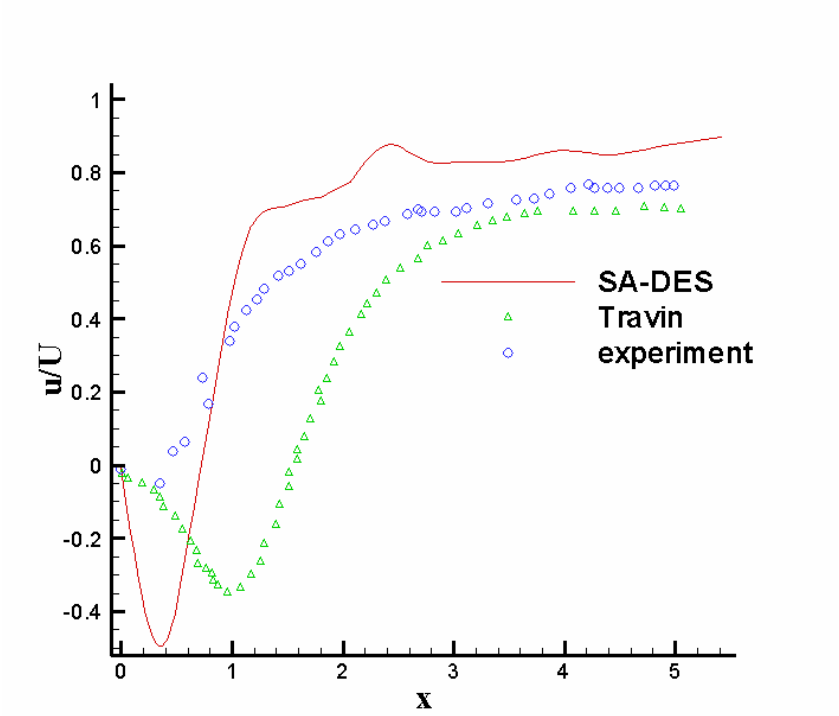

Figure 5-23 Centerline velocity plot of 3D cylinder at *Re* = 1.4 x 10^5

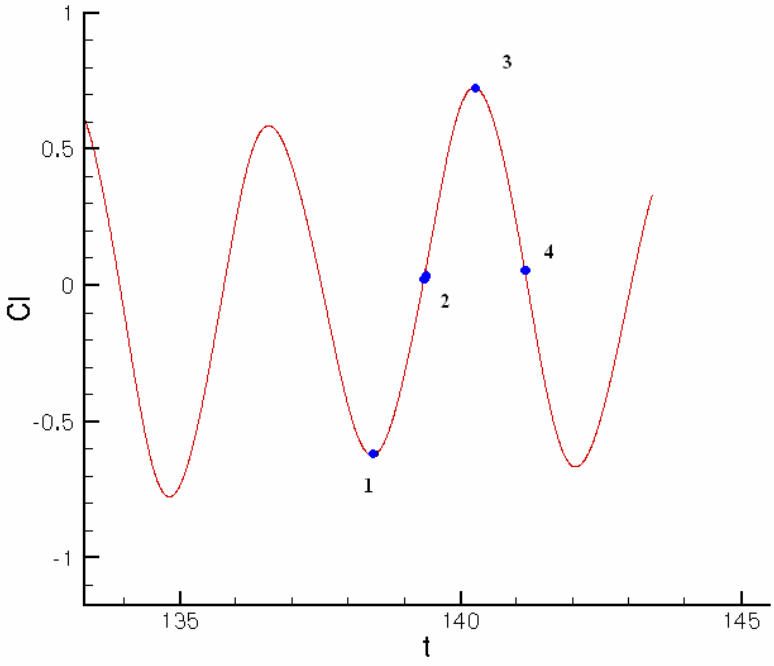

Figure 5-24 Lift oscillation at *Re* = 1.4 X 10^5

Four points were picked in the lift oscillation as shown in Figure 5-24 to observe the velocity distribution in the wake region in the streamwise and cross-flow directions. The velocity profiles were averaged in the z-direction and the mean of these profiles is taken over the four points on the lift oscillation mentioned above. Three different points are picked up in the wake region, $x = 1.06$, $x = 1.54$, and $x = 2.04$ to observe the velocity distributions. The velocity profiles are presented in Figure 5-25 at three different locations presented on the same plot. The minimum values of the velocities in streamwise direction at three different locations $x = 1.06$, $x = 1.54$, and $x = 2.04$ are -1.05, -0.47, and -0.308 respectively. The magnitude of the velocities at the higher end of the oscillation in the velocity distribution in the cross-flow direction at $x = 1.06$, $x = 1.54$, and $x = 2.04$ are 0.34, 0.196, and 0.12 respectively. The magnitude of the velocities at the lower end of the oscillation at $x = 1.06$, $x = 1.54$, and $x = 2.04$ are -0.409, -0.17, and -0.071. It can be observed that the velocity profiles smooth as the flow moves away from the surface of the cylinder.

Instantaneous contour plots for the streamwise, cross-flow, and spanwise velocities are presented in Figure 5-26 along with the contour interval values in Table 5-3. These contours are in the YZ plane and are in the wake region. The reason for presenting these contours is to show the velocity field in the wake region. Also, the instantaneous contour plot of $\overline{w'^2}$ with contour intervals of 0.002 is presented in Figure 5-27. This plot shows the three dimensionality of the flow and confirm that the simulation carried out is essentially three dimensional. Instantaneous plot of the iso-surfaces of vorticity magnitude is presented in Figure 5-28. The vortex structures in the wake region can be observed from this plot.

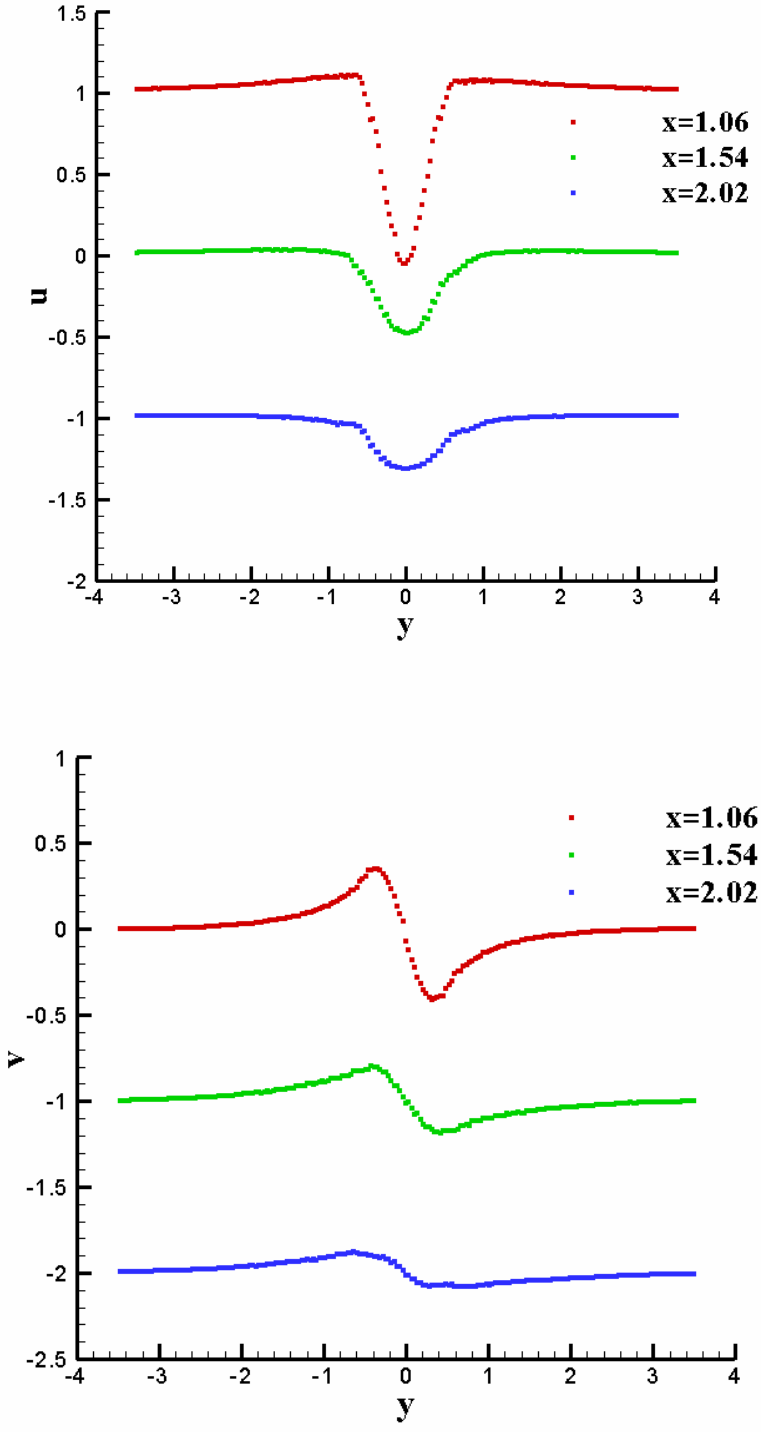

Figure 5-25 Velocity profiles in (a) Streamwise and (b) Cross-flow directions

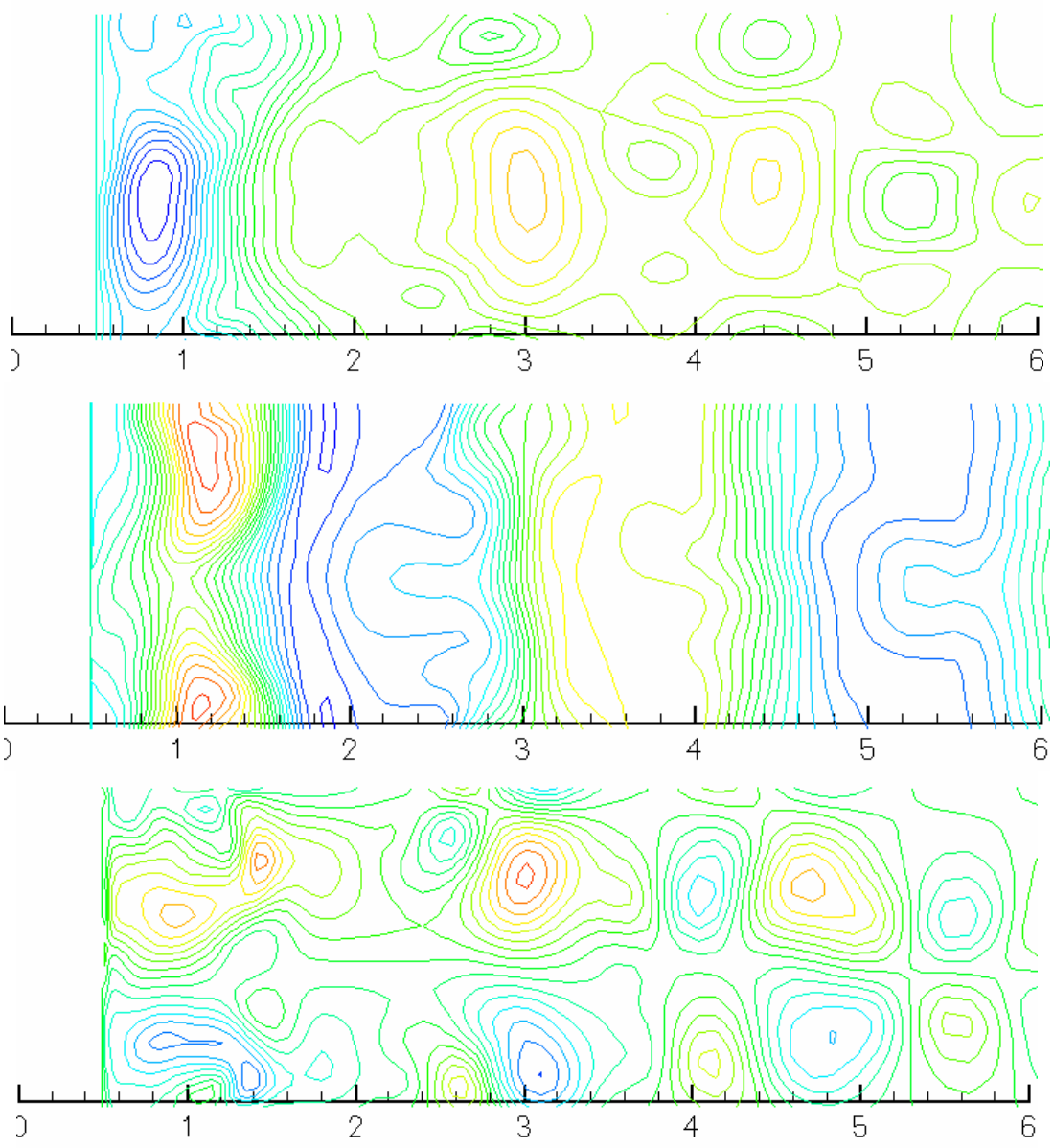

Figure 5-26 Contour plots for (a) Streamwise (top) (b) Cross-flow (middle) and (c) Spanwise velocities (bottom)

Table 5-3 Contour intervals for the streamwise, cross-flow, and spanwise velocity contour plots

	Contour intervals
u	0.04
v	0.095
w	0.18

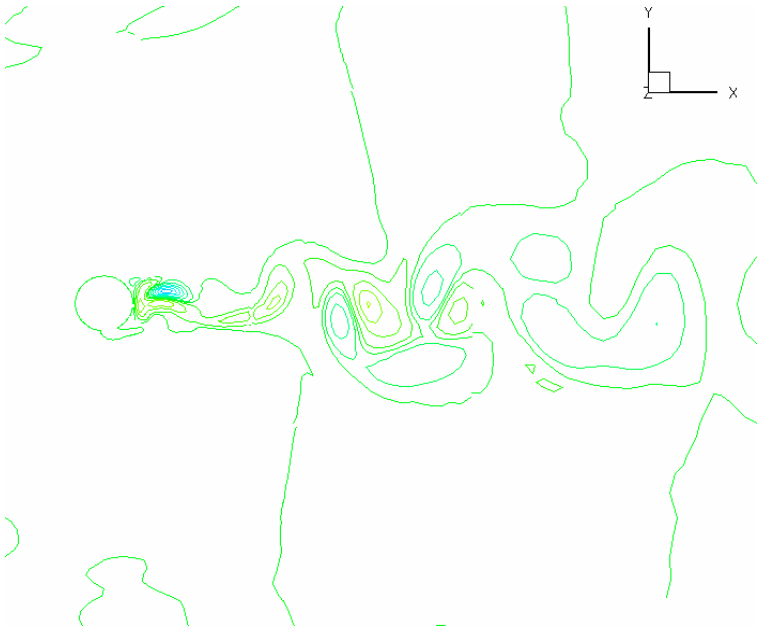

Figure 5-27 Contours of $\overline{w'^2}$

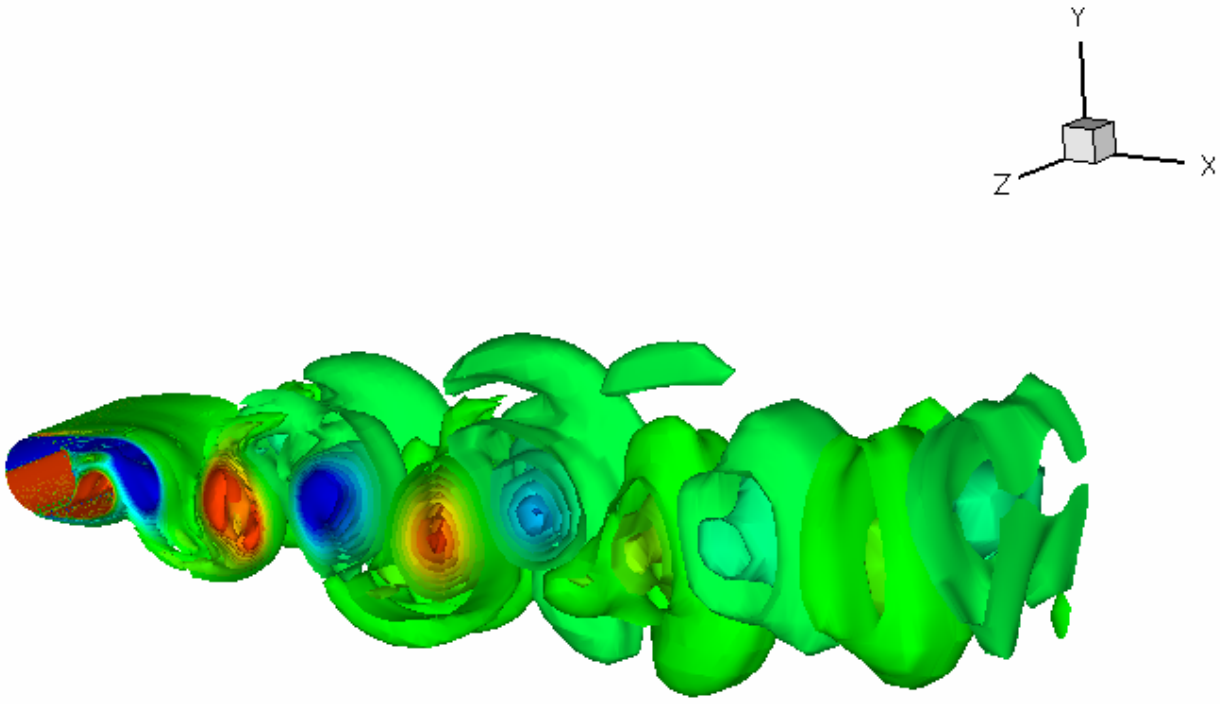

Figure 5-28 Iso-surfaces of vorticity magnitude

This test case is the first three-dimensional simulation that is run using the SA-DES model. As this is the initial simulations, in order to test the full functioning of the SA-DES case a

coarser grid was used. Some of the discrepancies in the results may be partially due to the coarser grid.

5.4.2 SA-DES case in UNCLE with Re = 3900

The test case here uses a different grid than the earlier case in the wake region with the Reynolds number $Re = 1.4 \times 10^5$. The grid used here is more refined in the wake region. The profile of the grid clearly is not changed as discussed in the earlier chapter in the GAMBIT grid generation section; however, the grid composition is changed which will be discussed here in detail. A snapshot of the grid is presented in Figure 5-29. The grid has 225 grid points in the circumferential direction with 75 grid points in the wake region with the grid points placed uniformly and the radial direction has 180 grid points with initial grid spacing of 2×10^{-4}. The spanwise direction has 30 grid points with the grid extending from 0.0 to 2.0 and the grid points are placed uniformly. The boundary conditions applied and the initialization of the transport variable of the SA-DES turbulence model are same as in the previous test case of a 3D circular cylinder at a $Re = 140{,}000$. The Reynolds number used for this test case is $Re = 3900$.

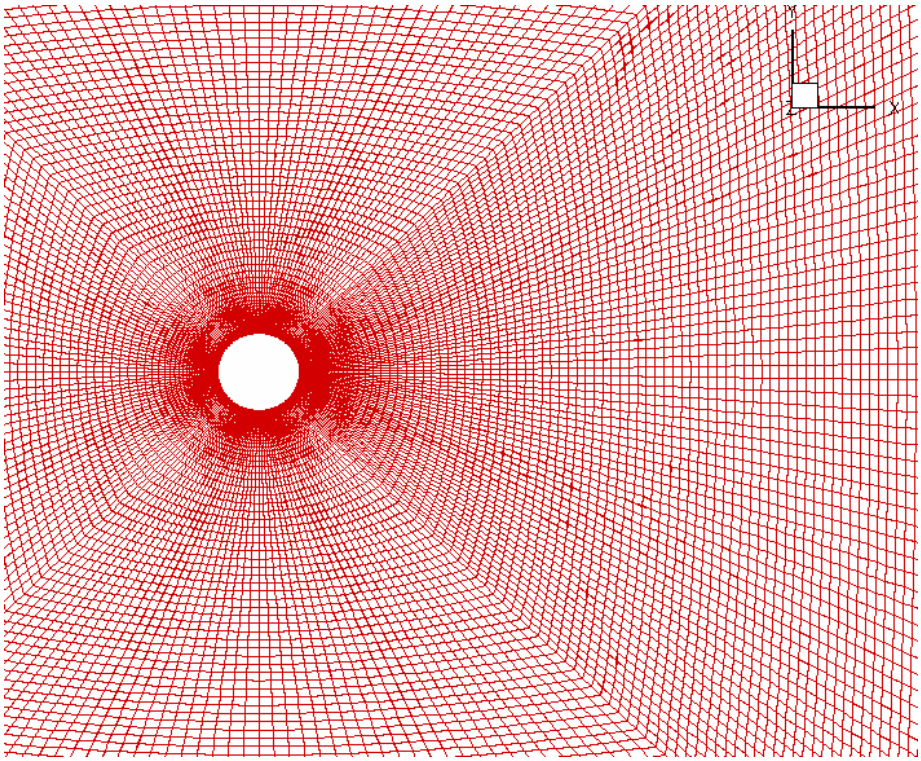

Figure 5-29 Snapshot of grid for *Re* = 3900

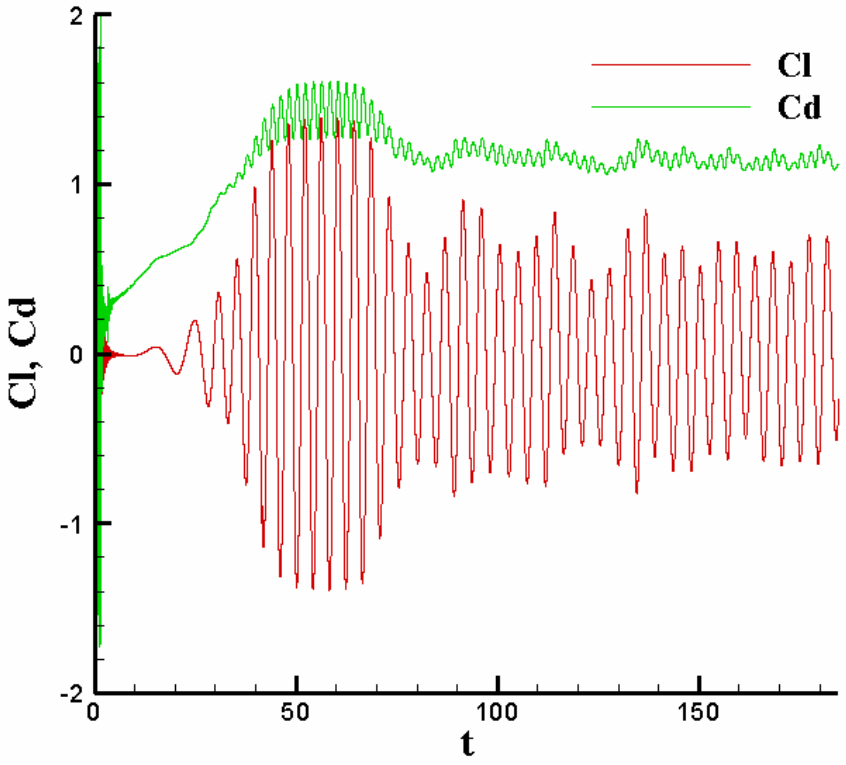

Figure 5-30 Lift-Drag Plot of 3D Cylinder at Re = 3900

The lift-drag plot is presented in Figure 5-30. The mean drag coefficient for this test case is 1.1495, averaged over ~105T (from 79T to 184T), which is higher than the experimental value of 0.99 ±0.05, as referred in [87]. The pressure distribution and the skin friction coefficient distribution at the surface of the cylinder averaged over time and space presented in Figure 5-31 are compared with the CFD simulation results by Amit *et al* [88] and with the experimental results by Norberg [89] at *Re* = 4200. Amit *et al* [88] did the simulation for a 3D cylinder flow using a grid composition of 100x100x30 with an initial grid spacing of 7.7×10^{-5} with the outer boundaries located at r/D = 75 at a Reynolds number of *Re* = 3900 using LES technique. Experiments on the cylinder flow were conducted in a wind tunnel section by Norberg [89] up to the Reynolds number of 4×10^4. The height, width, and length of the wind tunnel section are 1.25 m, 1.8 m, and 2.9 m respectively and the tests were conducted for various diameters of the cylinder, D = 0.2, 0.5, 1, 2, 6, and 20 mm. The pressure coefficient values were low when compared with the results by Amit *et al* [88] and Norberg [89]. However, the lower values of the

pressure coefficient in the separation region can be corrected for the blocking effect. Corrections accounting for the blocking effects must be considered which might give better pressure coefficient values. The correction factor [91] that is applied to the pressure coefficient values is given as,

$$c_{pc} = 1 - \left(1 - c_p\right) \Big/ \left(1 + \varepsilon\right)^2 , \tag{5.4}$$

where, ε is the ratio of the diameter of the circular cylinder to the total width of the domain, which is 1/30. After the correction of c_p values the pressure distribution at the surface is in much better in agreement with the other results. The corrected pressure coefficient plot is presented in Figure 5-32. In the profile the maximum value of pressure coefficient is at θ = 0°, the decrease in the slope of the pressure coefficient curve can be observed and the minimum of the pressure coefficient value can be observed at θ = 72°, the flow separates at θ = 90° and the recovery is only after θ = 102°. When compared to other results, occurrence of the recovery and the minimum value of c_p differ on the order of 2° which may be due to the lack of sufficient back pressure due to the lack of much finer grid in the wake region.

It should be mentioned here that there is a correction factor involved with the lift and drag coefficients also as the square of the freestream velocity is used in calculating these terms. However, there are complications involved in correcting these terms as the evaluation of these terms involves both the pressure and the skin friction terms. Hence, the proposed solution for this problem is to expand the outer boundaries and employ a finer grid in the wake region.

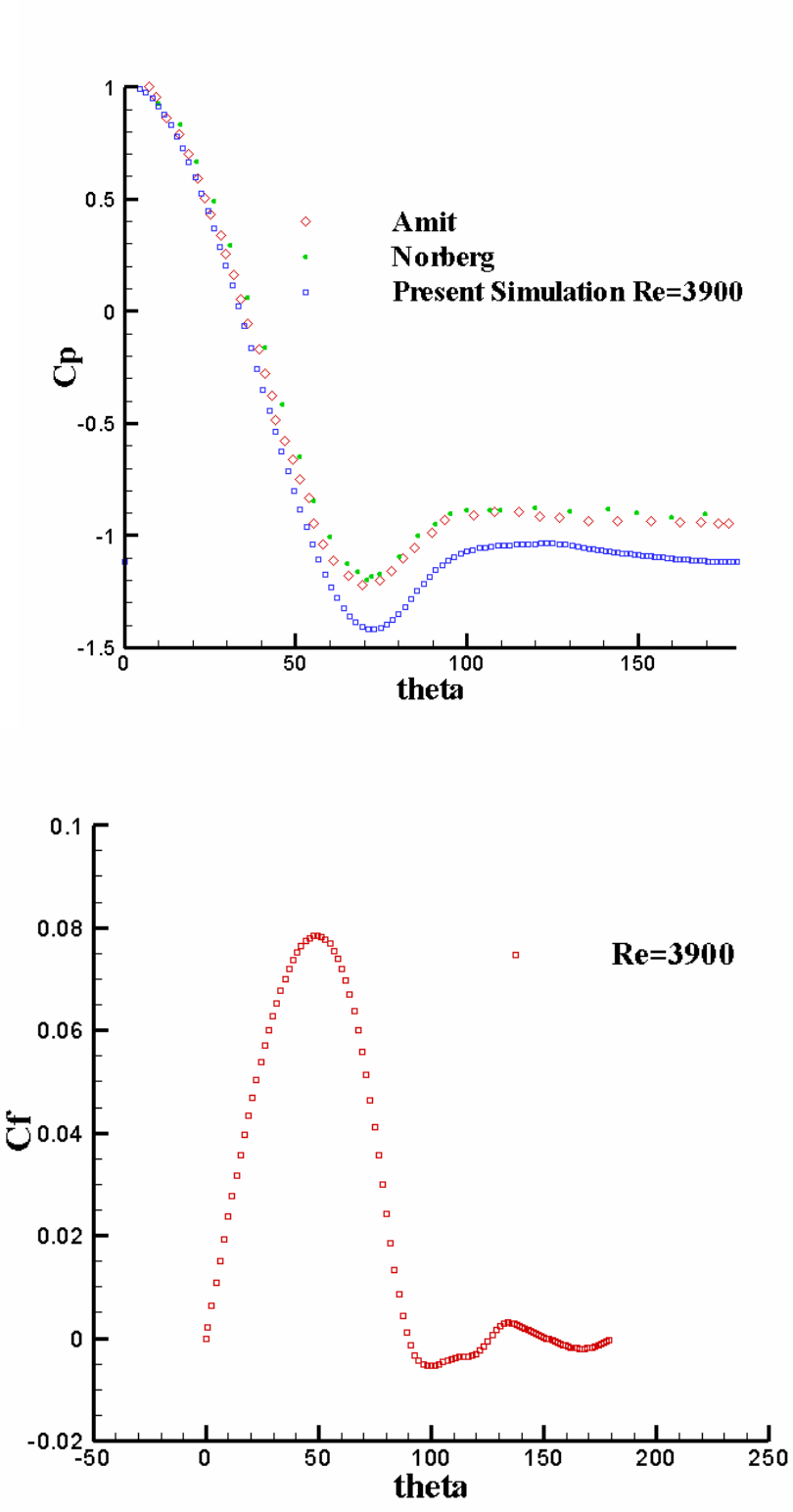

Figure 5-31 (a) Pressure plot and (b) Skin friction coefficient of 3D cylinder at *Re* = 3900

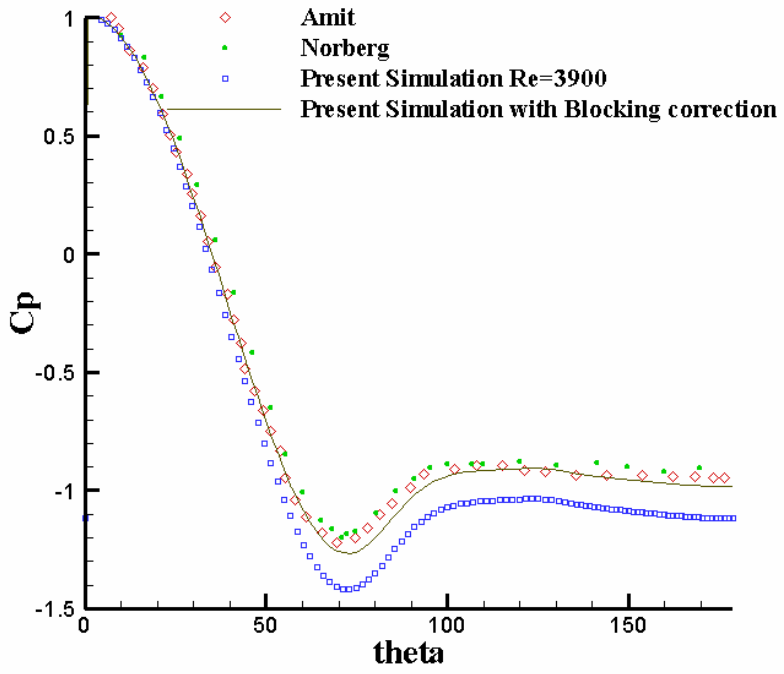

Figure 5-32 Pressure distribution on the surface of 3D cylinder with blocking corrections

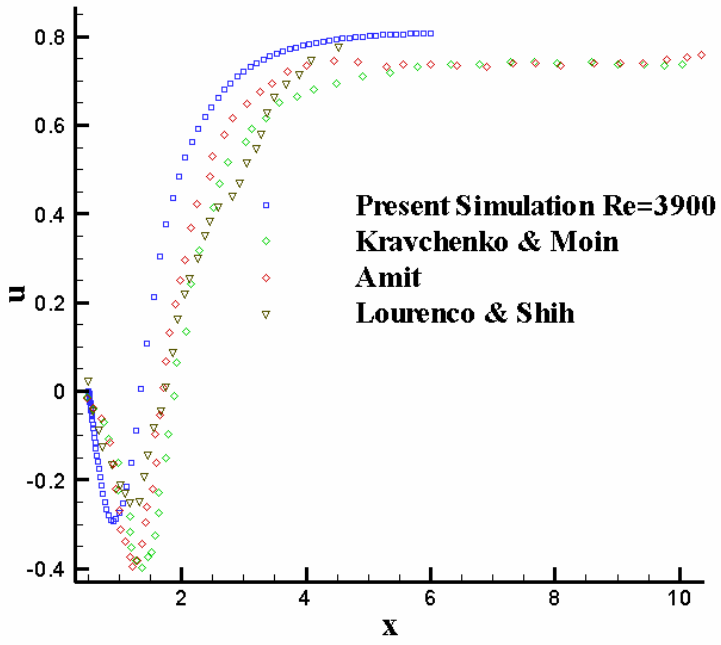

Figure 5-33 Centerline velocity plot of 3D cylinder at *Re* = 3900

The centerline velocity profile averaged over time and space is presented in Figure 5-33. The velocity profile is compared with the experimental results by Lourenco and Shih [90] referred from Kravchenko and Moin [87], results from the numerical simulation Kravchenko and Moin [87] at Re = 3900, and Amit *et al* [88] at Re = 3900. Kravchenko and Moin [87] performed numerical simulations of the flow over a 3D cylinder with a grid composition of 185x205x48 with the outer boundaries located at 60R (R = 0.5, radius of the cylinder) at a Reynolds number of Re = 3900 using the LES technique. The velocity profile has a good magnitude match at the minimum value of -0.29 when compared with the experimental result by Lourenco and Shih [90] at -0.25, while the minimum values of the profiles by Kravchenko and Moin [87] and Amit *et al* [88] occurring at -0.3969 and -0.3939 respectively which happen to be much lower. However, the velocity recovery at the lower end and the slope of this profile comes up a little earlier compared to the other results. The magnitude of the velocity profile at the higher end, which is approximately 0.79, is in agreement with the experimental [90] value of 0.776 at the higher end, notably better than the other simulations.

As discussed in the previous section, in order to observe the velocity distribution in the wake region four points were picked up in the lift oscillation as shown in Figure 5-34.The mean of the velocity distribution at the above discussed four points on the lift oscillation is taken and also are averaged over the spanwise direction. The velocity profiles in the streamwise direction at three different points in the wake region, x = 1.06, x = 1.54, and x = 2.04, are presented in Figure 5-35(a) and also for comparison velocity profiles by Amit *et al* [88] are presented in Figure 5-35(b). Even though quantitatively the velocity magnitudes are low compared with the results by Amit *et al* [88], the profiles have a qualitative match. The minimum values of the velocity profiles at the three positions, x = 1.06, x = 1.54, and x = 2.04, are -1.257, -0.8129, and -0.484 respectively and the results by Amit *et al* [88] have the minimum values of -1.4, -1.2, and -0.8 respectively. It should be mentioned that the velocities have been averaged over only one time interval and longer integration over time intervals is needed to be in a position to accurately compare with the results by Amit *et al* [88]. Also, the velocity profiles in the cross-flow direction at three different points in the wake region, x = 1.06, x = 1.54, and x = 2.04, are shown in Figure 5-36(a) and the results by Amit *et al* [88] are presented for comparison in Figure 5-36 (b). The magnitudes of the velocities at higher end of the oscillation at x = 1.06, x = 1.54, and x = 2.04 are 0.3, 0.28, and 0.18 respectively and results by Amit *et al* [88] have 0.15, 0.3, and 0.25

respectively. And the magnitude of velocities at lower end of the oscillation at $x = 1.06$, $x = 1.54$, and $x = 2.04$ are -0.255, -0.232, and -0.125 respectively and results by Amit *et al* [88] have -0.2, -0.3, and -0.2 respectively. Similar to the streamwise velocity profiles, the velocity profiles in the cross-flow direction are qualitatively in match with the results by Amit *et al* [88], except at $x = 1.06$ where the double oscillation is the results by Amit *et al* [88] is missing in the present simulation, and quantitatively differ when compared in terms of magnitude of the velocity. Again, longer integration over time intervals is required in order to be able to more accurately compare with the simulation results by Amit *et al* [88].

Instantaneous contour plots for the streamwise, cross-flow, and spanwise velocities in the YZ plane are presented in Figure 5-37 along with the contour interval values in Table 5-4. As discussed in earlier section, reason for presenting these contours is to understand the velocity distribution in the wake region. Also, the instantaneous contour plot of $\overline{w'^2}$ with the contour intervals of 0.002 is presented in Figure 5-38. The non-zero values of $\overline{w'^2}$ confirm the three dimensionality of the simulation. In order to observe the vortex structures in the wake region, the instantaneous plot of the iso-surfaces of vorticity magnitude is presented in Figure 5-39.

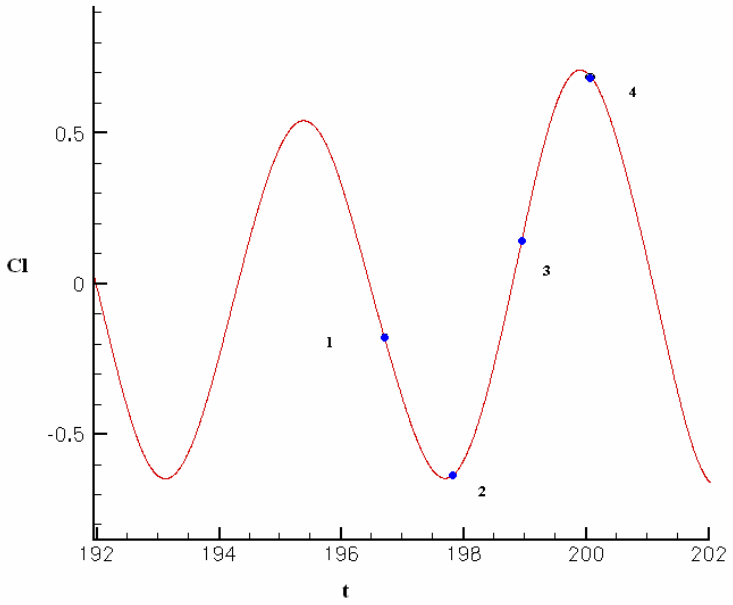

Figure 5-34 Lift oscillation at *Re* = 3900

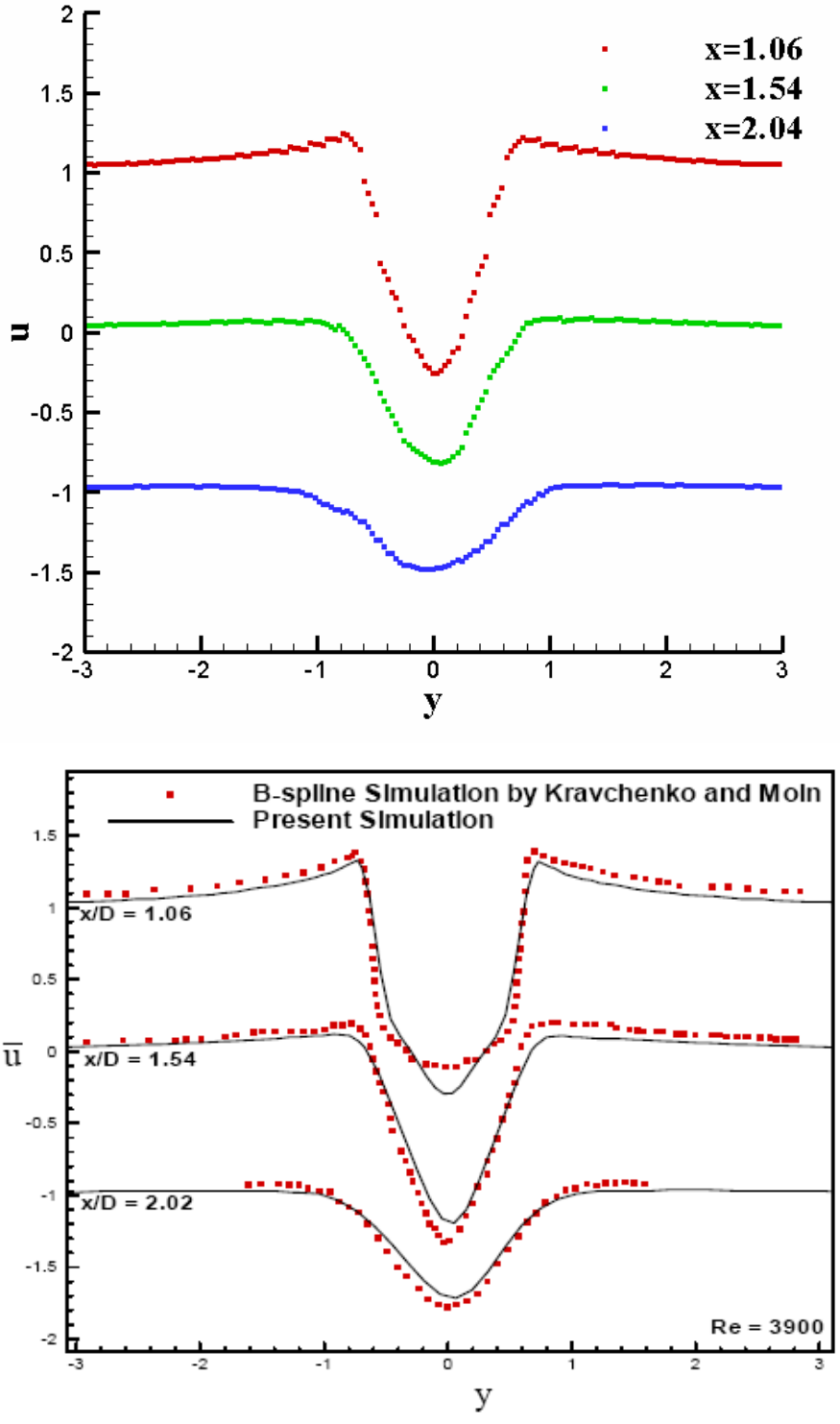

Figure 5-35 Velocity profile in streamwise direction (a) Current simulation (b) Amit *et al* [88] and Kravchenko and Moin [87] at *Re* = 3900

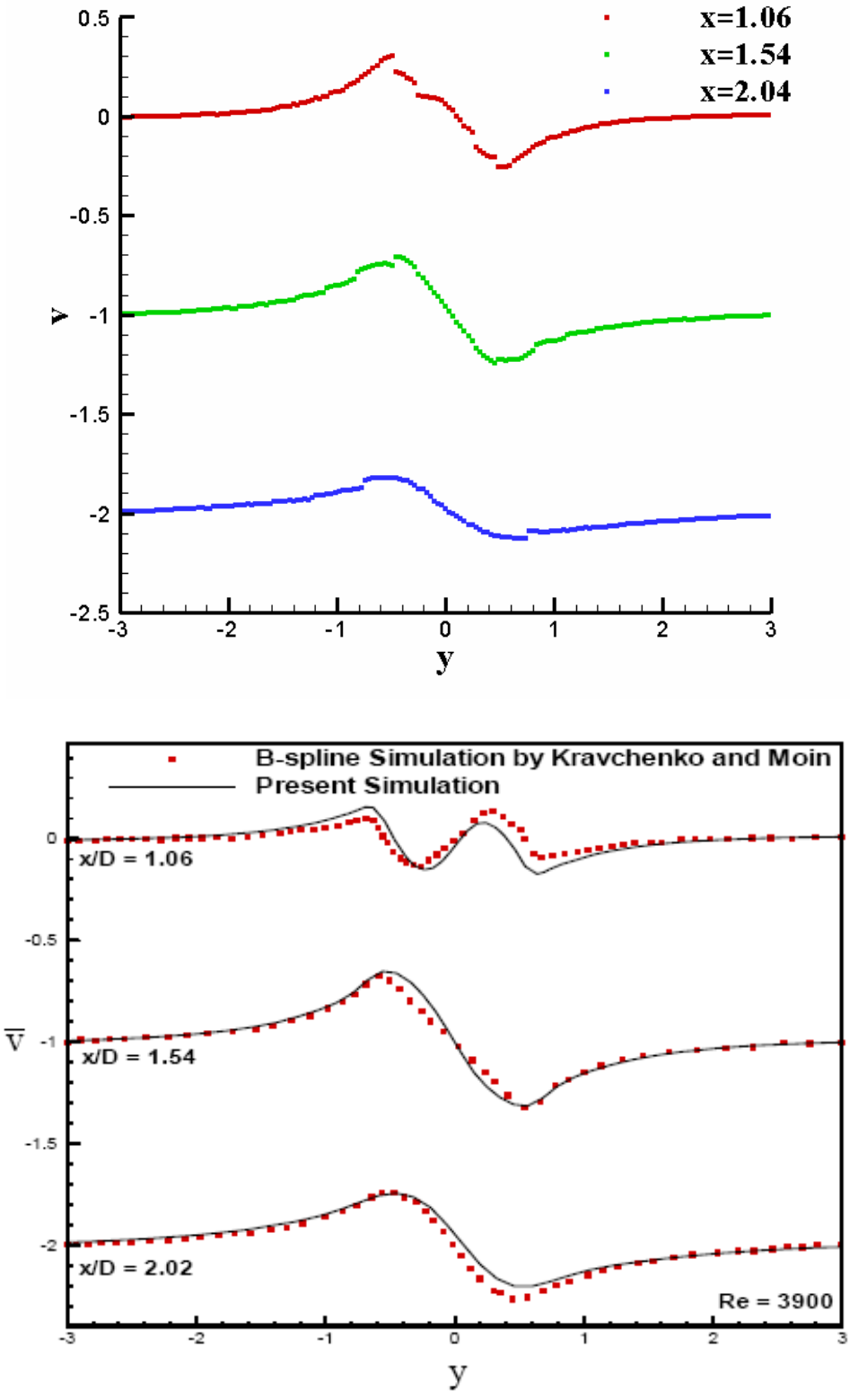

Figure 5-36 Velocity profile in cross-flow direction (a) Current simulation (b) Amit *et al* [88] and Kravchenko and Moin [87] at *Re* = 3900

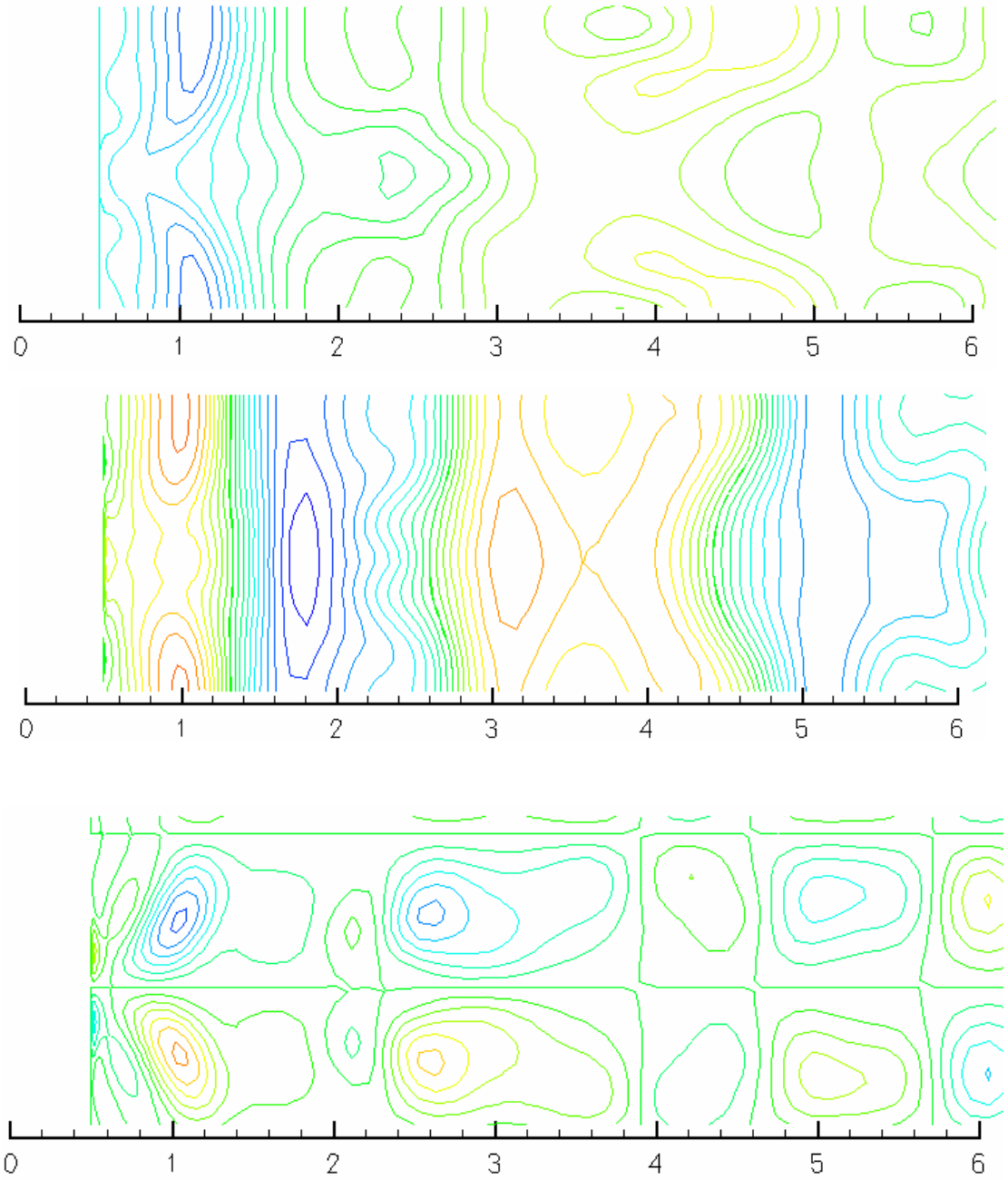

Figure 5-37 Contour plots for (a) Streamwise (top) (b) Cross-flow (middle) and (c) Spanwise velocities (bottom)

Table 5-4 Contour intervals for the streamwise, cross-flow, and spanwise velocity contour plots

	Contour intervals
u	0.1
v	0.085
w	0.035

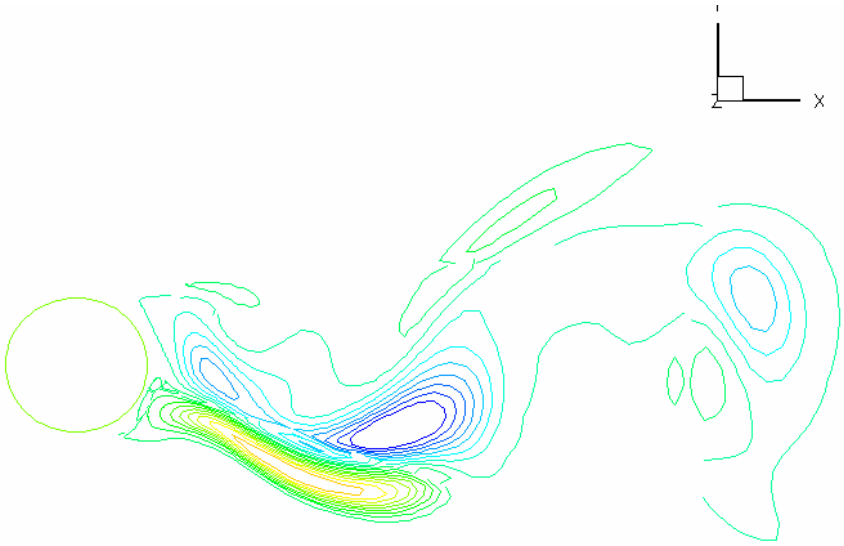

Figure 5-38 Contours of $\overline{w'^2}$

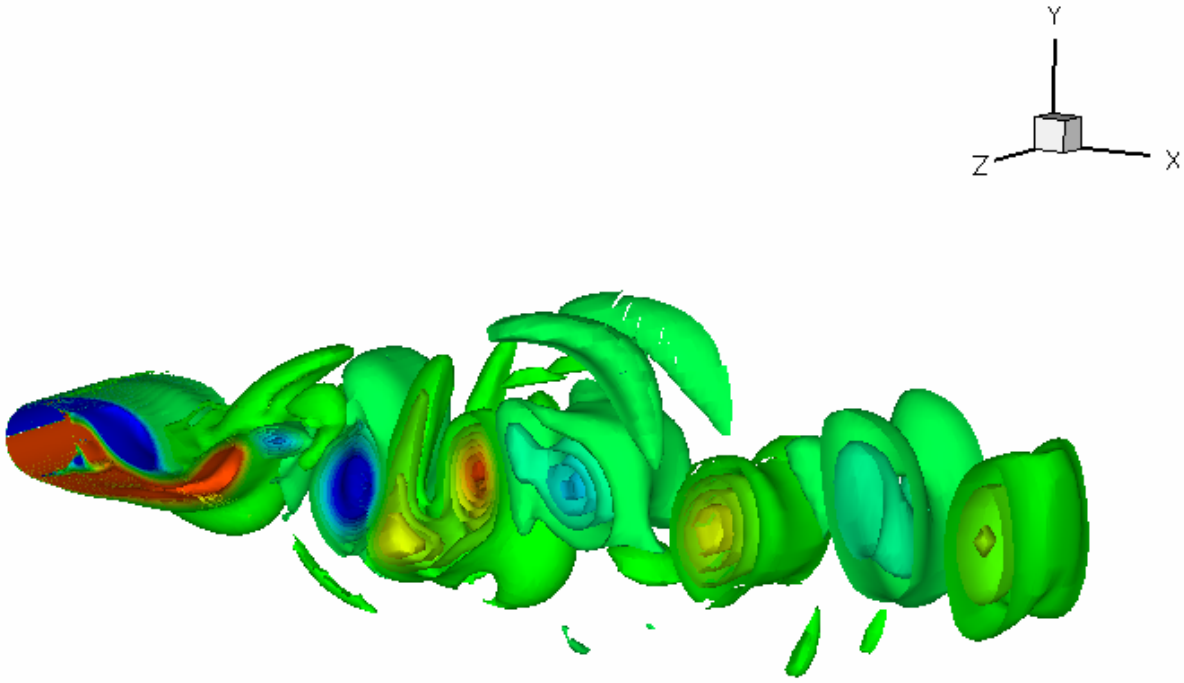

Figure 5-39 Iso-surfaces of vorticity magnitude

This simulation has a better grid density compared to the previous simulation. The pressure distribution at the surface with the blocking correction has a better match with other results. The other discrepancies in the results may be due to the insufficient grid density in wake region when compared with others simulations or experiments.

5.4.3 SA-DES case in UNCLE with Re = 13400

The test case carried here uses a grid with finer grid spacing near the wall when compared with the earlier test case with the Reynolds number, *Re* = 3900. The grid generation approach is the same as the one discussed in chapter 4 in the GAMBIT grid generation section. The grid for this test case has a grid size of 226x160 with 226 grid points in the circumferential direction and 160 in the radial direction. The inner region in the wake region has a grid size of 76x120 with 76 grid points in the circumferential direction and 120 in the radial direction. The initial grid spacing is $5x10^{-5}$, such that the first grid point is typically inside the sublayer. The spanwise direction stretches from 0.0 to 2.0 with 30 grid points uniformly spaced. The boundary conditions applied and the initialization of the transport variable of the SA-DES turbulence model are same as in the previous test case of a 3D circular cylinder at a *Re* = 140,000. The Reynolds number used for this case is *Re* = 13400.

The pressure distribution and the skin friction coefficient distribution averaged in time and space at the surface of the cylinder are presented in Figure 5-40. The pressure coefficients at the separation region are much lower compared to the experimental results by Sarioglu [91] at a Reynolds number *Re* = 16024 and the computational results by Amit *et al* [88] for flow over a cylinder at a Reynolds number *Re* = 13400 using a LES technique using 3.9 million grid points with 48 grid points in the z-direction with an initial grid spacing of $6.9x10^{-5}$ and the outer boundaries located at r/D = 100. Experiments for flow over circular and square cylinder were conducted in a wind tunnel section in the range of Reynolds numbers $1.3x10^{4}$ to $2x10^{5}$ by Sarioglu [91]. The wind tunnel has a width of 289 mm, height of 457 mm, and length of 1830 mm. The diameter of the circular cylinder is 50 mm. Comparison with the results by Sarioglu [91] is justified as both the Reynolds numbers *Re* = 13400 and *Re* = 16024 are in the same regime of transition in the shear layers. The lower pressure coefficient values even after the blocking correction can be due to the lack of integration over a sufficient number of time

intervals (depending on a specific flow conditions) and also may be due to the insufficient grid points in the wake region. However, after correcting for blocking the minimum value of the pressure coefficient occurs at $\theta = 74°$, the flow separates at $\theta = 90°$, and the recovery of the pressure curve occurs after $\theta = 125°$. There was no data available for the comparison of the skin friction coefficient values and hence the result from the previous test case with $Re = 3900$ is used to show the difference in the skin friction coefficient with increase in Reynolds number. However, it should be mentioned here that to obtain a solution that is in a position to be compared with other results requires averaging over longer time intervals while the current simulation is only averaged over 8 oscillations for a non-dimensional time of ~30T. The centerline velocity plot averaged in time and space is presented in Figure 5-41. Also, as there is no data available for comparison, the velocity at the centerline in this simulation is compared with the centerline velocity values from the previous test case at $Re = 3900$.

Mean velocity profiles in the streamwise and the cross-flow directions averaged over time and space are shown in Figure 5-42 and Figure 5-43. The velocity profiles are presented at the positions $x = 1.06$, $x = 1.54$, and $x = 2.04$. These profiles are compared with the computational results by Amit *et al* [88]. Even though there is a qualitative match between the current simulation and results by Amit *et al* [88], except cross-flow velocity profile at $x = 1.06$ where the double oscillation in the result by Amit is missing in the present simulation, it can be observed that current simulation is falling short in magnitude when compared quantitatively. The minimum values of the velocity profiles in the streamwise direction for three positions in the wake region, $x = 1.06$, $x = 1.54$, and $x = 2.04$, are -1.065, -0.55, and -0.37 respectively, and the simulation result by Amit *et al* [88] have the minimum values of -1.4, -1.1, and -0.7 respectively. In the cross-flow direction the magnitudes of the velocities at the higher ends of the oscillations at $x = 1.06$, $x = 1.54$, and $x = 2.04$, are 0.37, 0.21, and 0.11 respectively and results by Amit *et al* [88] have the values 0.2, 0.32, and 0.2 respectively. The magnitudes of the velocities at the lower ends of the oscillations at $x = 1.06$, $x = 1.54$, and $x = 2.04$, are -0.36, -0.17, and -0.085 respectively and results by Amit *et al* [88] have the values -0.3, -0.3, and -0.15 respectively. The reason for the discrepancies in the magnitudes of the velocity distributions can be insufficient integration over sufficient number of time intervals. However, the nature of low magnitude of the minimum values in these mean velocity profiles are consistent with the lower minimum value of the centerline velocity behind the cylinder.

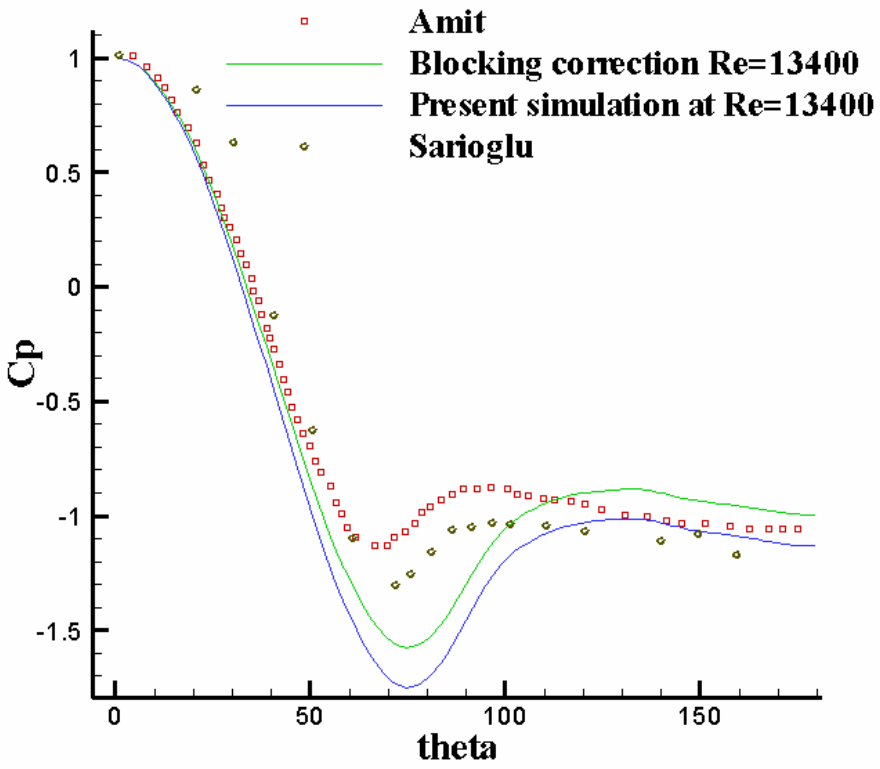

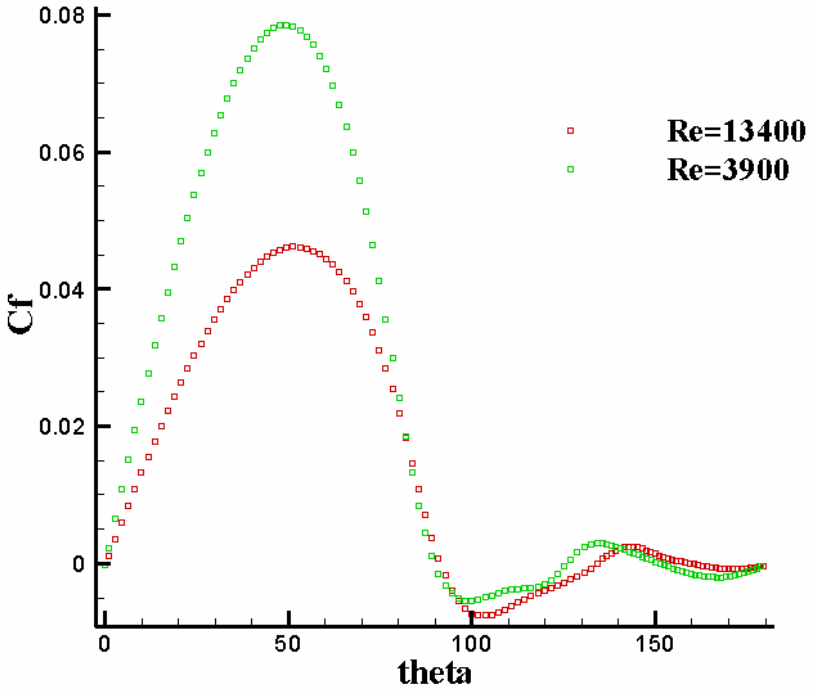

Figure 5-40 (a) Pressure plot and (b) Skin friction coefficient plot at *Re*=13400

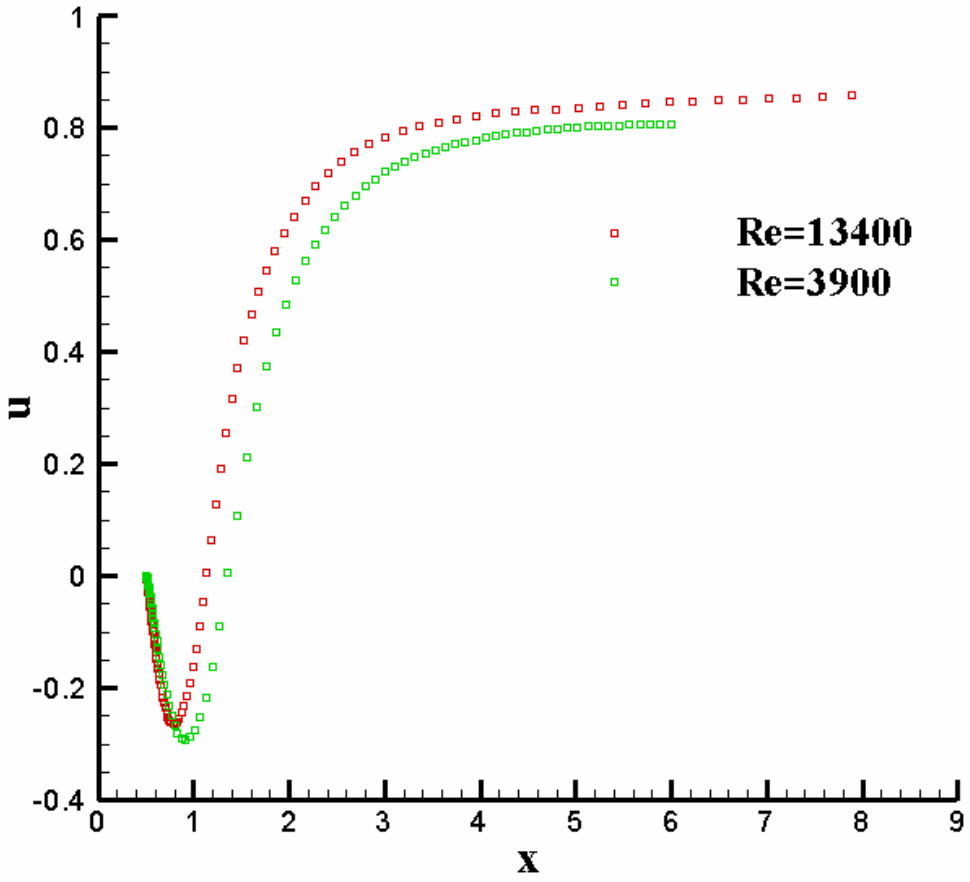

Figure 5-41 Centerline velocity plot at *Re*=13400

Instantaneous contour plots for the streamwise, cross-flow, and spanwise velocities in the YZ plane, the instantaneous contour plot of $\overline{w'^2}$ with the contour intervals of 0.002, and the instantaneous plot of the iso-surfaces of vorticity magnitude are presented in Figure 5-44, Figure 5-45, and Figure 5-46 respectively. The contour interval values for the contour plots for the streamwise, cross-flow, and spanwise velocities is presented in Table 5-5. Velocity contours represent the velocity distribution in the wake region. The non-zero values of $\overline{w'^2}$ confirms the three dimensionality of this simulation. And the vortex structures in the wake region can be observed in the iso-surface plot of the vorticity magnitude.

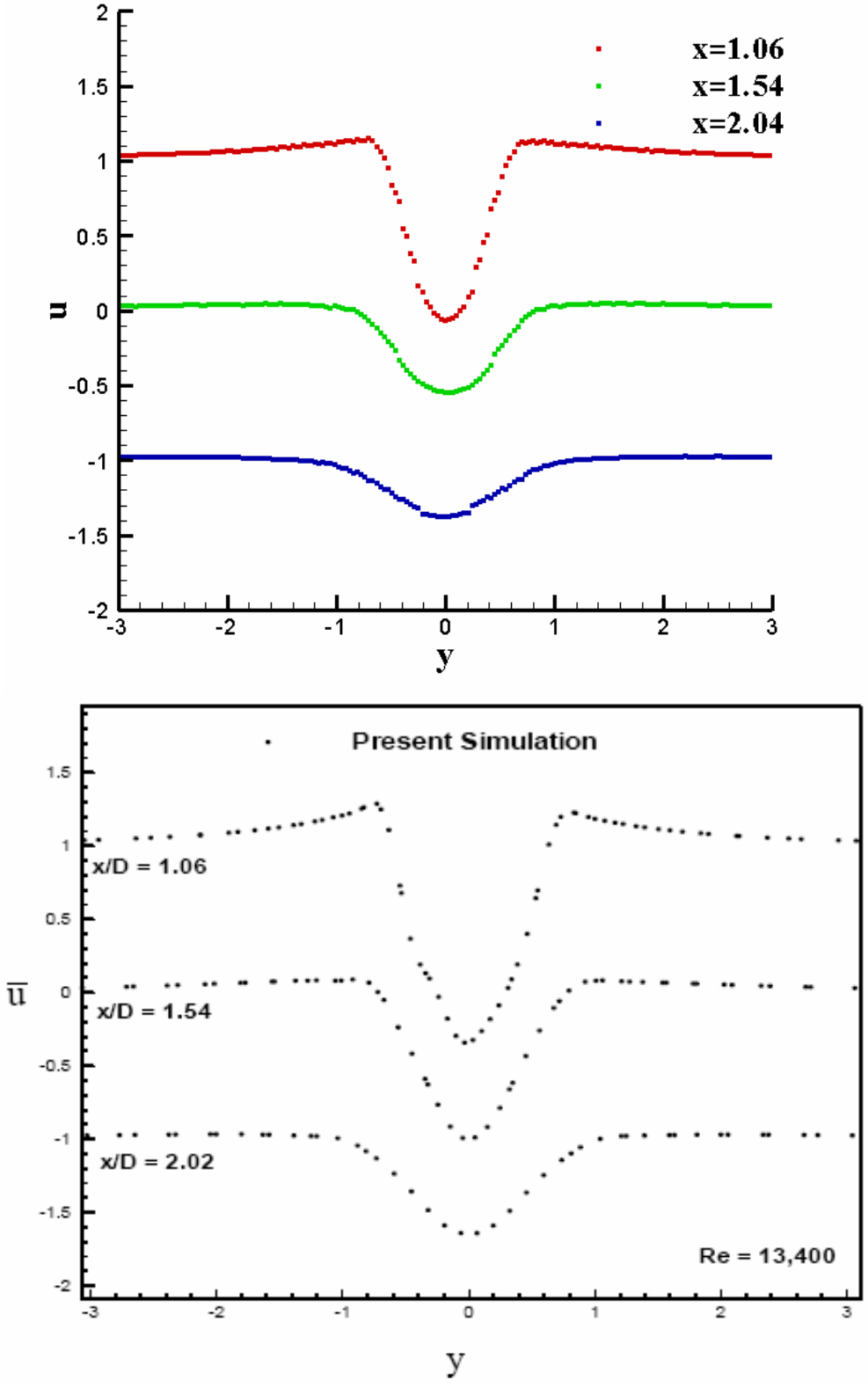

Figure 5-42 Mean velocity profiles in streamwise direction (a) Current simulation and (b) Amit *et al* [88]

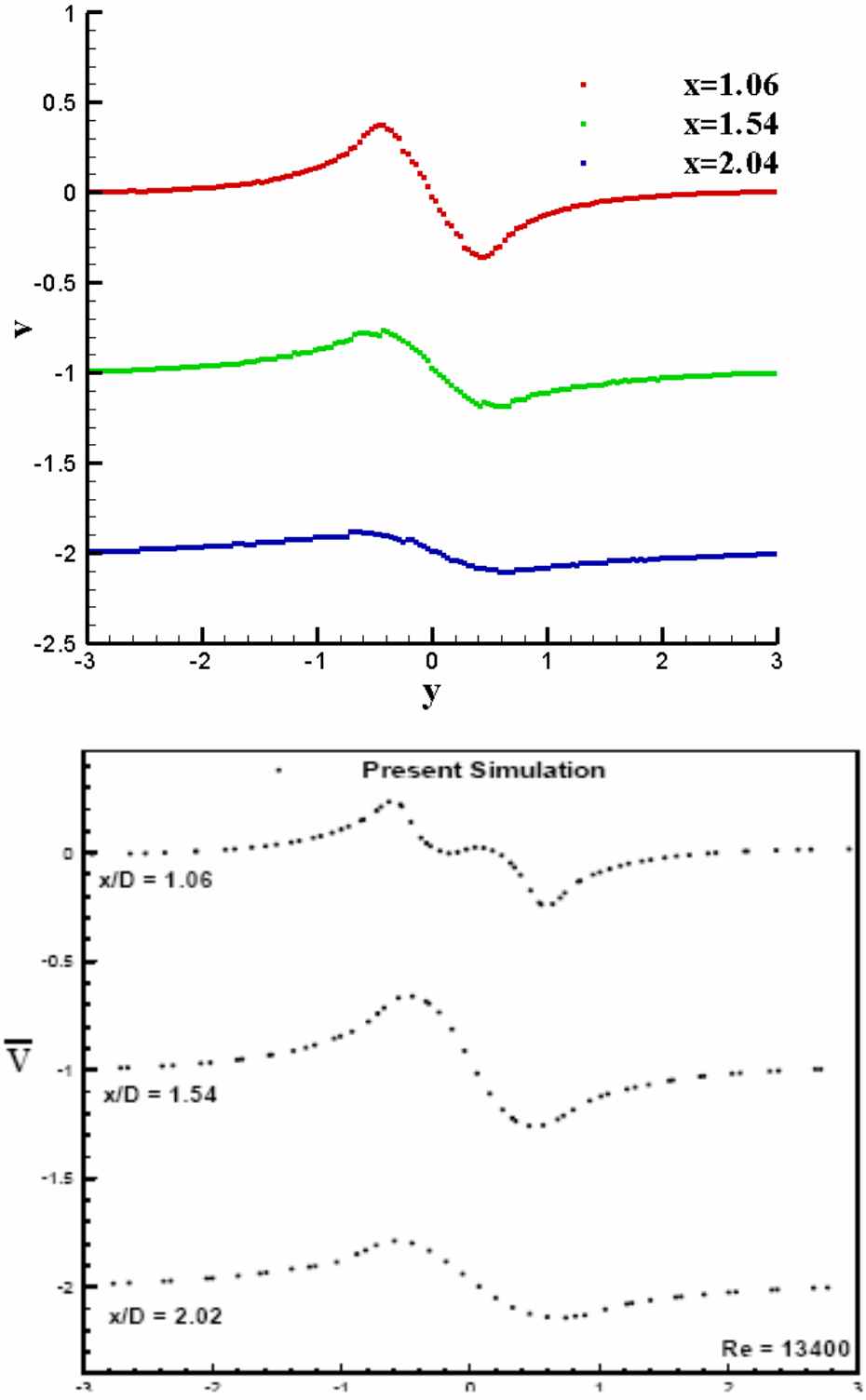

Figure 5-43 Mean velocity profiles in cross-flow direction (a) Current simulation and (b) Amit *et al* [88]

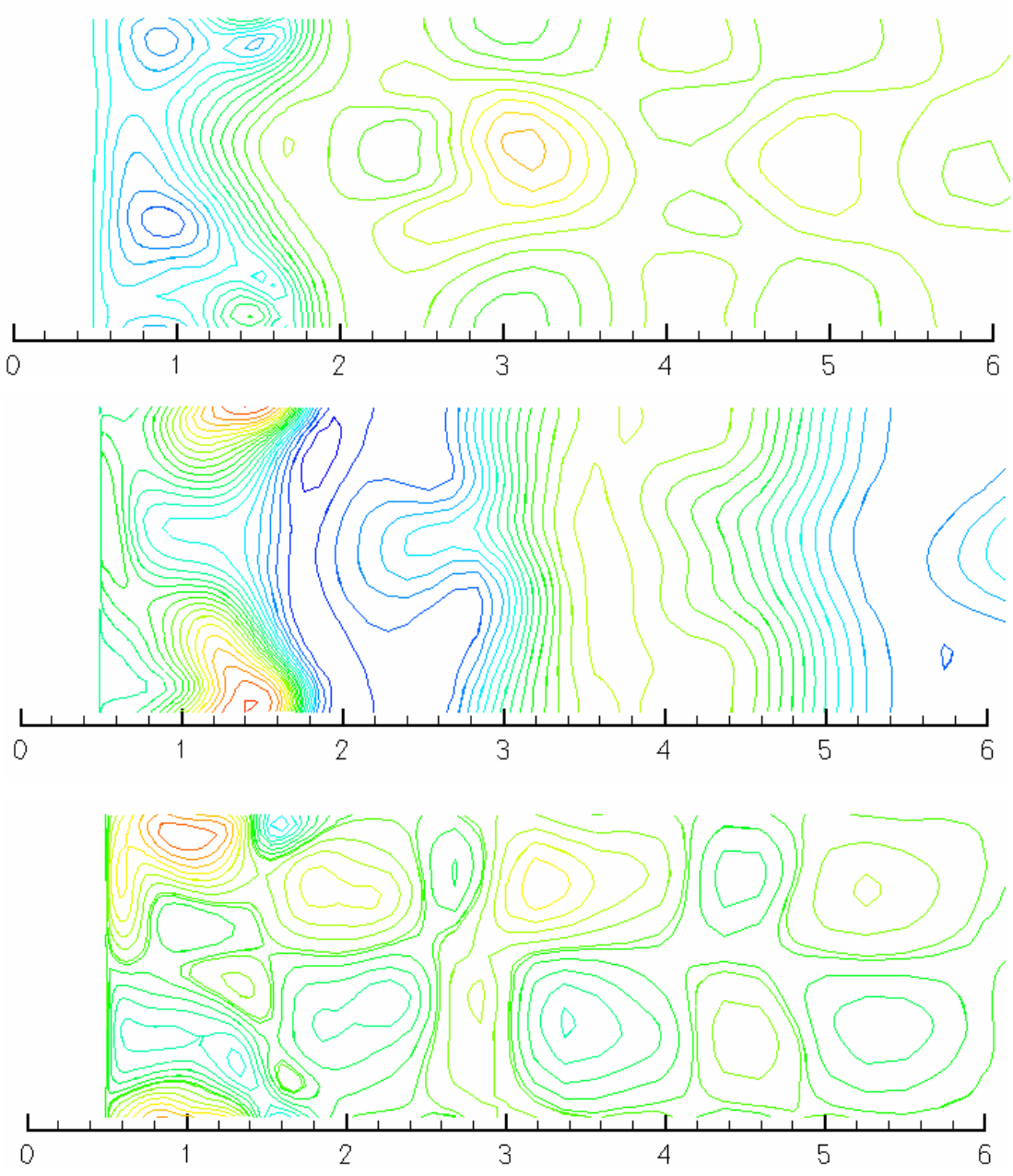

Figure 5-44 Contour plots for (a) Streamwise (top) (b) Cross-flow (middle) and (c) Spanwise velocities (bottom)

Table 5-5 Contour intervals for the streamwise, cross-flow, and spanwise velocity contour plots

	Contour intervals
u	0.1
v	0.1
w	0.054

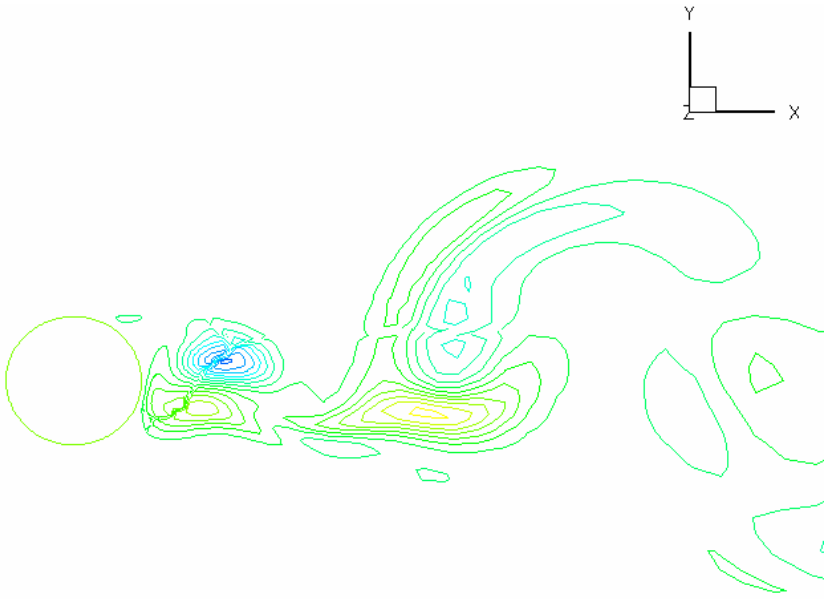

Figure 5-45 Contours of $\overline{w'^2}$

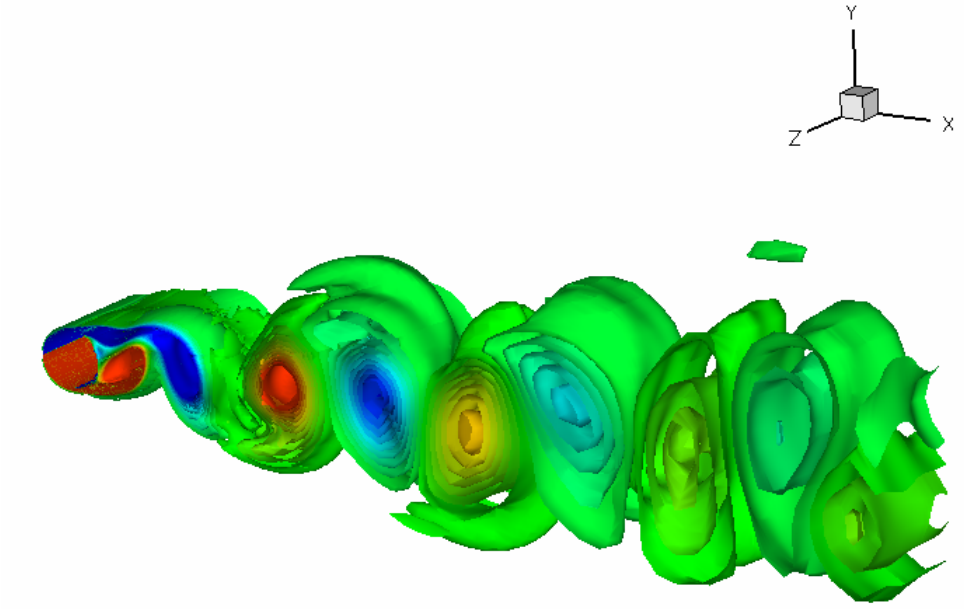

Figure 5-46 Iso-surfaces of vorticity magnitude for *Re* =13400

This test case has an improved grid density and initial grid spacing compared to the earlier simulations. To get better results longer integration over time intervals might be required.

5.4.4 SA-DES case in UNCLE with Re =140000 (Fine grid)

In this test case the same grid that is used in the previous test case with *Re* = 13400 is employed to carry out this simulation. The initial and the boundary conditions are same as the conditions in earlier 3D simulations. However, the results presented in this section are averaged only over less than an oscillation.

The pressure distribution at the surface of the cylinder averaged in time and space is presented in Figure 5-47. The results are compared with the same experiments and CFD simulations as in case of the first test case with *Re* = 140000 with a coarse grid. However, in order to compare the difference in the simulation results with coarse and finer grids, the results from the first 3D test case with the coarse grid with *Re* = 140000 is compared with the present simulation with a relatively finer grid at the same Reynolds number. The minimum pressure coefficient occurs at θ = 78°, flow separates at θ = 105°, and the recovery region is after θ = 115°. The skin friction coefficient distribution averaged in time and space is presented in Figure 5-48. The comparison is again with the same experiments and numerical simulations as In case of the first 3D test case with *Re* = 140000.

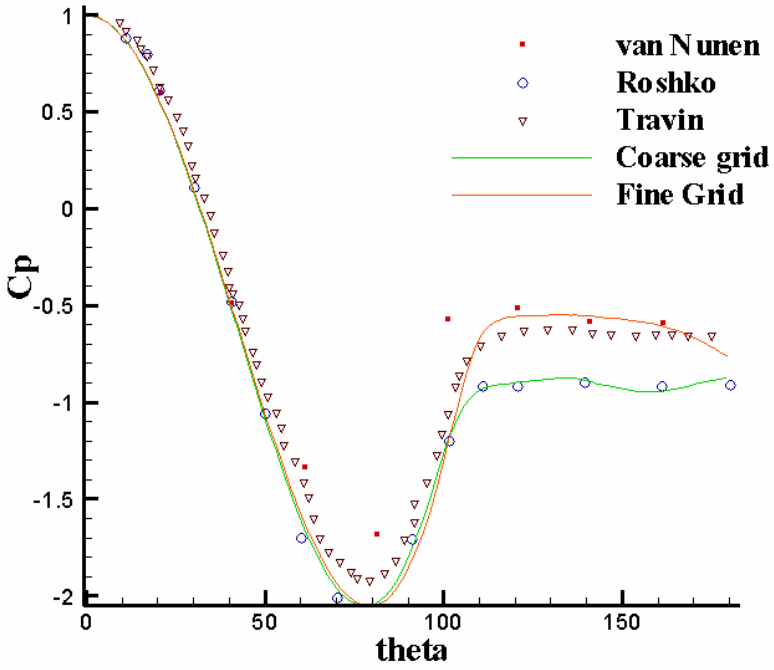

Figure 5-47 Pressure distribution at the surface of the cylinder at *Re* = 140000 (Fine grid)

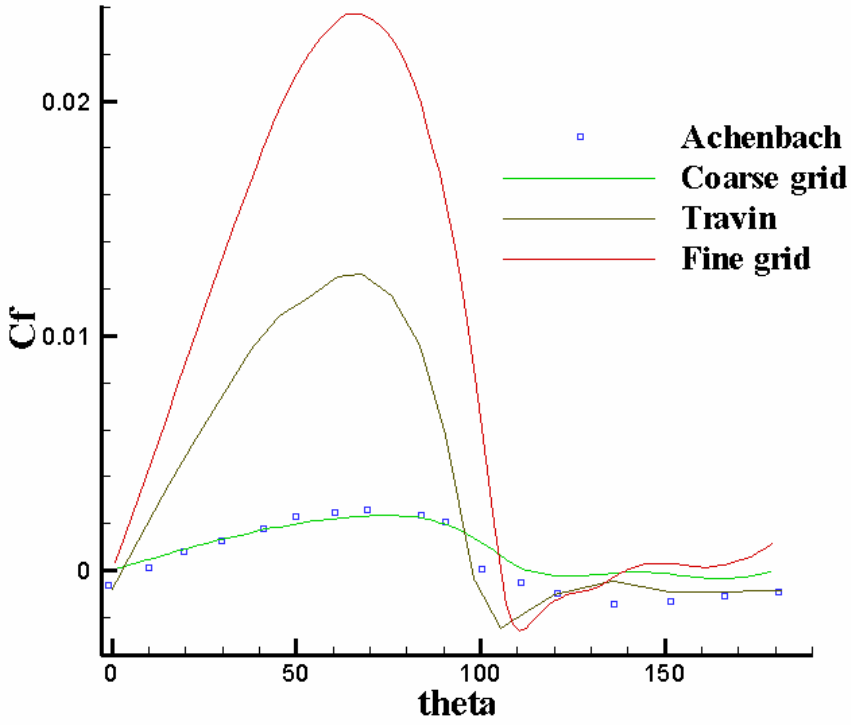

Figure 5-48 Skin friction coefficient distribution at the surface of the cylinder at *Re* = 140000 (Fine grid)

5.4.5 SAS case in UNCLE with Re=3900

As discussed in Chapter 4, along with the SA-DES model, the SAS hybrid turbulence model is implemented in the unstructured grid code, UNCLE. This simulation is the first step towards the validation of the SAS model in UNCLE code. This simulation is run at a Reynolds number of *Re*=3900. The grid size is 225X159X15 with the initial spacing of $5\text{x}10^{-5}$. The reasons for considering less number of grid points in spanwise direction is to reduce the computational time for the basic test and to confirm if the basic implementation of the model is functional in the model. The initial condition for the transport variable of the SAS model is $\nu_t = 5\nu$, where ν is the molecular viscosity. The inflow boundary condition has, $\nu_t = 5\nu$ and the outflow boundary

condition has, $\partial \nu_t / \partial x_i = 0$. No slip condition is applied at the wall boundary and the transport variable has, $\nu_t = 0$. Periodic boundary conditions are applied in the spanwise direction.

Better initial conditions are used for this simulation to avoid the computational time taken to overcome the initial noise in the flow. The concept of initial restart file is discussed in Chapter-4. Figure 5-49 shows the lift-drag plot where the simulation is started with an initial restart file, which is with better initial conditions. Figure 5-50 represents the SAS simulation started with out using the better initial conditions. Due to the double derivative term of velocity in the length scale calculation of the SAS model, the model is sensitive to the radical change in time step and requires a smaller time step of ~$1x10^{-6}$. Hence, when started without better initial conditions, the time step used to start the simulation was $1x10^{-6}$ and the noise part was oscillating on the order of 10^3 as observed from Figure 5-50.

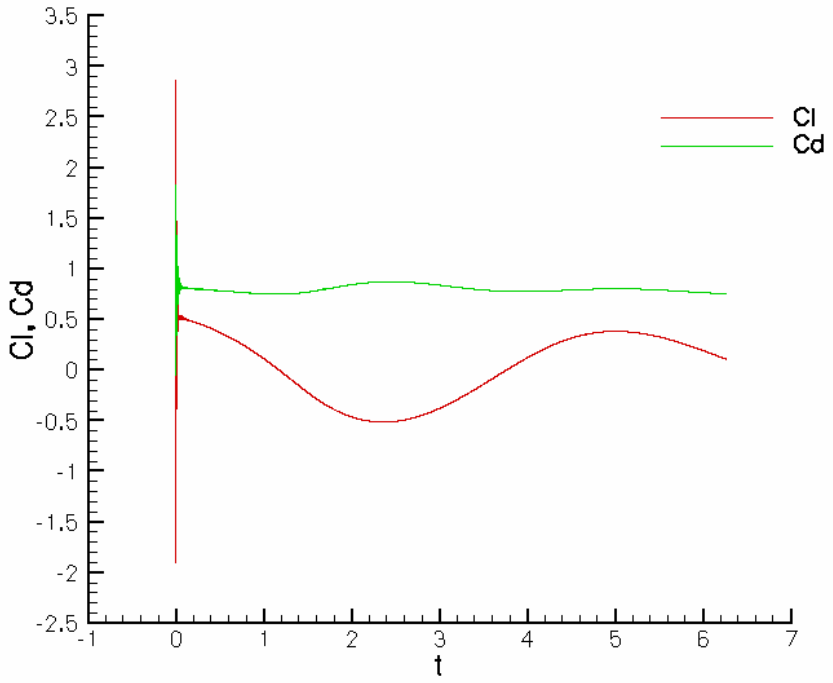

Figure 5-49 Lift-Drag plot for SAS model with better initial conditions at *Re* = 3900

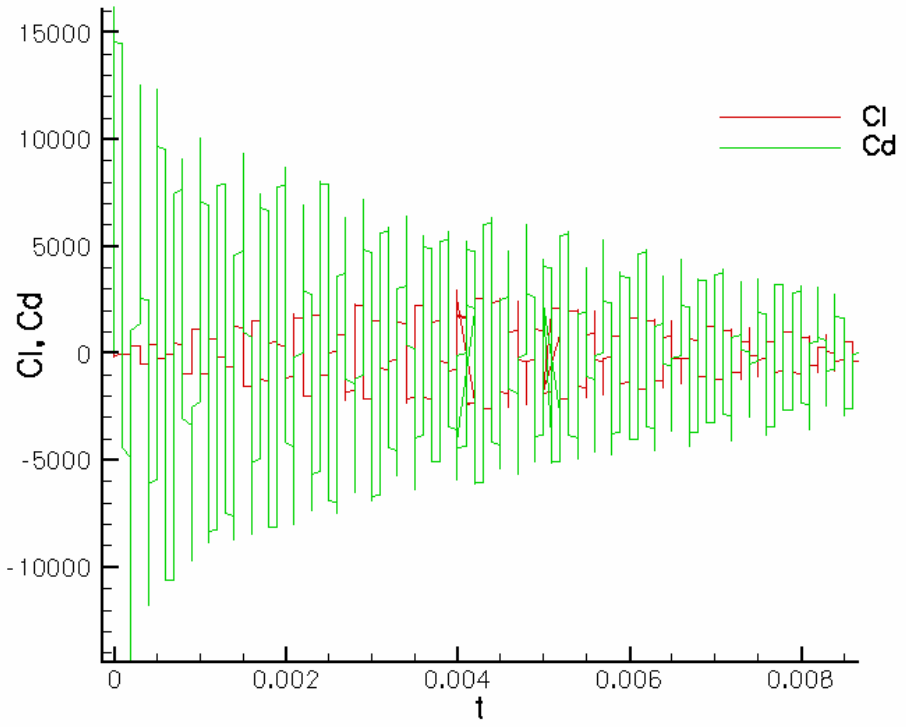

Figure 5-50 Lift-Drag plot for SAS model with out better initial conditions at *Re* = 3900

This is the currently ongoing simulation and more time is required for the confirmation of the functioning of the SAS model.

Chapter 6 : CONCLUSIONS AND FUTURE WORK

6.1 Summary and Conclusion

The implemented SA and SA-DES models in the UNCLE code have been tested and the results presented. Initially, the models are tested for a steady state flow over a two-dimensional flat plate with a Reynolds number, *Re* = 2000000 and are compared with the results from the GHOST code along with the SST models implemented in both the codes. The results from the SA models in UNCLE and GHOST are in agreement with each other indicating that the implementation of the SA model in both the codes is consistent. However, the SA models over predict the skin friction coefficient values when compared with the results predicted by SST model, but shape of the curve looks reasonable. The velocity profiles suggest that the implementation part is in the right path. A two-dimensional circular cylinder was considered as an initial test case for an unsteady flow. The models were tested for a relatively high Reynolds number, *Re*=140,000. Results for the SA model with laminar and turbulent initial flows, SA-DES model with laminar and turbulent initial flows, and the SST model with laminar initial flow in UNCLE were compared with each other. The results were compared with the available data from Travin *et al* [72] and the drag coefficients were considerably higher for all the cases and the lower pressure coefficient values were observed near the separation point. The skin friction plot revealed that there was a problem with the SST model in UNCLE and hence the further test cases were restricted to SA and SA-DES models in UNCLE. For a full fledged testing of the SA-DES model, unsteady flow over a three dimensional circular cylinder was considered as a test case. A coarser grid was used for the initial testing at a higher Reynolds number, *Re = 140,000*, to obtain results in a reasonably faster time to confirm the functioning of the implemented SA-DES model. It is to be noted that this test case employed a coarse grid to confirm the functioning of the model in less amount of computational time as coarse grids take less amount of wall time compared to fine grids. A relatively finer grid was employed to test the model for a low Reynolds number, *Re = 3900*. The results display lower values of pressure coefficient and higher

values of drag coefficients. This discrepancy is found to be due to the lack of correction to the freestream value for the blocking effects. When corrections were applied to the pressure coefficient values, the results were in very good agreement with the experimental values. Then the test case with *Re*=13400 with an improved grid in terms of initial grid spacing compared with the test case with *Re*=3900 is being simulated. The results obtained were averaged over 8 oscillations of the lift curve and requires averaging over more number of timer intervals.

Also, another simulation with the same grid which is used in case of *Re*=13400 was employed to simulated the flow over 3D cylinder with *Re*=140000, which was earlier simulated with a relatively coarser grid. This simulation has the results only with averaging over less than an oscillation of the lift curve. Finally, the simulation to validate the implemented SAS hybrid turbulence model is started.

Even though the goal of this thesis is to investigate the grid issues with the hybrid turbulence model, the DES model, it is only partially achieved due to the time constraint. A single three-dimensional simulation when run on the KFC5 machine takes about 20 hrs of wall time for 2000 iterations. The run time increases with the complexity of the problem, in this case when the Reynolds number is increased and when the grid is refined, and also due to CFDVAL criterion the time step used for a run should be decreased when the grid is refined. A full fledged run of a SA-DES model with a grid of 226X160X30 with an initial grid spacing of $5x10^{-5}$ on the KFC5 machine using 18 processors will take 10 – 12 weeks to complete.

6.2 Future Work

The future work needed for this project is to investigate the grey area effects on the Detached Eddy Simulation model. For this reason, highly controlled grids are to be constructed and a very good insight about the grids is recommended. The variation of the grey area region might be dependent on the method of calculation of the grid spacing, Δ. Hence, the test cases for future would be runs with higher Reynolds numbers with varying grid densities and variation of methods of calculating Δ. Also, the implemented SAS model in the UNCLE code is to be validated for the same set of Reynolds numbers on finer grids.

In order to overcome the errors due to the discrepancies in the grid especially in the wake region, new grids were made. The grid set up is motivated by the suggestions given by Travin *et al* in [72]. The grid compositions are, 217x189x30 and 217x189x42. In these grids the number of grid points in the circumferential and radial directions are kept constant and only the grid points in the spanwise direction are changed. The radius of the cylinder is 0.5. The positions of the outer boundaries in case of Travin *et al* [72] are at 30R and in case of Kravchenko and Moin [87] are at 60R. Hence, the locations of the outer boundaries are compromised to be placed at 40R.In the spanwise direction, the grid extends from 0.0 to 2.0. The initial grid spacing is $5x10^{-5}$ and the first grid point is typically well inside the sublayer. A snapshot of the grid in the XY plane is presented in Figure 6-1 and also a closer view can be seen in Figure 6-2. The grid is made such that the dimensions of a volume cell are roughly cubed, with the dimensions of ~0.05, in the wake region from x ~ 1.0 to 2.5. The simulations will be run with these improved grids to get better results.

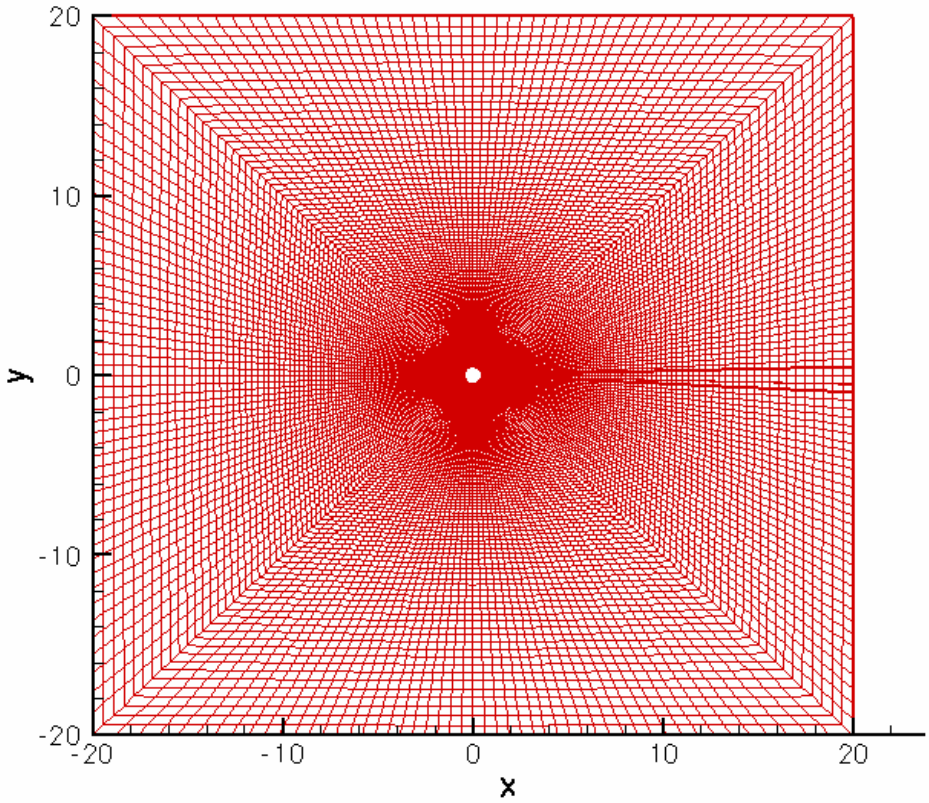

Figure 6-1 Snapshot of the improved grid

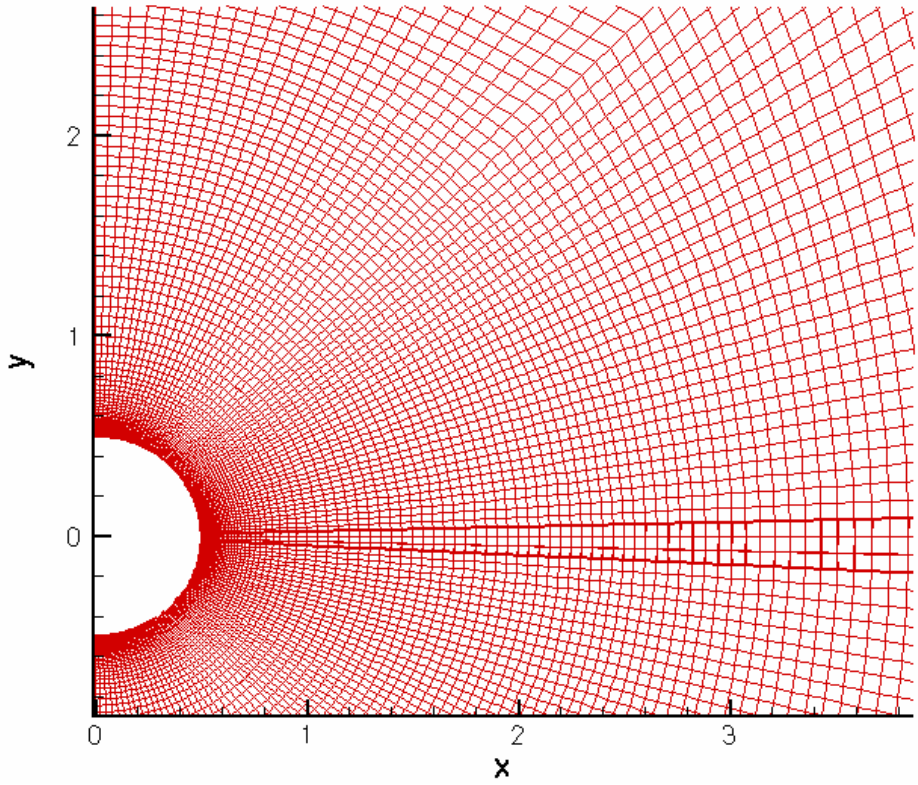

Figure 6-2 Closer view of the improved grid

REFERENCES

1. P. R. Spalart, W. H. Jou, M. Strelets, and S. R. Allmaras. Comments on the feas1ibility of LES for wings, and on a hybrid RANS/LES approach. In: Proceedings of first AFOSR international conference on DNS/LES, Ruston, Louisiana. Greyden Press, 4-8 Aug (1997).

2. P. A. Libby. *Introduction to Turbulence*, Taylor & Francis, Washington, DC, (1996).

3. L. F. Richardson. *Weather Prediction by Numerical Process*, Cambridge University Press (1922).

4. A. Tsinober. *An Informal Introduction to Turbulence*, Kluwer Academic Publishers, Dordrecht (2001).

5. H. Tennekes and J. L. Lumley. *A First Course in Turbulence*, MIT Press (1972).

6. D. C. Wilcox. *Turbulence Modeling for CFD*, DCW Industries, Inc., La Canada, CA (1993).

7. O. Reynolds. An experimental investigation of the circumstances which determine whether the motion of water shall be direct or sinuous, and of the law of resistance in parallel channels. *Phil. Trans. R. Soc. London, Ser.* A, 174, pp. 935-982 (1883).

8. O. Reynolds. On the dynamical theory of incompressible viscous fluid and the determination of the criterion. *Phil. Trans. R. Soc. London, Ser.* A., 186, pp. 123-161 (1895).

9. L. Prandtl. Bericht uber Untersuchungen zur ausgebildeten Turbulenz, ZAMM, 5, 2, pp. 136-139 (1925).

10. T. von Karman. Mechanische Ahnlichkeit und Turbulenz, *Proc. Int. Congr. Appl. Mech.*, 3rd, Stockholm, Part 1, pp. 85-105 (1930).

11. L. Prandtl. Ube rein neues Formelsystem fur die ausgebildete Turbulenz, *Nacr. Akad. Wiss. Gottingen*, Math-Phys. Kl., pp. 6-19 (1945).

12. A. N. Kolmogorov. Equations of Turbulent Motion of an Incompressible Fluid, *Izvestia Academy of Sciences, USSR*; Physics, Vol. 6, Nos. 1 and 2, pp. 56-58 (1942).

13. P. Y. Chou. On the velocity correlations and the solution of the equations of turbulent fluctuation, *Quart. Appl. Math.*, Vol. 3, p. 38 (1945).

14. J. C. Rotta. Statistische Teorie nichthomogener Turbulenz, *Zeitschrift fur Physik*, Vol. 129, pp. 547-572 (1951).

15. E. R. Van Driest. On turbulent flow near a wall, *Journal of the Aeronautical Sciences*, Vol. 23, p. 1007 (1956).

16. T. Cebeci and A. M. O. Smith. Analysis of Turbulent Boundary Layers, *Ser. in Appl. Math. & Mech.*, Vol. XV, Academic Press, Orlando, FL (1974).

17. B. S. Baldwin and H. Lomax. Thin-Layer approximation and algebraic model for separated turbulent flows, *AIAA Paper* 78-257 (1978).

18. P. Bradshaw, D. H. Ferriss, N. P. Atwell. Calculation of boundary layer development using the turbulent energy equation, *Journal of Fluid Mechanics*, Vol. 28, Pt. 3, pp. 593-616 (1967).

19. B. S. Baldwin and T. J. Barth. A One-Equation turbulence transport model for high Reynolds number wall-bounded flows, NASA TM-102847 (1990) [also see *AIAA Paper* 91-0610 (1991)].

20. U. C. Goldberg. Derivation and Testing of a One-Equation model based on two time scales, *AIAA Journal*, Vol. 29, No. 8, pp. 1337-1340 (1991).

21. B. E. Launder and D. B. Spalding. *Mathematical models of turbulence*, Academic Press, London (1972).

22. P. G. Saffman. A model for inhomogeneous turbulent flow, *Proc. R. Soc., Lond.*, Vol. A317, pp. 417-433 (1970).

23. D. C. Wilcox and I. E. Alber. A turbulence model for high speed flows, *Proc. of the 1972 Heat Trans. & Fluid Mech. Inst.*, Stanford Univ. Press, Stanford, CA, pp. 231-252 (1972).

24. P. G. Saffman and D. C. Wilcox. Turbulence-Model predictions for turbulent boundary layers, *AIAA Journal*, Vol. 12, No. 4, pp. 541-546 (1974).

25. D. C. Wilcox and R. M. Traci. A complete model of turbulence, *AIAA Paper* 76-351, San Diego, CA (1976).

26. D. C. Wilcox and M. W. Rubesin. Progress in turbulence modeling for complex flow fields including effects of compressibility, NASA TP-1517 (1980).

27. C. duP. Donaldson. Construction of dynamic model of the production of atmospheric turbulence and the dispersal of atmospheric pollutants, ARAP Report 175, Aeronautical Research Associates of Princeton, Princeton, NJ (1972).

28. B. J. Daly and F. H. Harlow. Transport equations in turbulence, *Physics of Fluids*, Vol. 13, pp. 1634-2649 (1970).
29. B. E. Launder, G. J. Reece and W. Rodi. Progress in the development of a Reynolds-Stress turbulence closure, *Journal of Fluid Mechanics*, Vol. 68, Pt. 3, pp. 537-566 (1975).

30. J. L. Lumley. Computational modeling of turbulent flows, *Adv. Appl. Mech.*, Vol. 18, pp. 123-176 (1978).

31. D. C. Haworth and S. B. Pope. A generalized Langevin model for turbulent flows, *Physics of Fluids*, Vol. 29, pp. 387-405 (1986).

32. J. Boussinesq. Theorie de l' Ecoulement Tourbillant, *Mem. Presentes par Divers Savants Acad. Sci. Inst. Fr.*, Vol. 23, pp. 46-50, Paris, (1877).

33. G. T. Chapman and M. Tobak. Observations, Theoretical Ideas, and Modeling of Turbulent Flows |Past, Present and Future, in *Theoretical Approaches to Turbulence*, Dwoyer et al. (eds), Springer-Verlag, New York, pp. 19-49 (1985).

34. J. O. Hinze. *Turbulence*, McGraw-Hill, New York (1959).

35. D. C. Leslie. *Developments in the Theory of Turbulence*, Oxford University Press, Oxford (1973).

36. R. S. Rogallo and P. Moin. Numerical simulation of turbulent flows, *Annu. Rev. Fluid Mech.* 16, pp. 99-137, (1984).

37. G. Currie. *Fundamental Mechanics of Fluids*, McGraw-Hill, New York (1974).

38. John D. Anderson Jr., *Computational Fluid Dynamics: The Basics with Application*, McGraw-Hill, New York (1995).

39. D. G Fox and D. K. Lilly. Numerical simulation of turbulent flows. *Rev. Geophys. Space. Phys.* 10, pp. 51–72 (1972).

40. A. S. Monin and A. M. Yaglom. *Statistical Fluid Mechanics: Mechanics of Turbulence*, MIT press, Cambridge, Mass. (1971).

41. Lecture notes by Dr J. M. McDonough, Introduction to Turbulence. http://www.engr.uky.edu/~acfd/lctr-notes634.pdf

42. P. Moin and K. Mahesh. Direct Numerical Simulation: A tool in turbulence research. *Annu. Rev. Fluid Mech.*, 30, pp. 539-578 (1998).

43. S. A. Orszag and G. S. Patterson. Numerical simulation of three-dimensional homogeneous isotropic turbulence. *Phys. Rev. Lett.* 8, pp. 76-79 (1972).

44. P. R. Spalart. Direct numerical simulation of a turbulent boundary layer up to Re_θ=1410. *J. Fluid Mech.* 187, pp. 61-98 (1988).

45. Smagorinsky. General circulation experiments with the primitive equations. I: The basic experiment, *Month. Weath. Rev.* 91, pp. 99-165 (1963).

46. Stephen B. Pope. *Turbulent Flows*, Cambridge Univ. Press, 2000.

47. W. Deardorff. A numerical study of three-dimensional turbulent channel flow at large Reynolds numbers, *J. Fluid Mech.* 41, 453 (1970).

48. A. Leonard. Energy cascade in large-eddy simulations of turbulent fluid flows, *Adv. Geophys.*, C18AD, 237 (1974).

49. U. Piomelli, T. A. Zang, C. G. Speziale, and M. Y. Hussaini. On the large eddy simulation of transitional wall-bounded flows, *Phys. Fluids* A 2, 257 (1990).

50. Germano, U. Piomelli, P. Moin and W. H. Cabot. A dynamic subgrid-scale eddy viscosity model, *Phys. Fluids* A 3, pp. 1760-1765 (1991).

51. J. A. Domaradzki and E. M. Saiki. A subgrid-scale model based on the estimation of unresolved scales of turbulence, *Phys. Fluids* 9, pp. 1-17 (1997).

52. D. K. Lilly. On the application of the eddy viscosity concept in the inertial subrange of turbulence, NCAR Manuscript 123, 1966

53. P. Moin and J. Kim. Numerical investigation of turbulent channel flow, *J. Fluid Mech.*, 118, 341 (1982).

54. E.R. van Driest. On the Turbulent Flow near a Wall, *Journal of the Aeronautical Sciences* 23(11), 1007 (1956).

55. U. Piomelli, P. Moin and J. H. Ferziger. Model consistency in large eddy simulation of turbulent channel flow, *Phys*. *Fluids*, 31, pp. 1884-1891 (1988).

56. V. Yakhot and S. A. Orszag. Renormalization group analysis of turbulence, *J. Sci. Comput.*, Vol. 1, p3, (1986).

57. A. Yakhot, S. A. Orszag, V. Yakhot, and M. Israeli. Renormalization group formulation of large-eddy simulations, *J. Sci. Comput.*, 4, 139 (1989).

58. P. R. Spalart. Strategies for turbulence modelling and simulations, *Intl. J. Heat and Fluid Flow*, 21, pp. 252-263 (2000).

59. A. Travin, M. Shur, M. Strelets, P. R. Spalart. Physical and numerical upgrades in the detached-eddy simulation of complex turbulent flows. In: Friedrich, R., Rodi, W. (eds.),

Proceedings of Euromech Coll. 412 "*LES of complex transitional and turbulent flows*," Munich, Germany, 5-6 October 2000. Kluwer, Dordrecht (2002).

60. P. R. Spalart and S. R. Allmaras. A one-equation turbulence model for aerodynamic flows, *La Rech. Aérospatiale* 1, pp. 5-21 (1994)

61. D. C. Wilcox. Reassessment of the Scale Determining Equation for Advanced Turbulence Models, *AIAA Journal,* Vol. 26, No. 11, pp. 1299-1310 (1988a).

62. F. R. Menter. Two-Equation Eddy-Viscosity Turbulence Models for Engineering Applications, *AIAA Journal*, Vol. 32, No. 8, August, pp 1598-1605 (1994).

63. F. R. Menter, M. Kuntz, and R. Bender. A Scale-Adaptive Simulation Model for Turbulent Flow Predictions, *AIAA* 2003-0767 (2003).

64. F. R. Menter. Eddy Viscosity Transport Equations and Their Relation to the k-e Model, *ASME Journal of Fluids Engineering*, Dec. 1997, Vol. 119, pp. 876-884 (1994b).

65. B. S. Baldwin and T. J. Barth. A One-Equation Turbulence Transport Model for High Reynolds Number Wall-Bounded Flows, *AIAA Paper* 91-0610 (1990).

66. P. Spalart, S. Deck, M. Shur, K. Squires, M. K. Strelets and A. Travin. A New Version of Detached-Eddy Simulation, Resistant to Ambiguous Grid Densities, *Theoretical and Computational Fluid Dynamics*, to appear (2006).

67. F. R. Menter, M. Kuntz, and L. Durand. Adaptation of Eddy Viscosity Turbulence Models to Unsteady Separated Flow Behind Vehicles, to be published in *Proc. THE AERODYNAMICS OF HEAVY VEHICLES: TRUCKS, BUSES AND TRAINS*, Monterey, Dec.2-6 (2002).

68. Saurabh Gupta, "Performance evaluation and optimization of the unstructured CFD code UNCLE" Master's Thesis, Dept. of Mechanical Engineering, Univ. of Kentucky, KY, 2006.

69. H. Chen, P.G. Huang and R.P. LeBeau. A cell-centered pressure based method for two/three-dimensional unstructured incompressible Navier-Stokes solver, *Proceedings of the International Conference on Computational Fluid Dynamics* 3, Toronto, Canada (2004).

70. G. Karypis and V. Kumar. A software package for partitioning unstructured graphs, partitioning meshes, and computing fill-reducing orderings of sparse matrices version 4.0," URL: http://www.cs.umn.edu/~karypis, [cited 1998].

71. C. M Rhie and W. L. Chow. Numerical study of the turbulent flow past an airfoil with tailing edge separation, *AIAA J.*, Vol. 21, pp. 1525-1532 (1983).

72. A. Travin, M. Shur, M. Strelets and P. Spalart. Detached-eddy simulations past a circular cylinder, *Flow Turb Comb* **63**, 293 (2000).

73. R. S. Rogallo. Numerical experiments in homogeneous turbulence. *NASA TM-81315* (1981).

74. B. E. Launder and B. I. Sharma. Application of the energy dissipation model of turbulence to the calculation of flow near a spinning disc, Letters in Heat and Mass Transfer, Vol. 1, No. 2, pp. 131-138 (1974).

75. D. K. Lilly. The representation of small-scale turbulence in numerical simulation experiments. In H. H. Goldstine (Ed.), *Proc.* IBM *Scientific Computing Symp. On Environmental Sciences,* pp. 195-210. Yorktown Heights, NY: IBM (1967).

76. J. W. Deardorff. Three-dimensional numerical study of the height and mean structure of a heated planetary boundary layer. *Boundary-Layer Meteorol.* 7, 81-106 (1974).

77. R. H. Kraichnan. Eddy viscosity in two and three dimensions, *J. Atmos. Sci.* 33, pp. 1521-1536 (1976).

78. J. R. Chasnov. Simulation of the Kolmogorov inertial subrange using an improved subgrid model, *Phys. Fluids A* 3, pp. 188-200 (1991).

79. U. Schumann. Subgrid scale model for finite difference simulations of turbulent flows in plane channels and annuli, *J. Comput. Phys.* 18, pp. 376-404 (1975).

80. P. Moin and J. Kim. Numerical investigation of turbulent channel flow, *J. Fluid Mech.* 118, pp. 341-377 (1982).

81. U. Piomelli. High Reynolds number calculations using the dynamic subgrid-scale stress model, *Phys. Fluids A* 5, pp. 1484-1490 (1993).

82. B. Galperin and S. A. Orszag. *Large Eddy Simulation of Complex Engineering and Geophysical Flows,* Cambridge Univ. Press (1993).

83. A. Roshko. Experiments on the flow past a circular cylinder at very high Reynolds number, *J. Fluid Mech.* **10**(3), pp. 345-356 (1961).

84. J. W. G. van Nunen. Pressure and forces on a circular cylinder in a cross flow at high Reynolds numbers, In: Naudascher, E. (ed.), *Flow Induced Structural Vibrations*. Springer-Verlag, Berlin, pp. 748-754 (1974).

85. E. Achenbach. Distribution of local pressure and skin friction around a circular cylinder in cross-flow up to Re = 5 x 10^6, *J.Fluid Mech.* **34**(4), pp. 625-639 (1968).

86. B. Cantwell and D. Coles. An experimental study of entrainment and transport in the turbulent near wake of a circular cylinder, *J. Fluid Mech.* **136**, pp. 321-374 (1983).

87. A. G. Kravchenko and P. Moin. Numerical studies of flow over a circular cylinder at Re_D=3900, *Phys. Fluids,* **12**(2), pp. 403 (2000).

88. Amit Kasliwal, Karman Ghia, and Urmila Ghia. Higher-Order Accurate Solution for Flow Past a Circular Cylinder at Re = 13,400, *AIAA* paper 2005-1123 (2005).

89. C. Norberg. An experimental investigation of the flow around a circular cylinder: Influence of aspect ratio, *Journal of Fluid Mechanics*, 258, pp. 287 (1994).

90. L. M. Lourenco and C. Shih. Characteristics of the plane turbulent near wake of a circular cylinder. A particle image velocimetry study, (private communication).

91. M. Sarioglu, and T. Yavuz. Subcritical Flow Around Bluff Bodies, *AIAA Journal*, Vol. 40, No. 7, July (2002).

VITA

Sri S Panguluri was born in Hyderabad, India on 16th of February 1983. She received her Bachelor of Engineering degree in Mechanical Engineering from MVSR Engineering College affiliated to Osmania University. She entered the University of Kentucky in August 2004 to pursue her Masters degree in Mechanical Engineering. She conducted research on the implementation and validation of the hybrid turbulence models in an unstructured grid code.

Conferences

Sri Swetha Panguluri and Raymond P. LeBeau, Jr. – "Investigation of the Grid spacing calculation effects on the performance of Detached Eddy Simulation**",** 32st AIAA Annual Dayton-Cincinnati Aerospace Science Symposium, Dayton, Ohio, USA.